Shape parameter estimation of a 3D model from multi-view radiographic images

Cédric Fragnaud

université
PARIS-SACLAY

Shape parameter estimation of a 3D model from multi-view radiographic images

Estimation de paramètres de forme d'un modèle 3D à partir d'images radiographiques multi-vues

Thèse de doctorat de l'université Paris-Saclay

École doctorale n°579, Sciences mécaniques et énergétiques, matériaux et géosciences (SMEMaG)
Spécialité de doctorat: Mécanique des matériaux
Graduate School : Sciences de l'ingénierie et des systèmes, Référent : ENS Paris-Saclay

Thèse préparée dans l'unité de recherche **LMPS** (Université Paris-Saclay, CentraleSupélec, ENS Paris-Saclay, CNRS), sous la direction de **Stéphane ROUX**, Directeur de Recherche CNRS, et le co-encadrement de **Julián BETANCUR**, Ingénieur de Recherche

Thèse soutenue à Paris-Saclay, le 4 janvier 2023, par

Cédric FRAGNAUD

Composition du jury

Membres du jury avec voix délibérative

Rachid DERICHE Directeur de Recherche INRIA, Sophia-Antipolis	Président
Jean-Yves BUFFIÈRE Professeur, MATEIS, INSA Lyon	Rapporteur & Examinateur
Marc FRANÇOIS Professeur, GeM, Université de Nantes	Rapporteur & Examinateur
Jan SIJBERS Professeur, Vision Lab, University of Antwerp	Examinateur
Caroline VIENNE Ingénieure de Recherche, CEA List, Université Paris-Saclay	Examinatrice

THESE DE DOCTORAT
NNT : 2023UPAST003

Contents

Remerciements

Ces trois années de thèse ont été le terrain de rencontres diverses et variées, toutes extrêmement enrichissantes, qu'il convient de mentionner avant de présenter mes travaux.

Dans un premier temps, je tiens à remercier les membres du jury qui m'ont fait l'honneur d'évaluer le projet de recherche que j'expose ici, et d'avoir alimenté les réflexions au cours de la soutenance. En particulier, merci à Rachid Deriche d'avoir présidé le jury, et à Jean-Yves Buffière et Marc François, rapporteurs, pour les échanges et pistes d'amélioration proposés et discutés.

Ce travail n'aurait pu être mené sans la précieuse aide de Stéphane Roux, qui a assumé la responsabilité de directeur de thèse. Sa rigueur, sa disponibilité et son expertise scientifique ont été d'une aide inestimable tout au long de ces années. Ses précieux conseils et sa passion pour la recherche m'ont permis de progresser dans ma compréhension des concepts fondamentaux et de développer mon esprit critique. Je suis particulièrement reconnaissant pour les précieux enseignements qu'il a su me transmettre. Je tiens également à remercier Julian Betancur, encadrant industriel de ces travaux, pour son soutien, ses conseils éclairés et sa volonté à m'encourager à valoriser mes travaux. Sa connaissance approfondie de l'industrie m'a permis de comprendre les enjeux pratiques de ces travaux et de développer une vision plus globale de mon travail. Également, la réussite des essais doit évidemment énormément à Clément Remacha qui, bien qu'il ne fasse pas partie de l'équipe d'encadrement, a su m'apporter son expertise essentielle. Son professionnalisme et son implication ont grandement contribué à la qualité des résultats obtenus.

Je tiens aussi à adresser mes remerciements aux collègues de Safran pour leur accueil chaleureux au sein du groupe et pour les échanges, scientifiques ou non, que nous avons eus. Cela inclut bien évidemment les membres de l'équipe A2MC, pour qui j'ai une estime et un respect particulier pour les précieux conseils qu'ils m'ont promulgués et leur ouverture d'esprit, mais aussi plus généralement ceux du service NDIS.

Les collègues du LMPS méritent également mes remerciements. Qu'il s'agisse des doctorants, post-doctorants, permanents, techniciens, personnels administratifs, ou stagiaires, j'ai apprécié leur sympathie, leur professionalisme et leur capacité d'écoute et de transmission. Je retiendrais les discussions impromptues dans les bureaux, les pauses-café qui n'en finissent plus ou encore les moments de travail intensif et de détente et de collation bien mérités dans la salle des doctorants. Ils ont su me faire découvrir le monde passionnant de la mécanique et de la recherche tout en entretenant une bonne ambiance.

Je voudrais également exprimer ma gratitude envers mes amis d'écoles, en particulier le groupe I et le groupe GM. Leurs encouragements, leur présence dans les moments difficiles et leur soutien indéfectible ont été une véritable bouffée d'air frais et une aide inestimable. Certains d'entre eux étaient présents lors de ma soutenance, et je suis heureux d'avoir pu partager ce moment particulier avec eux.

Enfin, je tiens à remercier ma famille pour leur soutien continu tout au long de ces trois années, et plus encore. De par leur présence, leur soutien et leur confiance en moi, ils m'ont aidé à surmonter les défis rencontrés et m'ont permis de continuer à avancer dans ma thèse.

Chapter 1

Introduction

Contents

1.1 Context

Aeronautics is a jewel of French industry, regularly put in the spotlight during the aerial display held for the French National Day. On a daily basis, tens of thousands of flights performed globally by the airline industry carry millions of passengers worldwide. For the safety of the pilot, crew, passengers, and people on the ground, it is vital that aircraft and their components meet rigorous safety requirements guaranteed by the manufacturers.

Aircraft are complex systems whose components, in particular the engine, handle severe operating conditions. The majority of recent aircraft engines are two-spool jet engines in which the compressor and turbine are each divided into two sections: the low pressure (LP) and high pressure (HP) sections. After the ignition of the air-kerosene mixture in the combustion chamber, hot exhaust gas flows through the HP turbine. The latter consists of multiple stages, each being composed of a stator and a rotor. The rotor corresponds to a metallic disk in which blades are fixed.

These blades, called HP turbine blades, are exposed to the extreme temperature of exhaust gas, known as the HP turbine inlet temperature. In an effort to improve engines efficiency, these temperatures have continuously increased since the 20$^{\text{th}}$ century, reaching now up to 1580°C, higher than the blades melting point. In addition, they endure severe mechanical constraints, *inter alia* due to the centrifugal force caused by their rotation around the HP shaft. The blades withstand these intense thermal and mechanical conditions through multiple solutions that include cooling systems, thermal barriers consisting of ceramic coating, and the recourse to materials known for their mechanical properties such as nickel-based alloys with a single-crystal microstructure. For these features to be efficient, it is essential that HP turbine blades comply with stringent controls. These controls are performed during periodic maintenance operations, but also directly when the part is manufactured, through Non Destructive Evaluation (NDE).

The French Confederation for Non Destructive Testing (COFREND) defines Non Destructive Evaluation as "a set of methods for characterizing the state of integrity of structures or materials, without deteriorating them, and at different stages in their life cycle". They ensure the conformity of the produced parts and, for critical aeronautic parts, are an essential step towards safety. NDE is widely used in industry to inspect the compliance of manufactured parts with respect to their design and quality specifications. Notably, the study of their shape is of great importance during control.

In the following section, we will present the most commonly used NDE techniques applied to aeronautical parts, in particular to the HP turbine blades. This thesis work will focus on the control of the shape of an HP turbine blade during its production phase. Consequently, the attention will be centered on dimensional controls for which the aim is to detect geometrical indications (dimensional irregularities that may result in a non-optimal system) in the inspected part.

1.2 NDE methods

Several Non Destructive Evaluation methods are used to control turbine blades during manufacturing or maintenance operations. The objective is to detect and avoid any flaw that could propagate and cause a failure. They are divided into (i) material health inspection methods and (ii) dimensional control methods.

Material health inspections aim to detect and characterize structural defects such as porosities, cracks, inclusions, or welding defects. They include the thermography imaging approaches [1, 2], based on the detection of the thermal radiation of the material using an infrared camera. Magnetic particle inspection [3] relies on detecting the disturbance in the magnetic flux caused by a defect, *e.g.* a crack, when a specimen made of a ferromagnetic material is exposed to a magnetic field. This detection is made possible by applying ferromagnetic particles, containing colored or fluorescent pigments, onto the surface of the part. Eddy current testing [4, 5, 6, 7] is based on the analysis of the local changes in the electromagnetic properties of the material due to a structural flaw.

Dimensional controls refer to inspections applied on the part to verify the dimensions defining its geometry and quantifying their deviations. Aeronautical parts such as HP turbine blades operate at very high temperatures, above the material melting

point. In order to ensure the integrity of the engine, cooling technologies have been developed [8, 9, 10, 11, 12]. Among them, the internal cooling systems use convective heat transfer in internal channels to withdraw heat from the blade. The cooling circuit, in which a flow of cooled air extracted from the LP compressor circulates from the hub towards the blade tip, needs to be highly efficient. A large internal surface area is desirable for this technology, so the cooling circuits tend to be serpentine and full of small structures (fins, ribs). As a result, HP turbine blades have complex geometries, resulting from a long joint work carried out by researchers and the design office. Therefore during manufacturing, both external and internal geometries of the blade must be very carefully controlled.

In the following, the most common dimensional control methods are introduced. Since the internal structure inspection is of particular interest, only modalities allowing measurements of internal elements are presented.

1.2.1 Ultrasound control

Ultrasonic control [1] consists of scanning the part to be inspected with elastic waves to measure material thicknesses. The measuring device, that corresponds to a transmitter and receiver of ultrasonic waves, is placed onto the surface of the sample perpendicular to it [13]. The interpretation of the time-of-flight (time difference between the emission and reception of the ultrasonic wave) allows the measurement of thickness at the sampling point.

This technique has been thoroughly developed [14, 15, 16, 17, 18], and thus provides accurate measurements. However, they are performed on a limited number of sampling points on the external surface: no global information on the geometry is obtained. In some cases, the device is difficult to position, *e.g.* for sampling points close to curved areas, which makes the control difficult. In addition, some measurements are impossible to assess, such as high thickness measurements or inter-cavity distances. The difficulty may also arise from weak or distorted "echoes" from the internal surface (*e.g.* oblique orientation, curved surface, proximity of a hole).

1.2.2 Radiographic imaging

Radiographic imaging methods used for NDE include X-ray [19, 20, 21], gamma-ray [22, 23], and neutron radiography/tomography [24, 25]. These technologies allow the internal structure of the part to be imaged by transmission and operate similarly. A radiograph is the transmission image of the part by radiation (X-ray, gamma, or neutron). Because of the interaction between the light beam and the material, these images allow the detection of dimensional flaws in the part: over-/under-thickness of the material, mispositioning of an element such as cooling holes, *etc.*.

X-rays and gamma-rays highly interact with dense materials and little with lighter ones, whereas neutron radiations reveal a different contrast. However, neutron sources are only available on large instruments — *e.g.* in France, the *Institut Laue–Langevin* in Grenoble — which limits their use. In the industry, and in particular in the aeronautical sector, X-ray imaging is the most widely used radiographic imaging technique.

1.2.2.1 X-ray radiography

An X-ray source irradiates the part under inspection [26]. Beams are attenuated at varying levels depending on the straight path they follow as they pass through the object. The ray intensities are measured by a detector array to obtain a 2D image of the specimen displaying the spatial distribution of its structure.

The control is then performed based on a restricted set of images, usually about ten, constituting a limited amount of information about a complex-shaped object. Trained operators examine the images seeking unusual gray levels, indicating the presence of a dimensional imperfection. Considering the difficulty of the task, an inter-operator bias may exist (*e.g.* due to difference in training or experience) as well as an intra-operator bias (*e.g.* due to fatigue, or psychological condition). In addition, the images result from complex interactions between the object and the X-ray photons, which must be understood and quantified to properly interpret gray levels. Thus, the characterization of 3D dimensional imperfections from 2D images is challenging.

1.2.2.2 X-ray tomography

X-ray tomography relies on the same technology and physical phenomena as X-ray radiography. The difference lies in the number of acquired images, typically a few thousand. This gain in the amount of information allows the 3D volume of the part, known as *tomogram*, to be computed using reconstruction methods [27, 28]. The tomogram is used to observe the (complex) internal structure of the part in a very detailed way and to perform measurements of *e.g.* angles, distances, and volumes. Furthermore, the alignment of the tomogram with the Computer-Aided Design (CAD) model of the part describing its nominal geometry allows observation and measurement of shape deviations.

This method is ill-adapted for production needs as the acquisition of thousands of images is time-consuming (around one hour per blade). In addition, the complex interactions underlying the formation of the images generate image artifacts in the tomogram if they are not properly estimated and corrected, which impedes precise control.

In light of the above, X-ray radiography appears to be a suitable compromise for dimensional control of complex-shaped parts. It provides global information about their geometry (both external and internal surfaces) while allowing a short inspection time, making it suited to production needs. In the following, a detailed description on the principle of X-ray radiography is proposed, which will highlight the main difficulties associated to the NDE of objects *via* X-ray radiography.

1.3 Principle of X-ray imaging

X-rays are a high-energy electromagnetic radiation. Due to their high capability of matter penetration, they are widely used to image the inside of objects.

1.3.1 X-ray generation

In electron-impact X-ray sources, the radiation is produced by the deceleration of fast-moving electrons hitting a solid metal anode [26]. Figure 1.1 represents an X-ray

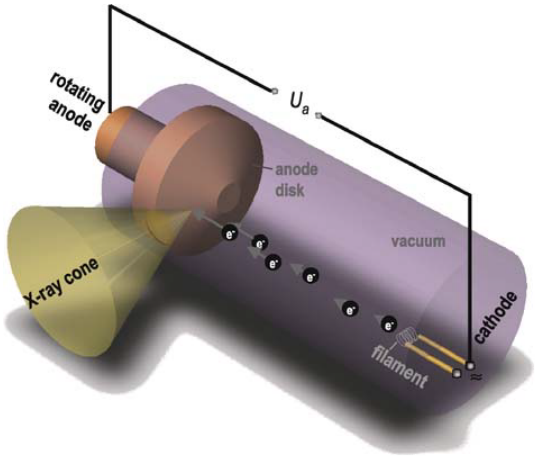

Figure 1.1: X-ray tube generator [26].

tube generator using this principle. A filament usually made of thoriated tungsten is heated, producing electrons through a phenomenon called thermionic emission. They are accelerated by the electric field between the cathode and the anode. Close to the anode surface, they undergo several processes, the main one being their deceleration by the Coulomb fields of the atoms in the metallic anode [29]. The slowdown of electrically charged particles leads to the emission of electromagnetic waves in the X-ray spectrum (wavelength from about 10^{-8} to 10^{-12} m). A continuous distribution of energies is thus obtained by the *bremsstrahlung*. In addition, fast electrons may directly interact with the inner shell electrons of the anode material. A fast electron may collide and kick out an electron on a K-shell or L-shell of the atom. An electron of one of the higher shells fills the vacant position on the K-shell or L-shell, which causes the emission of a photon. This de-ionization phenomenon creates a large number of X-ray radiations at discrete energies, known as the characteristic K-line or L-line.

The radiation energy of the emitted X-ray depends on the energy of the accelerated electron, which in turn depends on the anode-to-cathode voltage, also called the acceleration voltage. For material testing, acceleration voltages are usually chosen between 200 kV and 400 kV and can reach up to 500 kV.

Figure 1.2 displays the X-ray spectrum of a tungsten anode, depicting the number of emitted photons (in arbitrary units) as a function of energy. The spectrum was calculated using xpecgen [30, 31] without filtering the source and with two types of filters, copper and aluminum. The characteristic lines are visible at approximately 58 keV and 67 keV. The filters reduce the number of X-ray photons emitted from the source by absorbing photons at all energies, with lower-energy photons being more strongly attenuated.

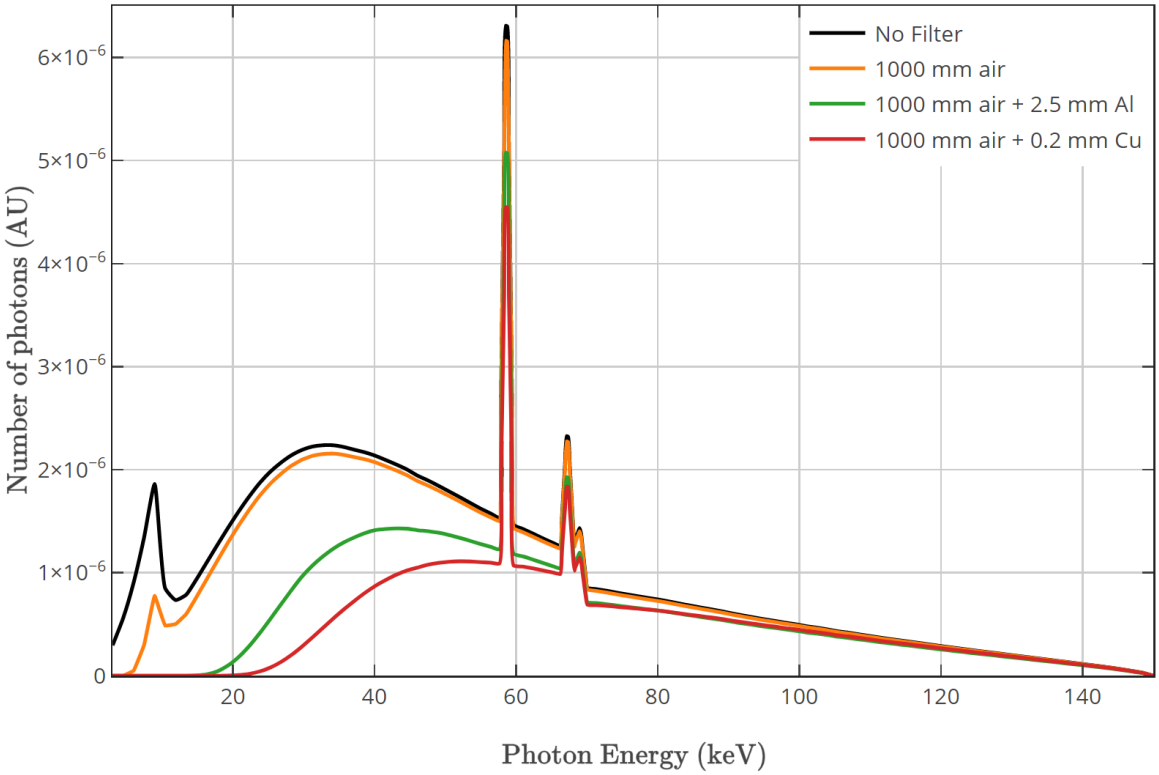

Figure 1.2: X-ray spectrum produced by a tungsten anode (anode angle of 10°, electron kinetic energy of 150 keV) simulated using xpecgen [30, 31] without and with filtering. The amount of intensity reduction due to the filtering depends on the energy. The characteristic lines are clearly visible.

1.3.2 Photon–matter interactions

Radiations emerging from the X-ray tube are directed in a conical shape toward the analyzed part placed in front of a detector panel, a photosensitive device used to convert X-ray quanta into images. Projection data (*i.e.* the radiographic images) are the result of the interaction between those radiations and the material of which the object is composed. In X-ray imaging, the attenuation a beam of X-ray has undergone after passing through the object is measured.

This section describes the attenuation law and the two main physical mechanisms of photon–matter interaction occurring for the targeted acceleration voltage: the photoelectric and the Compton scattering effects.

1.3.2.1 Attenuation of beam intensity: Beer-Lambert's law

Consider a polyenergetic X-ray traveling along the path $\mathcal{L}_{\boldsymbol{x}}$ joining the source to a detector position $\boldsymbol{x} \in \boldsymbol{\Omega}$, with $\boldsymbol{\Omega}$ the domain of all detector positions. The intensity $I(\boldsymbol{x})$ recorded at this position is related to the line integral of the material absorption along $\mathcal{L}_{\boldsymbol{x}}$ according to the polyenergetic Beer-Lambert's law

$$I(\boldsymbol{x}) = \int_{\mathcal{E}} I_0(\boldsymbol{x}, E) \ \exp\left(- \int_{\boldsymbol{y} \in \mathcal{L}_{\boldsymbol{x}}} \mu(\boldsymbol{y}, E) \, \mathrm{d}\boldsymbol{y} \right) \, \mathrm{d}E \tag{1.1}$$

where $\mathcal{E}$ denotes the energy spectrum, μ is the spatially and energy-dependent attenuation coefficient, and $I_0(\boldsymbol{x}, E)$ the intensity measured when no sample is found along the X-ray path $\mathcal{L}_{\boldsymbol{x}}$ and whose image as captured by the detector is called flat-field. For many materials, the linear coefficient $\mu(\boldsymbol{y}, E)$ decreases with increasing photon energy. When passing through an object, low-energy (soft) photons are absorbed preferentially, so that the remaining beam becomes proportionally richer in high-energy (hard) photons than the original beam. This phenomenon is known as *beam hardening*. The measured intensity $I(\boldsymbol{x})$ is proportional to the number of photons of a given energy impinging on the detector position $\boldsymbol{x}$ weighted by a response efficiency that depends on the energy.

If the object Ω_0 is made of a monomaterial component, the spatial dependence of the attenuation is removed for the entire path of penetration, *i.e.* $\mu(\boldsymbol{y}, E) \equiv \mu(E)\, \mathbb{1}_{\{\boldsymbol{y} \in \mathcal{L}_{\boldsymbol{x}} \cap \Omega_0\}}$, so that eq. (1.1) can be rewritten as

$$I(\boldsymbol{x}) = \int_{\mathcal{E}} I_0(\boldsymbol{x}, E) \exp\left(-\mu(E)\; T(\boldsymbol{x})\right)\; \mathrm{d}E \tag{1.2}$$

where $T(\boldsymbol{x})$ denotes the distance traveled by the ray inside the object.

The attenuation image P is derived from the measured intensity image I by setting

$$P(\boldsymbol{x}) = -\ln\left(\frac{I(\boldsymbol{x})}{I_0(\boldsymbol{x})}\right) \tag{1.3}$$

where $I_0(\boldsymbol{x})$ is obtained by integrating $I_0(\boldsymbol{x}, E)$ over all energies (in practice, the integration is weighted by the detector response depending on the energy). The nonlinearity between the attenuation value $P(\boldsymbol{x})$ and the thickness of material $T(\boldsymbol{x})$ calls for a careful interpretation of the gray levels of the measured images.

A common approach is to model the beam as being monoenergetic. The associated attenuation law is known as the (monoenergetic) Beer-Lambert's law, and the attenuation image is interpreted as

$$P(\boldsymbol{x}) = \mu\; T(\boldsymbol{x}) \tag{1.4}$$

This simplified formulation leads to a misinterpretation of the grayscale values. Thicknesses are underestimated (see Figure 1.3), or overestimated depending on the calibration between P and T (such a calibration being required for any practical application of radiography). Various schemes have been proposed to correct for these deviations. They can be divided into two main categories: pre-processing of projection data [32, 33] and dual energy imaging [34, 35].

The attenuation coefficient $\mu(E)$ is the sum of several components, each representing the contribution of a physical phenomenon to the intensity attenuation [36]. In industrial CT, photon energy ranges from around 100 to 400 keV. It is observed from Figure 1.4 that, within this energy range (cyan area), the predominant processes responsible for the attenuation of the X-ray beam intensity are the photoelectric absorption (orange curve) and the Compton scattering (green curve). In this sense, $\mu(E)$ may be written as a combination of a Compton scatter coefficient $\mu_s(E)$, and a photoelectric absorption coefficient $\mu_a(E)$.

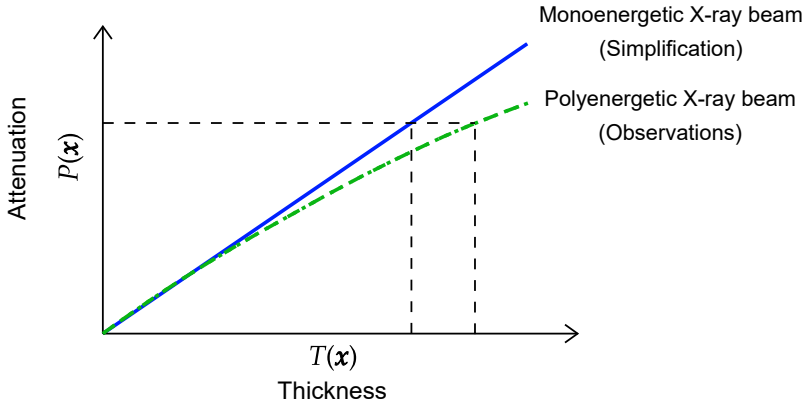

Figure 1.3: Differences between polyenergetic observations (green dashed line) and monoenergetic simplification (blue line). When considering monoenergetic Beer-Lambert's law, the analysis of grayscale values leads to an underestimation of the thickness the beam had gone through.

1.3.2.2 Photoelectric absorption

The photoelectric absorption effect is a pure photon absorption process that results in total absorption of the X-ray photon [29, 38]. This phenomenon is caused by the collision between a photon, with energy E_e, and an innermost shell (K-shell) electron bound in an atom of the material with a binding energy $E_b < E_e$ (Figure 1.5, top left). The photon is entirely absorbed by the atom, and the electron, called *photoelectron*, is ejected with kinetic energy equal to the difference $E_e - E_b$. This energy difference is thus removed from the incoming X-ray beam. Photoelectric absorption depends strongly on the unique binding energy of any K-shell electron for a particular material.

The vacancy left by the photoelectron is filled by electrons from outer shells. This recombination leads to the emission from the atom of characteristic radiations so that X-ray fluorescence lines can be measured (Figure 1.5, top right). Provided that the radiation energy resulting from the recombination process is high enough, it may instead eject another electron from the outer shell of the atom, resulting in the creation of a so-called *Auger electron* (Figure 1.5, bottom right). It should be noted that the emission of characteristic radiations and the creation of an Auger electron are mutually exclusive outcomes of the vacancy left by the photoelectron.

1.3.2.3 X-ray scattering: Compton effect

Scattering is a phenomenon that causes a reduction of contrast in the acquired images. Some photons emitted toward the object will deviate from their initial trajectories (straight path) due to their interaction with the material. They will thus hit the detector at a different position from where they should have been initially detected. When hitting the detector, a scattered photon will lead to an increase of the measured intensity away from its initial trajectory, and a decrease at this specific position, producing a blur in the images. Usually, image analysis for quantitative imaging only considers the absorption of the beam and does not account for scattering. This leads to a deviation of dimensional measurements from their actual values.

X-ray scattering is due to two physical phenomena: the Compton effect and the Rayleigh effect. The type of scatter that prevails (Compton or Rayleigh) depends

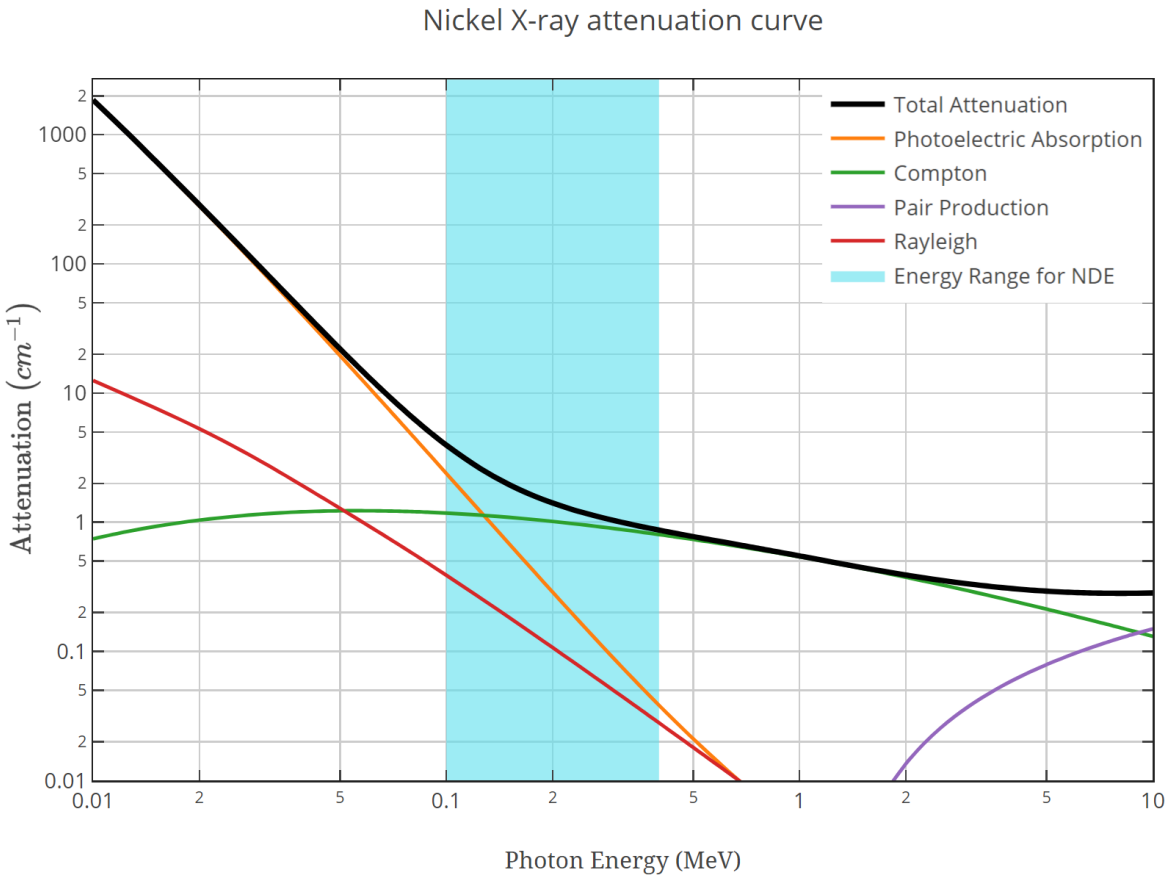

Figure 1.4: X-ray attenuation curve for Nickel describing the main interactions of X-ray photons with matter. Compiled with data from the online database XCOM [37]

on the beam's energy. Figure 1.4 indicates that, in the target industrial application, Compton scattering dominates over Rayleigh scattering.

The Compton effect refers to the interaction between a photon from the X-ray beam with a free electron of the inspected part or an electron weakly bounded to its atom [26]. As a result, the incident photon loses part of its energy which is transferred to the electron, and is deflected (scattered away) at a *scattering angle* φ from its original path (Figure 1.6) [29, 39]. Because of this energy loss, the wavelength of the scattered photon is larger (meaning less energetic photons) than that of the incident radiation: scatter distribution thus has dominant low-frequency components.

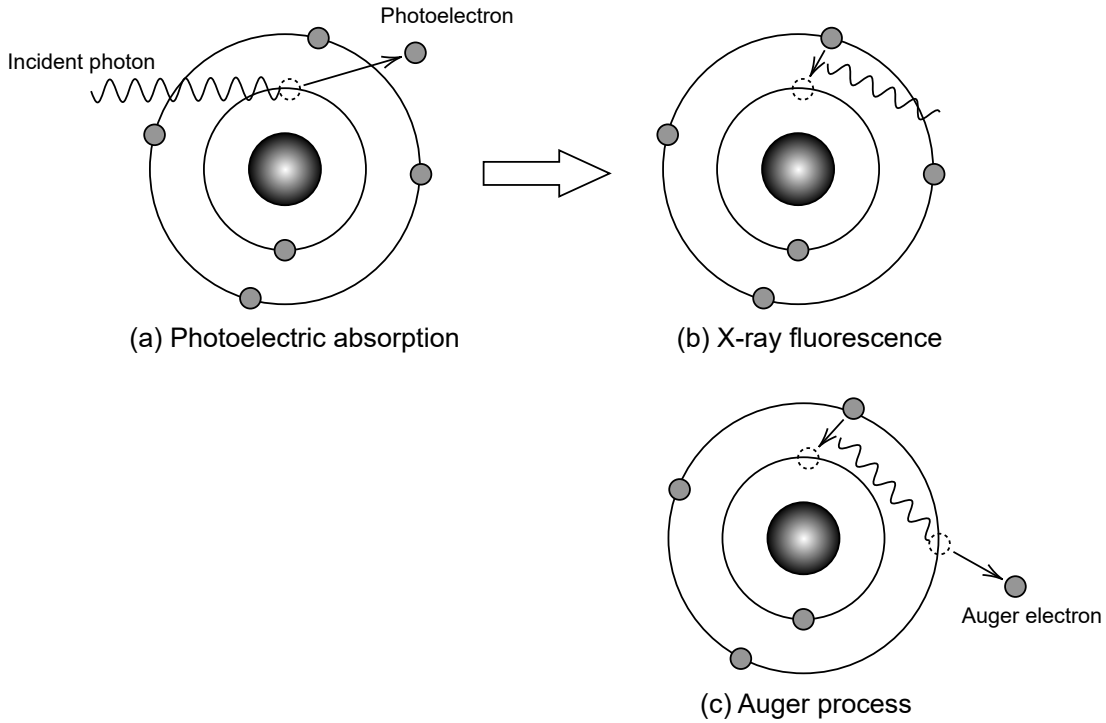

Figure 1.5: Principle of photoelectric effect. (Top left) Absorption of the X-ray photon and ejection of the electron. (Top right) The vacancy left by the ejected electron is filled, resulting in the emission of characteristic radiations. (Bottom right) The vacancy left by the ejected electron is filled, and an Auger electron is generated.

The probability of photon scattering by a free electron as a function of φ is given by the differential Klein-Nishina cross-section formula [29, 40]

$$\frac{\mathrm{d}\sigma_{KN}}{\mathrm{d}\Omega} = \frac{r_e^2}{2}\,\varepsilon^2\left(\varepsilon + \frac{1}{\varepsilon} - \sin^2(\varphi)\right) \tag{1.5}$$

where $\mathrm{d}\Omega = \sin(\varphi)\,\mathrm{d}\varphi\,\mathrm{d}\alpha$ denotes the differential solid angle (α being the azimutal angle), r_e is the classical electron radius, and ε is the ratio between the scattered photon energy $E'(\varphi)$ and the incident photon energy E, *i.e.* $\varepsilon = \varepsilon(E, \varphi)$. Due to the rotational symmetry of diffusion around the beam, the scattered intensity only depends on φ, and hence one may integrate this scattered flux over α so that only the solid angle $\mathrm{d}\Omega = 2\pi\sin(\varphi)\,\mathrm{d}\varphi$ matters.

When the photon is scattered by a bound electron, the electronic binding effects must be taken into account. This contribution of surrounding electrons is modeled by multiplying eq. (1.5) with the incoherent scattering function $S(q(\varphi), Z)$, where $q(\varphi)$ is the momentum transfer variable[1] and Z is the atomic number of the absorber material, yielding the differential Compton cross-section $\frac{\mathrm{d}\sigma_c}{\mathrm{d}\Omega}$. Integrating this expression over the entire solid angle Ω gives the Compton scattering cross section

$$\sigma_c = \pi r_e^2 \int_0^\pi \varepsilon^2\left(\varepsilon + \frac{1}{\varepsilon} - \sin^2(\varphi)\right)\sin(\varphi)\;S(q(\varphi), Z)\,\mathrm{d}\varphi \tag{1.6}$$

[1] $q(\varphi) = 4\pi\sin\left(\frac{\varphi}{2}\right)\frac{E'(\varphi)}{hc}$ where h is Planck's constant and c is the speed of light.

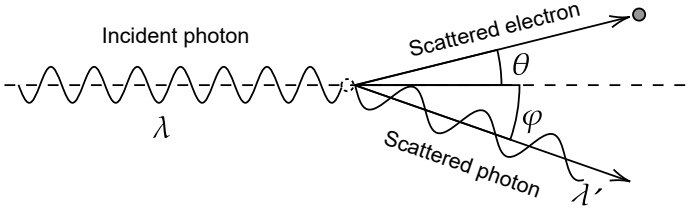

Figure 1.6: The Compton effect. Collision between a photon and a free electron. The scattered photon has a longer wavelength than that of the incident one.

The scattering angle thus depends on the energy of the X-ray beam. An example of angular Compton scattering probability by a single free electron at different energies is illustrated in Figure 1.7. This figure indicates that the scattering probability decreases as the energy increases: it is half as small at 350 keV as it is at very low energy. In addition, at lower energy, scattering occurs more likely in the backward direction.

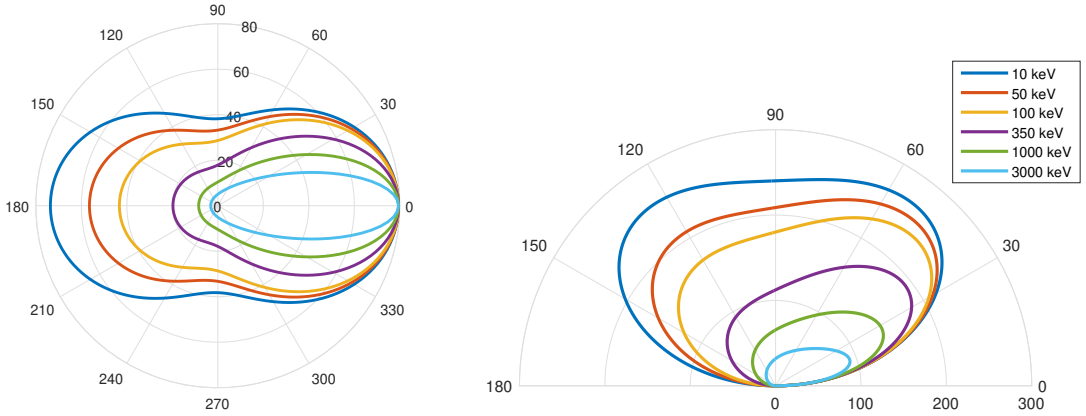

Figure 1.7: Angular Compton scattering probabilities for a free electron as a function of φ for different energies (a) Expressed in millibarn per steradian from the definition of $\frac{\mathrm{d}\sigma_{KN}}{\mathrm{d}\Omega}$. (b) Expressed in millibarn per degree from the definition of $\frac{\mathrm{d}\sigma_{KN}}{\mathrm{d}\varphi}$.

A scattered photon can still interact with another electron to give rise to a second scattered photon, and so on: this is known as *multiple scattering*. However, the more a photon undergoes the Compton effect, the more energy it loses, increasing the absorption probability. The scattering probability being small, only *single scattering* may be considered, with a good approximation.

It is essential to note that scattering can be assimilated to absorption for scattering in a highly different direction. Scattered photons are eliminated from the incident beam through their interactions with atoms (or, more precisely, electrons) in the same way as absorption *via* the photoelectric effect. Given this, the study will be limited to small angle scattering, in addition to the single scattering approximation.

1.4 Objectives and approach

This thesis work focuses on the analysis of the shape of an HP turbine blade during its manufacturing. As discussed in Section 1.2, a multitude of NDE methods are used to inspect the geometry of such parts during their production. Among them, X-ray radiography allows the visualization of the whole internal, potentially complex, and external structures of the part. Additionally, the short acquisition time of X-ray images makes the NDE from a dozen images adapted to the production needs (*i.e.* brief enough not to impact the production rate while ensuring high quality products).

The problem tackled in this work consists in the development of an NDE process for the identification and characterization of geometrical indications of an HP turbine blade from a reduced number of X-ray images. Given that numerous controls are carried out on turbine blades, we restricted ourselves, for practical reasons, to wall thickness inspections. This control is critical as wall thickness imperfections can impair the blades integrity when operating at high temperatures. The process is intended to address the difficulties pointed out in subsection 1.2.2.1, namely:

- *the limited number of views*: this point is synonymous with using a reduced amount of information about the inspected part. To circumvent this difficulty, one may consider exploiting complementary information about the part, such as its CAD model or its manufacturing process.

- *the phenomena involved in the formation of X-ray images*: the formation of X-ray images described in the previous section indicates that a specific attention must be paid regarding the interpretation of the observed gray levels. The gray levels of a projection are related to the thickness of material the beam has gone through, but in a non-linear way due to the beam hardening phenomenon. In addition, phenomena other than pure absorption, such as Compton scattering, lead to the observation of a spurious signal. These two aspects are all the more impacting as the control is performed from a reduced number of images, namely a dozen. Hence, these phenomena should be correctly modeled and estimated to properly interpret the observed gray levels.

- *the operator dependency*: this calls for an automated process, in which the input corresponds to the observed X-ray images (plus additional information, as mentioned above), and the outputs are markers highlighting the geometrical indications on the part (identification), and accurate dimensional measurements (characterization). It should be noted that the procedure is not intended to be a substitute for the operators, but rather to serve as a tool to assist them in the inspection process. The final decision regarding the part (valid, rejected, remanufacture) is left in the hands of the human expert.

- *the bias of assessing 3D dimensional measurements from 2D images*: this issue suggests that measurements should not be computed directly from the images, but rather from a 3D model of the inspected part.

1.4.1 Developed approach

Following these desired features, we developed an NDE process whose pipeline is displayed in Figure 1.8. It relies on Projection-based Digital Volume Correlation (P-

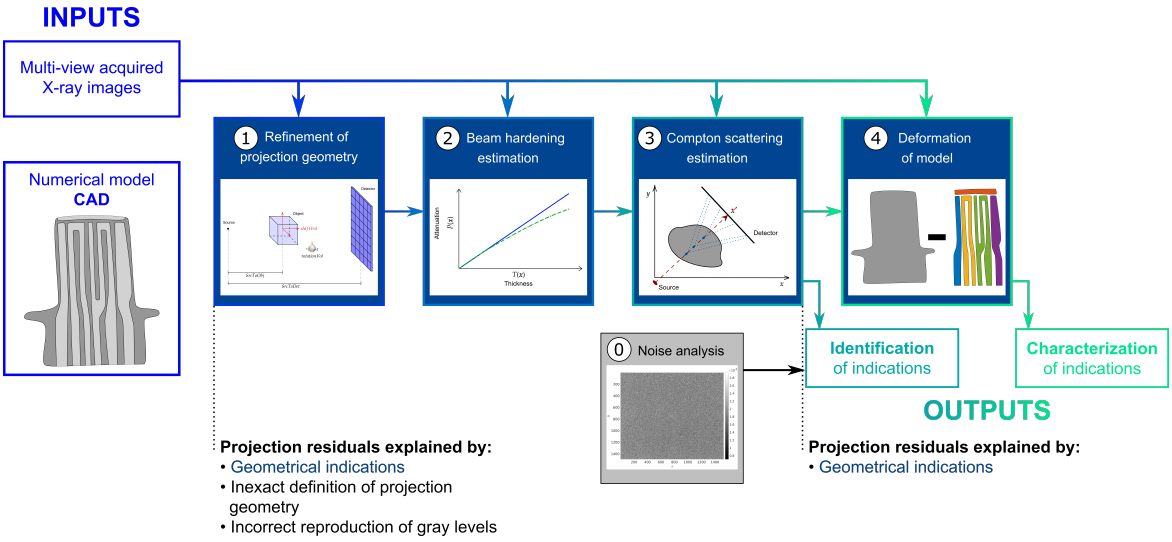

Figure 1.8: Schematic representation of the NDE process for geometrical indications from few radiographic views.

DVC) approach, introduced in [41] and further extended to the study of a fatigue crack in a cast iron sample [42] or to *in-situ* mechanical tests [43]. It aims at reducing the differences, known as *projection residuals* or *residuals*, between acquired X-ray images and numerically computed ones. In this work, the simulated projections have been computed using the ASTRA Toolbox [44]. From the acquired X-ray images representing the inspected part and its CAD model, the process is described by five main steps:

0. **Noise analysis**: A preliminary step in the procedure consists in evaluating the noise affecting a radiographic image. It allows the cost function in the P-DVC to be properly defined, and provides a baseline value (standard deviation of the noise) to interpret the projection residuals. This noise analysis is independent of the X-ray images of the part, as opposed to the following steps that rely on these images, hence the distinct color used in Figure 1.8 and the step number.

1. **Projection geometry refinement**: The simulation of X-ray images requires the definition of the projection geometry which encompasses the geometry of the acquisition system (relative position of the source and detector, orientation of the detector, *etc.*), along with the position and orientation of the part in it. The problem of determining the projection geometry from X-ray images is a subject of interest [45, 46]. It usually requires a phantom whose geometry is perfectly known [47, 48, 49]. Other approaches include the use of features in images simulated from a CAD model [50], or AI-based approaches [51]. In this work, we propose to refine the projection geometry based on a P-DVC method which exploits the entire image, or Regions Of Interest (ROIs) in it.

2. **Beam hardening estimation**: This phenomenon arises from the polyenergetic nature of the X-ray source, resulting in a non-linear relationship between the attenuation and the thickness of material the beam has gone through. Estimating the actual relationship allows the correction of BH, which reduces to a non-linear gray level re-encoding using a (parametric) correction function. Strategies for such an estimation include acquiring projections of a known object and fitting the correction function to the point cloud — pixelwise detector attenuation versus thickness — by the least-squares method [52], but it does not exploit the spatial dependency of gray levels. The correction function is usually modeled as an odd-order polynomial. Another approach consists in performing Monte-Carlo simulations [53], but their applicability in practice is jeopardized by their time-consuming nature. In this work, we propose to identify the correction function, modeled as a piecewise linear function, using P-DVC.

3. **Compton scattering estimation**: Scattering phenomenon leads to the measurement of a spurious signal. Suggestions to estimate and correct for it include Monte-Carlo simulations [54, 55], or model the scatter signal as the convolution between the primary signal and a kernel to be estimated [56] prior to applying a deconvolution algorithm to obtain scatter-free radiographs. In this work, the latter model is used. The associated parameters are identified using P-DVC, and the estimated signal is reproduced on simulated images to avoid numerical instabilities encountered in deconvolution algorithm.

4. **Deformation of model**: To obtain deviation measurements, the actual geometry of the imaged part is to be inferred from the X-ray images. This shape inference relies on deformation models that can be statistical models of global deformations such as "point distribution models" [57]. Other local deformation models are based on Markov fields [58]. Deformations may also be encoded in latent spaces through Convolutional Neural Networks (CNN) [59] or Generative Adversarial Network (GAN) [60]. Although these approaches are powerful, they require large amounts of data (for either training the Neural Network or statistically determining the deformation modes) and are computationally demanding. In this work, a parsimonious yet representative deformation model is proposed. It is based on the manufacturing process of turbine blades and has been designed in collaboration with experts in NDE for turbine blades who are familiar with the dimensional imperfections encountered in production lines.

It should be noted that, after step 3, simulated projections match observed ones up to geometrical indications. As a consequence, the projection residuals display the geometrical discrepancies (*i.e.* indications) between the manufactured (inspected) part and its ideal model. These discrepancies can be highlighted by comparing the residuals with the baseline value defining the noise level, introduced in step 0.

1.4.2 Structure of the dissertation

This dissertation, which aims at presenting the developed NDE process, is structured as follows:

- **Chapter 2** is dedicated to the study of acquisition noise, that is the noise polluting a projection. This analysis involves the characterization of the noise polluting a flat-field image, from which acquisition noise is derived. The latter is found to be Gaussian, white (spatially and temporally uncorrelated), and characterized by a deterministic variance. It is worth stressing that this variance reflects the structural heterogeneities of the detector that cannot be anticipated from first principles. These heterogeneities are thus to be characterized beforehand.

- **Chapter 3** details steps 1 to 3 of the procedure, namely the adjustment of the projection geometry and the estimation of the beam hardening and Compton scattering. A state of the art regarding these three aspects is first proposed. The developed approach, based on P-DVC, is introduced, and the results are presented and discussed. After these steps, a realistic projection operator is obtained. This chapter is extracted from [61].

- **Chapter 4** focuses on step 4 of the process, that is the deformation model derived from the manufacturing process of turbine blades. A discussion on wall thickness inspections is proposed. The parametric deformation model and the identification parameter methods are presented. The reliability of the approach is assessed through a repeatability study, with positive and encouraging results. This chapter is extracted from [62].

- **Chapter 5** offers a conclusion concerning the issues addressed in this work. Avenues for improvement are also suggested, and related works on the treated aspects are listed.

Complementary notes

Articles from published or submitted works are extended with complementary notes. The additional text is added in a blue frame, to avoid confusing it with the original article.

Bibliography

[1] Vistasp M. Karbhari. *Non-destructive evaluation (NDE) of polymer matrix composites*. Elsevier, 2013.

[2] Thierry Maffren. *Détection et caractérisation de fissures dans des aubes de turbine monocristallines pour l'évaluation de leurs durées de vie résiduelles*. PhD Thesis, Conservatoire national des arts et métiers-CNAM, 2013.

[3] David Lovejoy. *Magnetic particle inspection: a practical guide*. Springer, 2012.

[4] Javier García-Martín, Jaime Gómez-Gil, and Ernesto Vázquez-Sánchez. Non-destructive techniques based on eddy current testing. *Sensors*, 11(3):2525–2565, 2011. Publisher: Molecular Diversity Preservation International.

[5] Rémy Fransen. *LES based aerothermal modeling of turbine blade cooling systems*. PhD thesis, École normale supérieure de Cachan-ENS Cachan, 2013.

[6] Gerhard Hübschen, Iris Altpeter, Ralf Tschuncky, and Hans-Georg Herrmann. *Materials characterization using nondestructive evaluation (NDE) methods*. Woodhead publishing, 2016.

[7] Jesse Herrin, Nicholas Cardillo, Steve Timm, and Tom Rohlfing. Flaw detection capabilities in aerospace with eddy current array technology. In *NDE of Aerospace Materials & Structures 2018*, pages 44–52, 2018.

[8] Lesley M. Wright and Je-Chin Han. Enhanced internal cooling of turbine blades and vanes. *The gas turbine handbook*, 4:1–5, 2006.

[9] Kyung Min Kim, Suk Hwan Park, Yun Heung Jeon, Dong Hyun Lee, and Hyung Hee Cho. Heat/mass transfer characteristics in angled ribbed channels with various bleed ratios and rotation numbers. *Journal of Turbomachinery*, 130(3), 2008.

[10] Je-Chin Han, Sandip Dutta, and Srinath Ekkad. *Gas turbine heat transfer and cooling technology*. CRC press, 2012.

[11] Sumanta Acharya and Yousef Kanani. Chapter Three - Advances in Film Cooling Heat Transfer. In Ephraim M. Sparrow, John P. Abraham, and John M. Gorman, editors, *Advances in Heat Transfer*, volume 49, pages 91–156. Elsevier, 2017.

[12] Farah Nazifa Nourin and Ryoichi S. Amano. Review of gas turbine internal cooling improvement technology. *Journal of Energy Resources Technology*, 143(8), 2021.

[13] Dong Fei, David K. Hsu, and Mark Warchol. Simultaneous velocity, thickness and profile imaging by ultrasonic scan. *Journal of Nondestructive Evaluation*, 20(3):95–112, 2001.

[14] Renaldas Raisutis, Rymantas Kazys, and Liudas Mazeika. Ultrasonic Thickness Measurement of Multilayered Aluminum Foam Precursor Material. *IEEE Transactions on Instrumentation and Measurement*, 57(12):2846–2855, 2008.

[15] Shinnosuke Hirata, Minoru Kuribayashi Kurosawa, and Takashi Katagiri. Accuracy and resolution of ultrasonic distance measurement with high-time-resolution cross-correlation function obtained by single-bit signal processing. *Acoustical science and technology*, 30(6):429–438, 2009.

[16] Andrew J. C. Jarvis and Frederic B. Cegla. Application of the distributed point source method to rough surface scattering and ultrasonic wall thickness measurement. *The Journal of the Acoustical Society of America*, 132(3):1325–1335, 2012.

[17] Meng Lian, Haibo Liu, Tongyu Zhang, Qile Bo, Te Li, and Yongqing Wang. Ultrasonic on-machine scanning for thickness measurement of thin-walled parts: modeling and experiments. *The International Journal of Advanced Manufacturing Technology*, 104(5):2061–2072, 2019.

[18] Morana Mihaljević, Damir Markučič, Biserka Runje, and Zdenka Keran. Measurement uncertainty evaluation of ultrasonic wall thickness measurement. *Measurement*, 137:179–188, 2019.

[19] Pavel Müller. *Coordinate Metrology by Traceable Computed Tomography*. PhD thesis, Technical University of Denmark, Kgs. Lyngby, 2013.

[20] Leonardo De Chiffre, Simone Carmignato, Jean-Pierre Kruth, Robert Schmitt, and Albert Weckenmann. Industrial applications of computed tomography. *CIRP annals*, 63(2):655–677, 2014. Publisher: Elsevier.

[21] Thomas De Schryver, Jelle Dhaene, Manuel Dierick, Matthieu N. Boone, Eline Janssens, Jan Sijbers, Mattias van Dael, Pieter Verboven, Bart Nicolai, and Luc Van Hoorebeke. In-line NDT with X-Ray CT combining sample rotation and translation. *NDT & E International*, 84:89–98, 2016.

[22] Ronald S. Holt, Malcolm J. Cooper, and Daphne F. Jackson. Gamma-ray scattering techniques for non-destructive testing and imaging. *Nuclear Instruments and Methods in Physics Research*, 221(1):98–104, 1984.

[23] Joseph R. Lapinskas and Robert L. Kelly. Small Controlled Area Radiography–Fundamentals and Technology Advancements. In *ASNT Annual Conference 2017*, pages 101–110, 2017.

[24] Arthur Kevin Heller and Jack S. Brenizer. Neutron Radiography. In Hassina Z. Bilheux, Robert McGreevy, and Ian S. Anderson, editors, *Neutron Imaging and Applications: A Reference for the Imaging Community*, pages 67–80. Springer, 2009.

[25] Aaron E. Craft and John P. Barton. Applications of neutron radiography for the nuclear power industry. *Physics Procedia*, 88:73–80, 2017.

[26] Thorsten Buzug. *Computed Tomography : From Photon Statistics to Modern Cone-Beam CT*. Springer, 2008.

[27] Lee A. Feldkamp, Lloyd C. Davis, and James W. Kress. Practical cone-beam algorithm. *Journal of the Optical Society of America A*, 1(6):612–619, 1984.

[28] Marcel Beister, Daniel Kolditz, and Willi A. Kalender. Iterative reconstruction methods in X-ray CT. *Physica Medica*, 28(2):94–108, 2012.

[29] Ervin B. Podgoršak. *Radiation physics for medical physicists*, volume 1. Springer, 2006.

[30] Guillermo Hernández and Francisco Fernández. A model of tungsten anode x-ray spectra. *Medical Physics*, 43(8):4655–4664, 2016.

[31] Guillermo Hernández and Francisco Fernández. xpecgen: A program to calculate x-ray spectra generated in tungsten anodes. *J. Open Source Softw.*, 1(7):62, 2016.

[32] Rodney A. Brooks and Giovanni Di Chiro. Beam hardening in X-ray reconstructive tomography. *Physics in Medicine & Biology*, 21(3):390–398, 1976.

[33] William D. McDavid, Robert G. Waggener, William H. Payne, and Michael J. Dennis. Correction for spectral artifacts in cross-sectional reconstruction from x rays. *Medical physics*, 4(1):54–57, 1977.

[34] Robert E. Alvarez and Albert Macovski. Energy-selective reconstructions in x-ray computerised tomography. *Physics in Medicine & Biology*, 21(5):733, 1976.

[35] André J. Duerinckx and Albert Macovski. Polychromatic streak artifacts in computed tomography images. *Journal of Computer Assisted Tomography*, 2(4):481–487, 1978.

[36] Karsten Schörner. *Development of Methods for Scatter Artifact Correction in Industrial X-ray Cone-beam Computed Tomography*. PhD thesis, Technische Universität München, 2012.

[37] Martin J. Berger, John H. Hubbell, Stephen M. Seltzer, J. Chang, J. S. Coursey, R. Sukumar, D. S. Zucker, and K. Olsen. XCOM: Photon Cross Section Database (version 1.5), 2010.

[38] Soraia Rosa, Chris Connolly, Giuseppe Schettino, Karl T. Butterworth, and Kevin M. Prise. Biological mechanisms of gold nanoparticle radiosensitization. *Cancer nanotechnology*, 8(1):1–25, 2017. Publisher: BioMed Central.

[39] James E. Parks. The compton effect-compton scattering and gamma ray spectroscopy. *Department of Physics and Astronomy, The University of Tennessee Knoxville, Tennessee*, pages 37996–1200, 2015.

[40] Oskar Klein and Yoshio Nishina. Über die Streuung von Strahlung durch freie Elektronen nach der neuen relativistischen Quantendynamik von Dirac. *Zeitschrift für Physik*, 52(11):853–868, 1929.

[41] Hugo Leclerc, Stéphane Roux, and François Hild. Projection savings in CT-based digital volume correlation. *Experimental Mechanics*, 55(1):275–287, 2015.

[42] Thibault Taillandier Thomas. *Développement de la tomographie spatio-temporelle pour le suivi d'essais mécaniques*. PhD thesis, Université Paris Saclay (COmUE).

[43] Clement Jailin. *Projection-based in-situ 4D mechanical testing*. PhD thesis, Université Paris Saclay (COmUE), 2018.

[44] Wim Van Aarle, Willem Jan Palenstijn, Jeroen Cant, Eline Janssens, Folkert Bleichrodt, Andrei Dabravolski, Jan De Beenhouwer, Kees Joost Batenburg, and Jan Sijbers. Fast and flexible X-ray tomography using the ASTRA toolbox. *Optics express*, 24(22):25129–25147, 2016. Publisher: Optical Society of America.

[45] Vikas Patel, Rohit N. Chityala, Kenneth R. Hoffmann, Ciprian N. Ionita, Daniel R. Bednarek, and Stephen Rudin. Self-calibration of a cone-beam micro-CT system. *Medical Physics*, 36(1):48–58, 2008.

[46] Souhila Ouadah, Joseph Webster Stayman, Grace Jianan Gang, Tina Ehtiati, and Jeffrey Harold Siewerdsen. Self-calibration of cone-beam CT geometry using 3D–2D image registration. *Physics in Medicine & Biology*, 61(7):2613–2632, 2016.

[47] Van Nguyen, Jan De Beenhouwer, Joaquim G. Sanctorum, Sam Van Wassenbergh, Peter Aerts, Chris Van Ginneken, Joris J. J. Dirckx, and Jan Sijbers. A low-cost and easy-to-use phantom for cone-beam geometry calibration of a tomographic X-ray system. In *9th Conference on Industrial Computed Tomography, Padova, Italy (iCT 2019)*, 2019.

[48] Van Nguyen, Jan De Beenhouwer, Joaquim G. Sanctorum, Sam Van Wassenbergh, Shabab Bazrafkan, Joris J. J. Dirckx, and Jan Sijbers. A low-cost geometry calibration procedure for a modular cone-beam X-ray CT system. *Nondestructive Testing and Evaluation*, 35(3):252–265, 2020.

[49] Jianqiao Yu, Jian Lu, Yi Sun, Jishun Liu, and Kai Cheng. A geometric calibration approach for an industrial cone-beam CT system based on a low-rank phantom. *Measurement Science and Technology*, 33(3):035401, 2021.

[50] Victor Bussy and Caroline Vienne. Robust 3D/2D hybrid registration for integrating a priori CAD model into X-ray Computed Tomography. In *ORASIS 2021*, 2021.

[51] Alice Presenti, Shabab Bazrafkan, Jan Sijbers, and Jan De Beenhouwer. Deep learning-based 2D-3D sample pose estimation for X-ray 3DCT. In *10th Conference on Industrial Computed Tomography (ICT 2020)*, 2020.

[52] Elke Van de Casteele, Dirk Van Dyck, Jan Sijbers, and Erik Raman. A Model-Based Correction Method for Beam Hardening Artefacts in X-ray microtomography. *Journal of X-Ray Science and Technology*, 12(1):43–57, 2003.

[53] Maria Thomsen, Erik Bergbäck Knudsen, Peter Kjær Willendrup, Martin Bech, Marian Willner, Franz Pfeiffer, Mette Poulsen, Kim Lefmann, and Robert Feidenhans'l. Prediction of beam hardening artefacts in computed tomography using Monte Carlo simulations. *Nuclear Instruments and Methods in Physics Research Section B: Beam Interactions with Materials and Atoms*, 342:314–320, 2015.

[54] Chalinee Thanasupsombat, Saowapak S. Thongvigitmanee, Sorapong Aootaphao, and Pairash Thajchayapong. A Simple Scatter Reduction Method in Cone-Beam Computed Tomography for Dental and Maxillofacial Applications Based on Monte Carlo Simulation. *BioMed Research International*, 2018:1–15, 2018.

[55] Ammar Alsaffar, Gasim Mammadov, and Sven Simon. Scattering Correction of CBCT Projections for the Quality Enhanced CT Reconstruction Using an Efficient Monte Carlo Photon Transport Model. In *10th Conference on Industrial Computed Tomography, Wels, Austria (iCT 2020)*, 2020.

[56] Lane Alan Love and Robert A. Kruger. Scatter estimation for a digital radiographic system using convolution filtering. *Medical Physics*, 14(2):178–185, 1987.

[57] Marcel Lüthi, Thomas Gerig, Christoph Jud, and Thomas Vetter. Gaussian process morphable models. *IEEE transactions on pattern analysis and machine intelligence*, 40(8):1860–1873, 2017.

[58] Aristeidis Sotiras, Christos Davatzikos, and Nikos Paragios. Deformable medical image registration: A survey. *IEEE transactions on medical imaging*, 32(7):1153–1190, 2013.

[59] Shubham Tulsiani, Abhishek Kar, Joao Carreira, and Jitendra Malik. Learning category-specific deformable 3d models for object reconstruction. *IEEE transactions on pattern analysis and machine intelligence*, 39(4):719–731, 2016.

[60] Jiajun Wu, Chengkai Zhang, Tianfan Xue, Bill Freeman, and Josh Tenenbaum. Learning a probabilistic latent space of object shapes via 3d generative-adversarial modeling. *Advances in neural information processing systems*, 29, 2016.

[61] Cédric Fragnaud, Clément Remacha, Julián Betancur, and Stéphane Roux. CAD-based X-ray CT calibration and error compensation. *Measurement Science and Technology*, 33(6):065024, 2022.

[62] Cédric Fragnaud, Clément Remacha, Julián Betancur, and Stéphane Roux. Model-based dimensional NDE from few X-ray radiographs: Application to the evaluation of wall thickness in metallic turbine blades. Submitted to *Precision Engineering*.

Chapter 2

Noise quantification

Contents

This research project aims at identifying geometrical imperfections of an aeronautical part (turbine blade) from a limited number of X-ray images acquired with a CT-scanner. A methodology based on the numerical simulation of radiographic images is proposed to fulfill this objective. The projection residuals, *i.e.* the differences between the acquired and simulated projections, are used to identify the geometrical indications.

However, the acquired projections are polluted with noise, which must be considered. It is thus proposed to quantify and characterize the noise polluting a projection. This quantification allows a reference measure to be obtained for interpreting the projection residuals: residuals lower than the noise suggest a negligible difference, meaning that the numerical model matches the imaged part. Additionally, it would permit to formulate optimization problems designed to minimize the acquisition noise error.

The noise affecting a white field image is first investigated, from which the noise affecting a projection is derived. The approach adopted here is to build a simple yet accurate descriptive model of a flat-field image: any deviations from this model will be considered as noise.

2.1 Description of a flat-field image

A flat-field image $I_0(\boldsymbol{x})$ is defined as an image acquired by illuminating the detector with the source, with no sample in between (Figure 2.1). Ideally, a flat-field image is

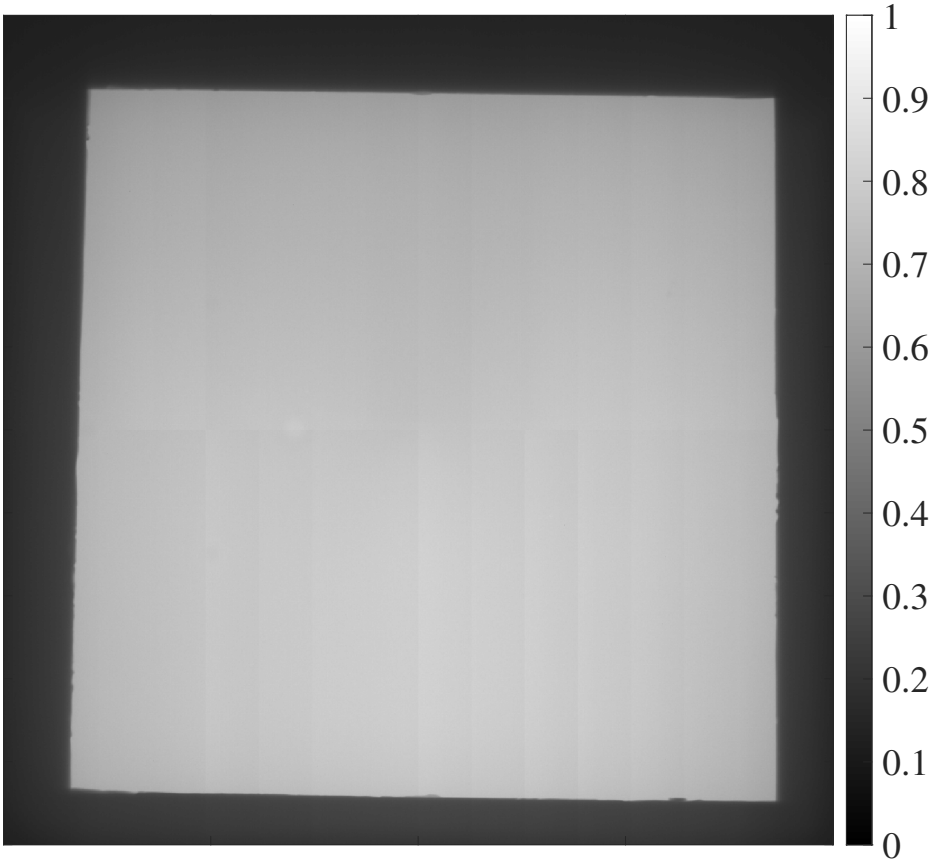

Figure 2.1: Example of a flat-field image $I_0(\boldsymbol{x})$. The obscured area corresponds to the area hidden by the collimator.

(spatially) homogeneous. However, due to the technology of the source (cone-beam geometry) and the structure of the detector (panel assembly), a dependence of the measured intensity on the pixel position $\boldsymbol{x} = (x_1, x_2)$ is observed. Additionally, the intensity of the X-ray beams emitted by the source varies over time, *e.g.* due to the progressive heating of the source. Although subtle, this fluctuation leads to a temporal dependency on the gray levels of a flat-field image. Hence, such an image is considered to be space-time dependent, *i.e.* $I_0(\boldsymbol{x}, t)$, where t denotes a time variable.

To establish the desired representation, a set of $N_t = 48$ flat-field images were collected, see Table 2.1 for the acquisition parameters. In the following, $I_0(\boldsymbol{x}, t)$ will represent the flat-field image acquired at a time index t. Their study was restricted to the areas not obscured by the collimator. Although derived from these specific flat-field images, the description presented in this section is expected to remain relevant for other sets of images as it is intended to be generic and adaptable.

Acceleration voltage	400 kV	Exposure time	354 ms
Tube current	725 μA	Encoding	16-bit uint

Table 2.1: Parameters for X-ray image acquisition using an XT H 450 (Nikon Metrology) with an XRD 1621 ES detector (Perkin Elmer).

2.1.1 Space-time decomposition

Theoretical development

A common approach to describe a space-time phenomenon consists of using model reduction methods that provide a low-dimensional description of the phenomenon.

Among the *a posteriori* reduction methods, one can mention the Proper Orthogonal Decomposition (POD) [1], also known as Principal Components Analysis (PCA) [2], Singular Value Decomposition (SVD) [3], or Karhunen-Loève Decomposition (KLD) [4], depending on the application. It relies on constructing optimal reduced basis functions using a separated representation. The flat-field is thus represented as a finite sum of M terms, called *modes*, expressed in the variables-separated form

$$I_0(\boldsymbol{x},t) \approx \sum_{m=1}^{M} a_m\ \Phi_m(\boldsymbol{x})\ \psi_m(t) \qquad \|\Phi_m\|_2^2 = \|\psi_m\|_2^2 = 1 \tag{2.1}$$

The principle of POD is restated here. Such a decomposition can be obtained by the extraction of one (the dominant) mode from the POD residual (*i.e.* raw signal from which all previous modes contributions have been subtracted). The principle of mode extraction is described for the first mode. The determination of a_1, Φ_1 and ψ_1 is done by minimizing

$$J\left(\Phi_1,\psi_1\right) = \left\|I_0(\boldsymbol{x},t) - a_1\ \Phi_1(\boldsymbol{x})\ \psi_1(t)\right\|_2^2 \tag{2.2}$$

Differentiating J with respect to Φ_1 and ψ_1 respectively, and setting the partial derivatives equal to 0, leads to

$$a_1\ \Phi_1(\boldsymbol{x}) = \sum_t I_0(\boldsymbol{x},t)\ \psi_1(t) \tag{2.3}$$

$$a_1\ \psi_1(t) = \sum_{\boldsymbol{x}} I_0(\boldsymbol{x},t)\ \Phi_1(\boldsymbol{x}) \tag{2.4}$$

Using the normalization

$$a_1 = \left\| \sum_{\boldsymbol{x}} I_0(\boldsymbol{x},t)\ \Phi_1(\boldsymbol{x}) \right\|_2 = \left\| \sum_t I_0(\boldsymbol{x},t)\ \psi_1(t) \right\|_2 \tag{2.5}$$

one gets

$$\Phi_1(\boldsymbol{x}) = \frac{1}{a_1} \sum_t I_0(\boldsymbol{x},t)\ \psi_1(t) \tag{2.6}$$

$$\psi_1(t) = \frac{1}{a_1} \sum_{\boldsymbol{x}} I_0(\boldsymbol{x},t)\ \Phi_1(\boldsymbol{x}) \tag{2.7}$$

The expressions of Φ_1 and ψ_1 given by (2.6) and (2.7) respectively imply

$$a_1^2\ \Phi_1(\boldsymbol{x}) = \sum_{\boldsymbol{x'}} \sum_{t} I_0(\boldsymbol{x}, t)\ I_0(\boldsymbol{x'}, t)\ \Phi_1(\boldsymbol{x'}) \tag{2.8}$$

$$a_1^2\ \psi_1(t) = \sum_{t'} \sum_{\boldsymbol{x}} I_0(\boldsymbol{x}, t)\ I_0(\boldsymbol{x}, t')\ \psi_1(t') \tag{2.9}$$

Introducing $F(\boldsymbol{x}, \boldsymbol{x'}) = \sum_t I_0(\boldsymbol{x}, t)\ I_0(\boldsymbol{x'}, t)$ and $G(t, t') = \sum_{\boldsymbol{x}} I_0(\boldsymbol{x}, t)\ I_0(\boldsymbol{x}, t')$, the problem amounts to an eigenvalue problem

$$F\ \Phi_1 = a_1^2\ \Phi_1 \tag{2.10}$$

$$G\ \psi_1 = a_1^2\ \psi_1 \tag{2.11}$$

where a_1^2 is the largest eigenvalue of F or G, and Φ_1 (resp. ψ_1) is the corresponding eigenvector of F (resp. G). Hence, either one of (2.10) or (2.11) can be solved, from which (2.6) or (2.7) will complement the determination of the space or time mode and amplitude. In practice, the smallest matrix size, either F or G, is considered.

Should one decide to compute a second mode, one would solve an identical problem for the residual but restricted to the subspace orthogonal to the mode. Given that all modes are orthogonal, Φ_2 (or equivalently ψ_2) would be the second eigenvector, *i.e.* a_2^2 would be the second largest eigenvalue of F or G. Thus an iterative algorithm is not necessary, and all the eigenvalues/eigenvectors can be readily obtained.

This decomposition allows the decoupling of the spatial variation of a flat-field image from the temporal one through a sparse and faithful representation.

Application

This decomposition is applied to the N_t observed images. The value a_m quantifies the energy of the m^{th} mode, *i.e.* its contribution to the decomposition. It is found that the first mode contains the majority of the energy of the decomposition achieved using eight modes ($> 99.5\%$, Table 2.2). Hence, only it is analyzed and used thereafter.

Mode number m	1	2	3	4	5	6	7	8
$\frac{a_m}{\sum_{j=1}^{8} a_j}$	0.9952	0.0007	0.0007	0.0007	0.0007	0.0007	0.0007	0.0007

Table 2.2: Relative energies of the POD modes (values rounded to 4 decimal places).

The first temporal mode $\psi_1(t)$, Figure 2.2a, shows a slight evolution that is attributed to the (minute) temporal fluctuation of the signal emitted by the X-ray source. The increasing nature of ψ_1 over time is explained by the progressive heating of the source. The first spatial mode $\Phi_1(\boldsymbol{x})$, Figure 2.2b, on the other hand, exhibits much more disparity resulting from the abovementioned points, namely the cone-beam geometry and the panel assembly. These factors are expressed in $\phi_1(\boldsymbol{x})$ through specific patterns:

- Cone-beam geometry of the source: the center of the detector being more illuminated than the edges, the corners (dark) contrast with the center (light), with a smooth gradient between the center and the corners.

- Panel assembly: the detector being made of several panels assembled together, horizontal and vertical streaks are visible.

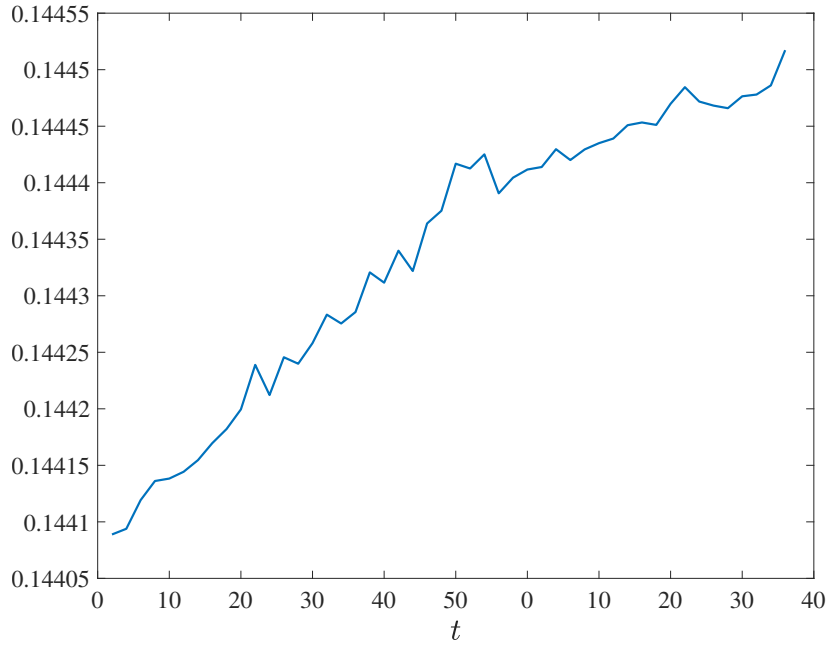

(a)

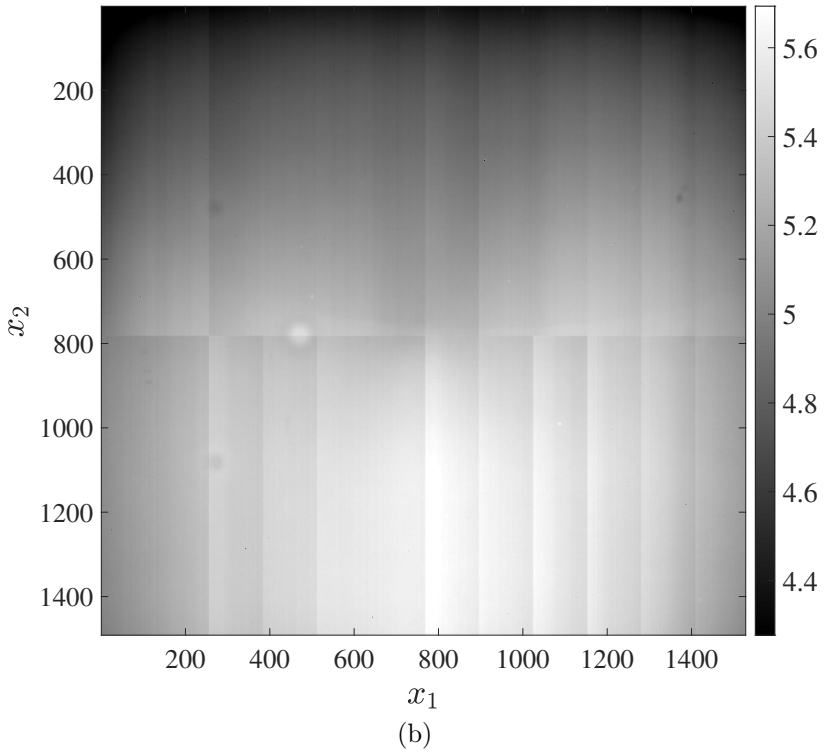

(b)

Figure 2.2: First mode of the POD of a flat-field image. (a) Temporal mode $\psi_1(t)$; (b) spatial mode $a_1\ \Phi_1(\boldsymbol{x})$. All the represented units correspond to greyscale values. The temporal mode fluctuates within a very narrow range of 3.10^{-3}.

Consequently, a more detailed description of the spatial mode is proposed. In order to keep a typical gray level value close to 1, we introduce ϕ_1 as

$$\phi_1 = \frac{\Phi_1}{\langle \Phi_1 \rangle_{\boldsymbol{x}}} \qquad \text{where} \quad \langle \cdot \rangle_{\boldsymbol{x}} = \frac{1}{N_{\boldsymbol{x}}} \sum_{\boldsymbol{x}} \cdot \tag{2.12}$$

with $N_{\boldsymbol{x}}$ the number of pixels.

2.1.2 Source-detector dissociation

The mode $\phi_1(\boldsymbol{x})$ reflects the spatial variation of a flat-field image due to the source and the detector. $\phi_1(\boldsymbol{x})$ is thus interpreted as being the product of two terms, $S(\boldsymbol{x})$ and $C(\boldsymbol{x})$, which are to be identified to improve the description of a flat-field image. $S(\boldsymbol{x})$ expresses the contribution of the source to the flat-field image, while $C(\boldsymbol{x})$ expresses the contribution of the detector. In the following, $S(\boldsymbol{x})$ and $C(\boldsymbol{x})$ are referred to as the *source* and *detector* terms, respectively.

A formulation of the identification problem is first established, leading to the computation of these terms. A sparse representation of the detector term is then proposed, which allows the estimation of $S(\boldsymbol{x})$ and $C(\boldsymbol{x})$ to be refined.

2.1.2.1 Identification of the source and detector terms

Theoretical development

The pattern characteristic to the technology of the source (dark/light contrast) can be captured by a smooth function $f(\boldsymbol{x}) \in \mathcal{V}$ with $\boldsymbol{x} = (x_1, x_2)$, *e.g.* a polynomial, where $\mathcal{V}$ denotes a function space.

The problem thus amounts to identifying the function $f(\boldsymbol{x})$ that best approximates $\phi_1(\boldsymbol{x})$ in the least-squares sense, assuming $C(\boldsymbol{x}) \equiv 1$ (perfect detector). This identification is described as

$$S = \underset{f \in \mathcal{V}}{\arg\min} \, \|\phi_1(\boldsymbol{x}) - f(\boldsymbol{x})\|_2^2 \tag{2.13}$$

Once the minimization problem (2.13) is solved, the detector term C is determined by

$$C(\boldsymbol{x}) = \frac{\phi_1(\boldsymbol{x})}{S(\boldsymbol{x})} \tag{2.14}$$

Application

Based on the shape of the surface associated with $\phi_1(\boldsymbol{x})$, Figure 2.3a, the function f found in eq. (2.13) is chosen as a polynomial of degree 2. The function S that minimizes this equation is shown in Figure 2.3b. The surface S captures the smooth variations of ϕ_1.

The image of $C(\boldsymbol{x})$ appears more homogeneous than the one associated with $\phi_1(\boldsymbol{x})$, see Figure 2.4. As expected, inhomogeneities due to the cone-beam geometry of the source (dark/light contrast) are imperceptible; only the streaks (characteristic of the detector) remain.

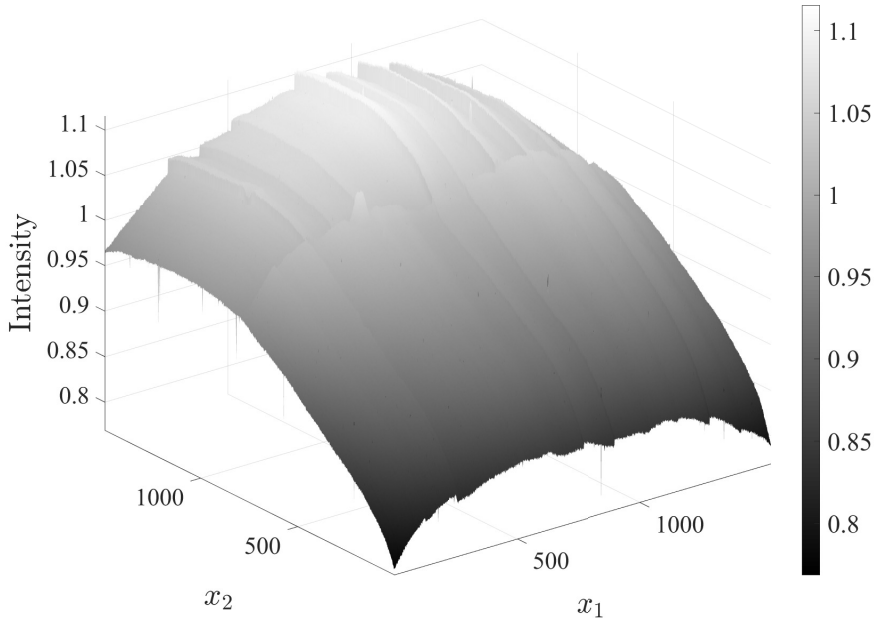

(a)

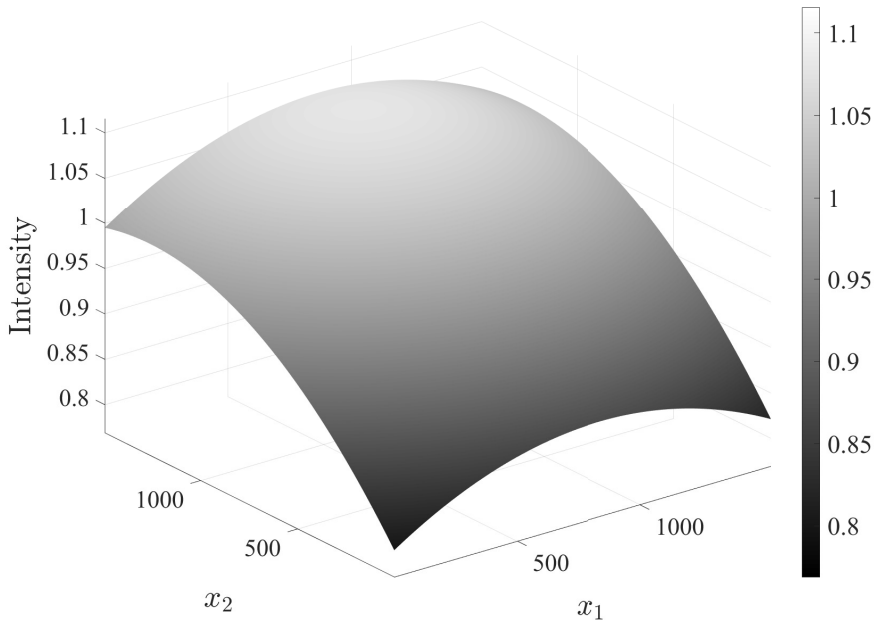

(b)

Figure 2.3: Comparison between the function $\phi_1(\boldsymbol{x})$ (a) and its fit by a polynomial of degree 2, $S(\boldsymbol{x})$ (b).

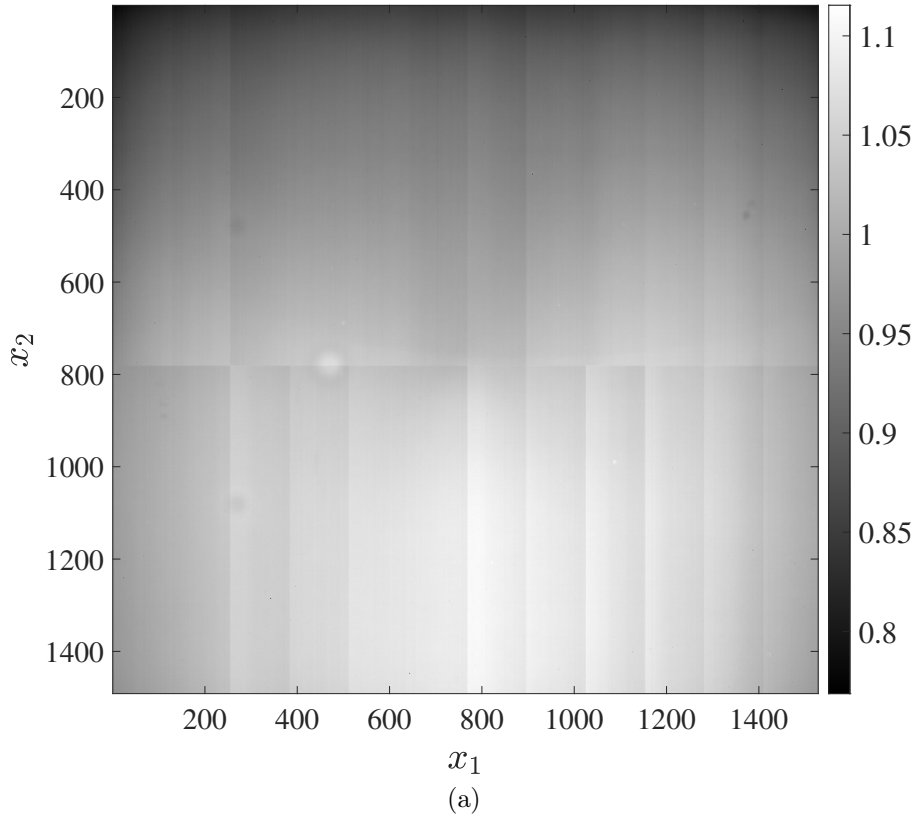

(a)

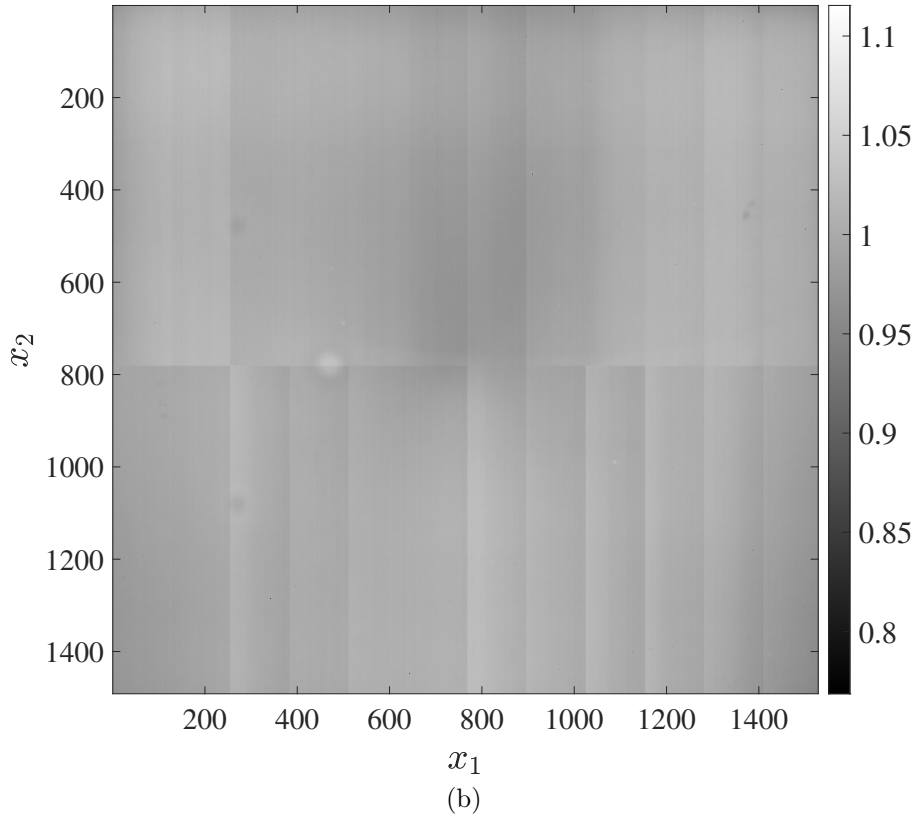

(b)

Figure 2.4: Comparison between (a) the function $\phi_1(\boldsymbol{x})$ and (b) the function $C(\boldsymbol{x})$ describing the contribution of the detector to the flat-field image.

2.1.2.2 Description of the detector term

Theoretical development

A further description of the detector term $C(\boldsymbol{x})$ with $\boldsymbol{x} = (x_1, x_2)$ is proposed. This description may be provided by a POD performed on C, as presented in Section 2.1.1.

However, vertical and horizontal streaks are visible in the detector term $C(\boldsymbol{x})$, Figure 2.4b. They are attributed to the detector (XRD 1621) being mounted in panels: two main panels (upper and lower parts of the detector), each composed of smaller panels placed side by side. As it is not natural to process the distinct areas (strips) delineated by these streaks together, several variants of the POD can be considered. Thus, the following variants are proposed:

1. Subdividing $C(x_1, x_2)$ in K domains Ω_k, one for each distinct panel (see Figure 2.5a), such that

$$C(x_1, x_2) = \sum_k \underbrace{C(x_1, x_2)\ \mathbb{1}_{\Omega_k}(x_1, x_2)}_{C_k(x_1, x_2)} \tag{2.15}$$

   where $\mathbb{1}$ denotes the indicator function. A POD is then performed on each function C_k

$$C_k(x_1, x_2) \approx \sum_{l=1}^{L} b_{kl}\ \varphi_{kl}(x_1)\ \omega_{kl}(x_2) \qquad \|\varphi_{kl}\|_2^2 = \|\omega_{kl}\|_2^2 = 1 \tag{2.16}$$

2. Subdividing $C(x_1, x_2)$ in two domains Ω_T and Ω_B, representing the upper and lower halves (see Figure 2.5b), such that

$$C(x_1, x_2) = \underbrace{C(x_1, x_2)\ \mathbb{1}_{\Omega_B}(x_2)}_{C_B(x_1, x_2)} + \underbrace{C(x_1, x_2)\ \mathbb{1}_{\Omega_T}(x_2)}_{C_T(x_1, x_2)} \tag{2.17}$$

   A POD is then performed on the functions C_B and C_T

$$C_B(x_1, x_2) \approx \sum_{l=1}^{L} b_{Bl}\ \varphi_{Bl}(x_1)\ \omega_{Bl}(x_2) \qquad \|\varphi_{Bl}\|_2^2 = \|\omega_{Bl}\|_2^2 = 1 \tag{2.18}$$

$$C_T(x_1, x_2) \approx \sum_{l=1}^{L} b_{Tl}\ \varphi_{Tl}(x_1)\ \omega_{Tl}(x_2) \qquad \|\varphi_{Tl}\|_2^2 = \|\omega_{Tl}\|_2^2 = 1 \tag{2.19}$$

One would note that variant n°2 corresponds to a particular case of the variant n°1 for which a single x_2-mode is shared between all panels of a given half.

Application

The spots visible in the image $C(\boldsymbol{x})$, *e.g.* at $(x_1, x_2) \approx (500, 800)$, are hardly explainable with a POD. Therefore, we chose to mask them and perform a Gappy-POD instead [5, 6, 7, 8]. The latter is a modified version of the POD developed to address the case where the function to be decomposed includes missing information.

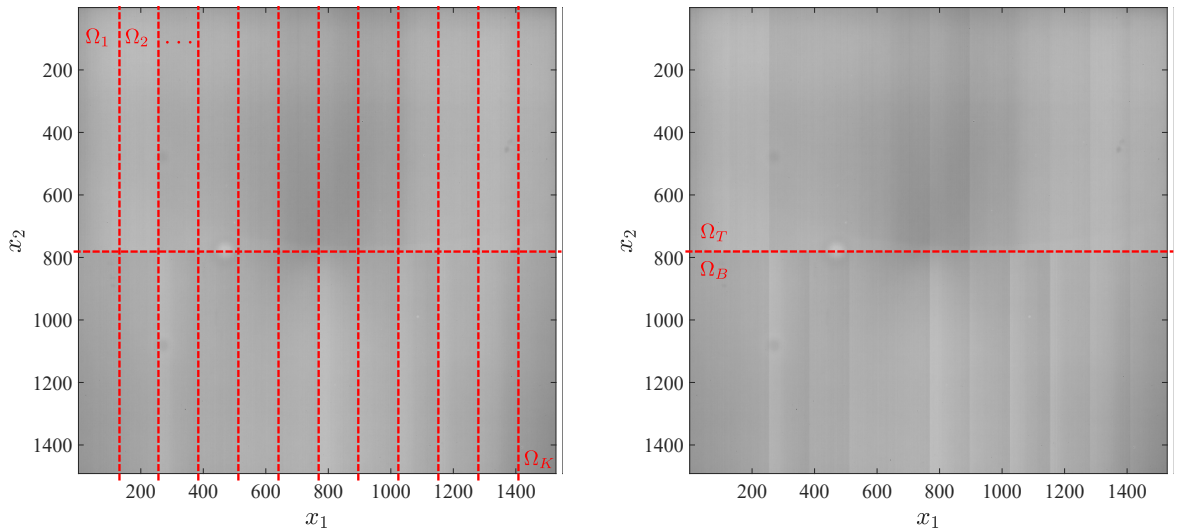

(a) (b)

Figure 2.5: Visualization of the subdivisions for (a) the first variant, and (b) the second variant of the POD.

Multiple algorithms or variants implementing the Gappy-POD have been designed, the difference lying in the way the missing data are interpolated. In this work, an algorithm found to yield good results, both in terms of quality results and convergence speed, with sparse and noisy data was utilized [9].

Variants 1 and 2 of the POD have been evaluated with a single mode, *i.e.* $L = 1$, using the Gappy version. The associated modes are presented in Figures 2.6 and 2.7.

Two remarks are to be made regarding the x_2-modes $\omega_{k1}(x_2)$: (i) the average profile of the upper part clearly differs from that of the lower part, and (ii) for a given half, the x_2-mode have a similar trend. These observations are explained by the operation of the detector. Indeed, its specifications state that (i) the upper and the lower parts are electrically separated and (ii) the data of each half is transferred by so-called *read out groups* (previously introduced as *panels*) that successively scan the sensor columns.

As expected, the first variant provides a more accurate approximation. Indeed, this approximation captures fine details since less constraints are enforced (more flexibility for the x_2-modes). However, this approximation is considered as over-fitting, in the sense that it might also capture noise, which we are trying to extract. Hence, the second variant was retained and used in the following. This choice is supported by the clear tendency existing for the average profile of $\omega_{k1}(x_2)$ (Figure 2.6b), which suggests a common x_2-mode for each given half.

An additional hybrid variant has been investigated and is here briefly presented. For each half, the x_2-modes $\omega_{k1}(x_2)$ are similar (Figure 2.6b). This reflects the fact that, within each bloc Ω_k, the intensity of $C(x_1, x_2)$ seems not to evolve significantly with x_2. Hence, a hybrid variant is given by:

3. Subdividing $C(x_1, x_2)$ in K domains Ω_k, one for each distinct panel, yielding the same expression as eq. (2.15). A (very degenerated) POD on each function C_k is performed, with the x_2-modes $\omega_{kl}(x_2)$ constant, *i.e.* $\omega_{kl}(x_2) = \omega_{kl}$ such that

$\|\omega_{kl}\|_2 = 1$:

$$C_k(x_1, x_2) \approx \sum_{l=1}^{L} b_{kl}\ \varphi_{kl}(x_1)\ \omega_{kl} = \sum_{l=1}^{L} c_{kl}\ \varphi_{kl}(x_1) \qquad \|\varphi_{kl}\|_2^2 = 1 \tag{2.20}$$

The associated modes are presented in Figure 2.8. This variant has not been selected for the description as it does not fit the detector term well enough, *i.e.* the fitting residuals were too high.

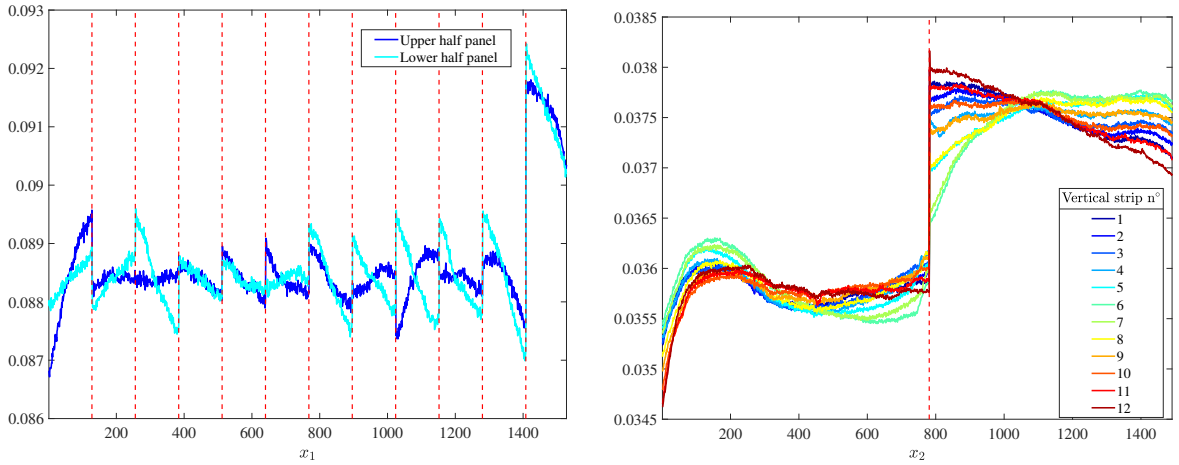

(a) (b)

Figure 2.6: Modes of the POD of C using the first variant. (a) x_1-modes given by $\varphi_{k1}(x_1)$. The dash-lines represent the separation between the various vertical strips of C (delineated by the vertical streaks). (b) x_2-modes given by $\omega_{k1}(x_2)$. The dash-line represents the separation between the upper and lower-half of C (delineated by the horizontal streak).

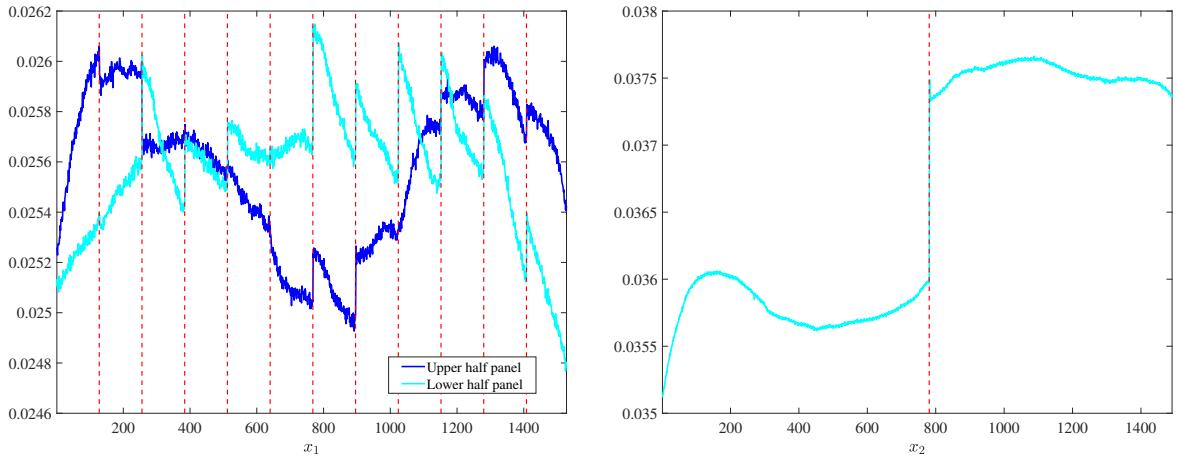

(a) (b)

Figure 2.7: Modes of the POD of C using the second variant. (a) x_1-modes given by $\varphi_{B1}(x_1)$ and $\varphi_{T1}(x_1)$. The dash-lines represent the separation between the various vertical strips of C (delineated by the vertical streaks). (b) x_2-modes given by $\omega_{B1}(x_2)$ and $\omega_{T1}(x_2)$. The dash-line represents the separation between the upper and lower-half of C (delineated by the horizontal streak).

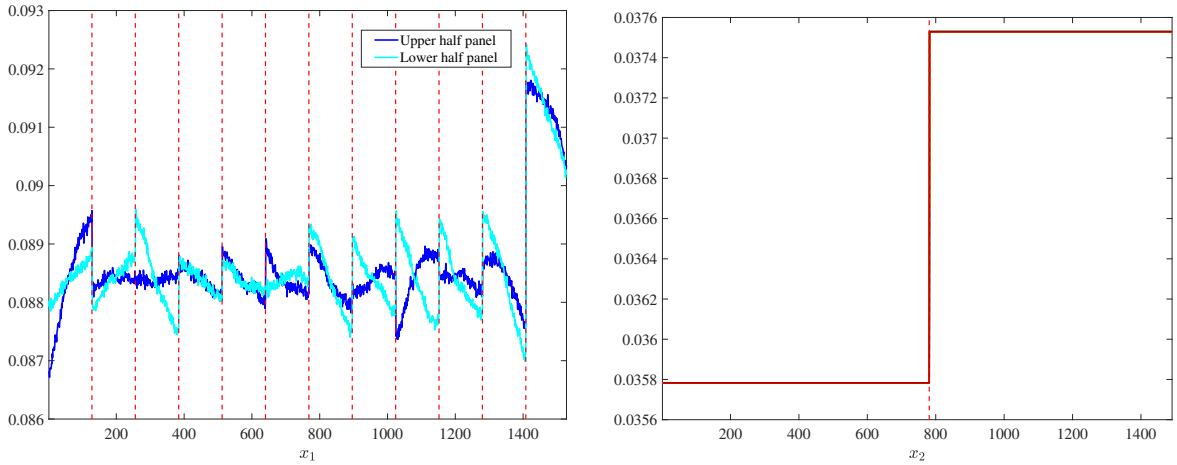

(a) (b)

Figure 2.8: Modes of the POD of C using the third (additional) variant. (a) x_1-modes given by $\varphi_{k1}(x_1)$. The dash-lines represent the separation between the various vertical strips of C (delineated by the vertical streaks). (b) x_2-modes given by $\omega_{k1}(x_2)$. The dash-line represents the separation between the upper and lower-half of C (delineated by the horizontal streak).

2.1.2.3 Refinement of estimation

Theoretical development

Let $\widehat{C}$ denote the approximation of the detector term C by its POD using one of the variants above presented. S may be recalculated as

$$S = \underset{f \in \mathcal{V}}{\arg\min} \left\| \phi_1(\boldsymbol{x}) - \widehat{C}(\boldsymbol{x})\, f(\boldsymbol{x}) \right\|_2^2 \tag{2.21}$$

An iterative algorithm, described in Algorithm 1, is derived.

Algorithm 1: Refinement of source and detector terms

Data: Spatial mode $\phi_1(\boldsymbol{x})$
Result: Source and detector terms, $S(\boldsymbol{x})$ and $C(\boldsymbol{x})$, and $\widehat{C}(\boldsymbol{x})$
Compute $S(\boldsymbol{x})$ using eq. (2.13) ; ▷ `Initialization`
do
  Set $C(\boldsymbol{x}) = \phi_1(\boldsymbol{x})/S(\boldsymbol{x})$;
  Compute $\widehat{C}(\boldsymbol{x})$ by the POD of $C(\boldsymbol{x})$;
  Compute $S(\boldsymbol{x})$ by resolving eq. (2.21);
while *Convergence criterion met*;

This algorithm ultimately leads to the identification of the source and detector terms, $S(\boldsymbol{x})$ and $C(\boldsymbol{x})$, together with the POD approximation of $C(\boldsymbol{x})$ denoted $\widehat{C}(\boldsymbol{x})$, that best represent the spatial mode $\phi_1(\boldsymbol{x})$.

Application

To refine the estimation of S and C, the algorithm 1 was applied. It was proposed to enrich the description by a new choice for f, namely a polynomial of degree 4. Finally, the difference between C and its approximation $\widehat{C}$, Figure 2.9, indicates that an accurate and faithful description has been achieved. For comparison purposes, the same difference $C - \widehat{C}$, but for which $\widehat{C}$ is approximated using variant n°1 (resp. n°3), is shown in Figure 2.10 (resp. Figure 2.11).

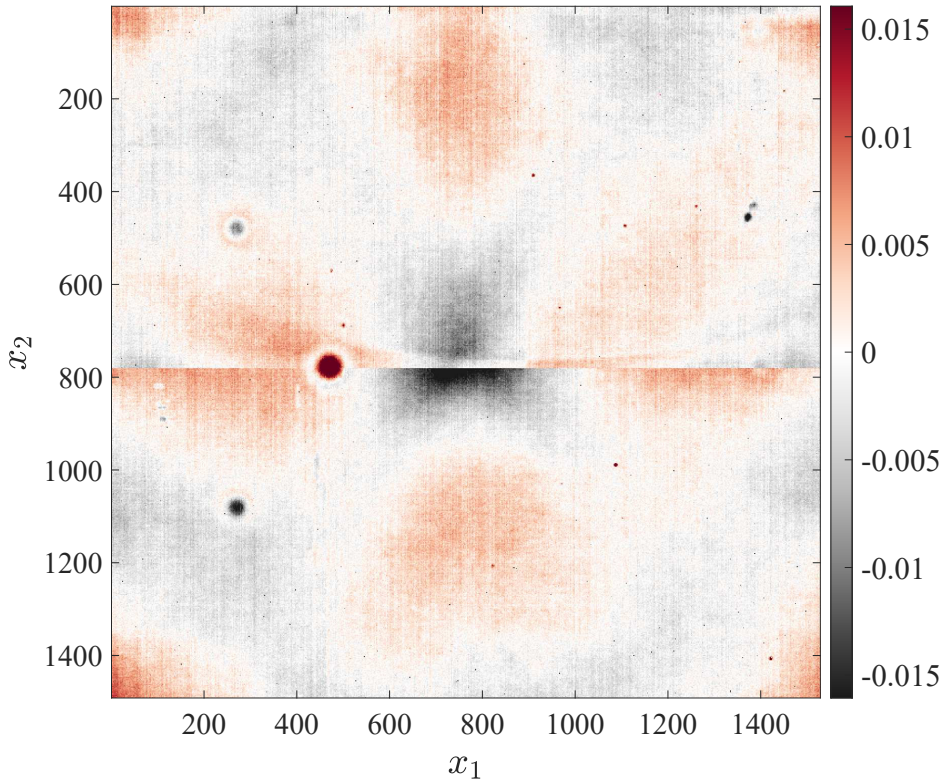

Figure 2.9: Difference between C and $\widehat{C}$ after the proposed refinement step. As $\phi_1 = S\,C$, this figure also represents the difference between ϕ_1 and its approximation given by $S\,\widehat{C}$.

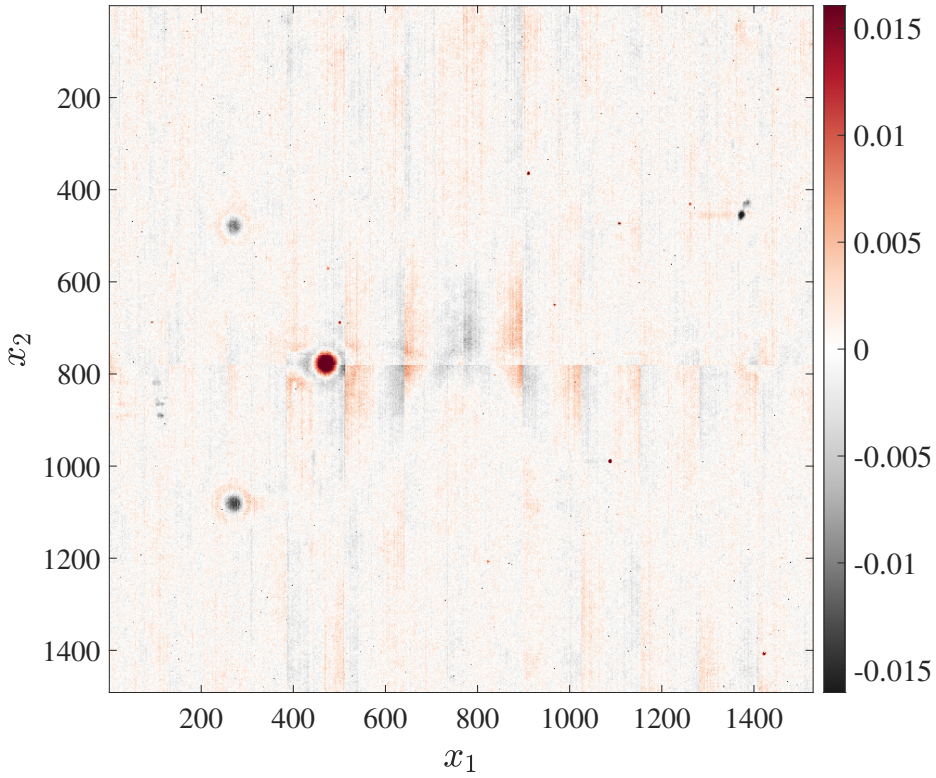

Figure 2.10: Difference between C and $\widehat{C}$ after the proposed refinement step, using the first variant of the POD.

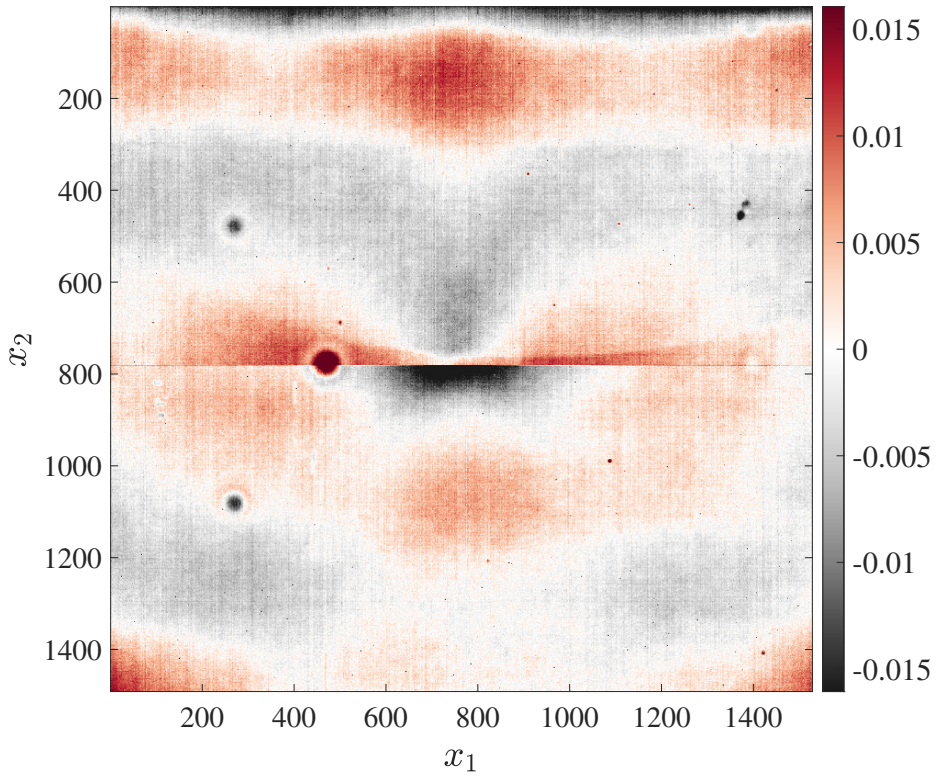

Figure 2.11: Difference between C and $\widehat{C}$ after the proposed refinement step, using the third (additional) variant of the POD.

2.2 Noise in a flat-field image

Based on the previous description of a flat field-image, an approximation of $I_0(\boldsymbol{x}, t)$ is given by

$$\widehat{I}_0(\boldsymbol{x}, t) = a_1 \, \langle \Phi_1 \rangle_{\boldsymbol{x}} \, S(\boldsymbol{x}) \, \widehat{C}(\boldsymbol{x}) \, \psi_1(t) \tag{2.22}$$

where $\widehat{C}$ is computed using the second variant. The measured signal unexplained by the previous description is contained in the fitting residuals $\rho(\boldsymbol{x}, t) = \widehat{I}_0(\boldsymbol{x}, t) - I_0(\boldsymbol{x}, t)$ (Figure 2.12). It should be emphasized that, as ψ_1 is almost constant, the temporal fluctuation of ρ is nearly the same as that of I_0, which corresponds to the natural definition of the noise. Hence, ρ contains the fitting residuals as well as the noise.

In this subsection, it is proposed to study the properties of this noise ρ, specifically its variance, normality, and whiteness.

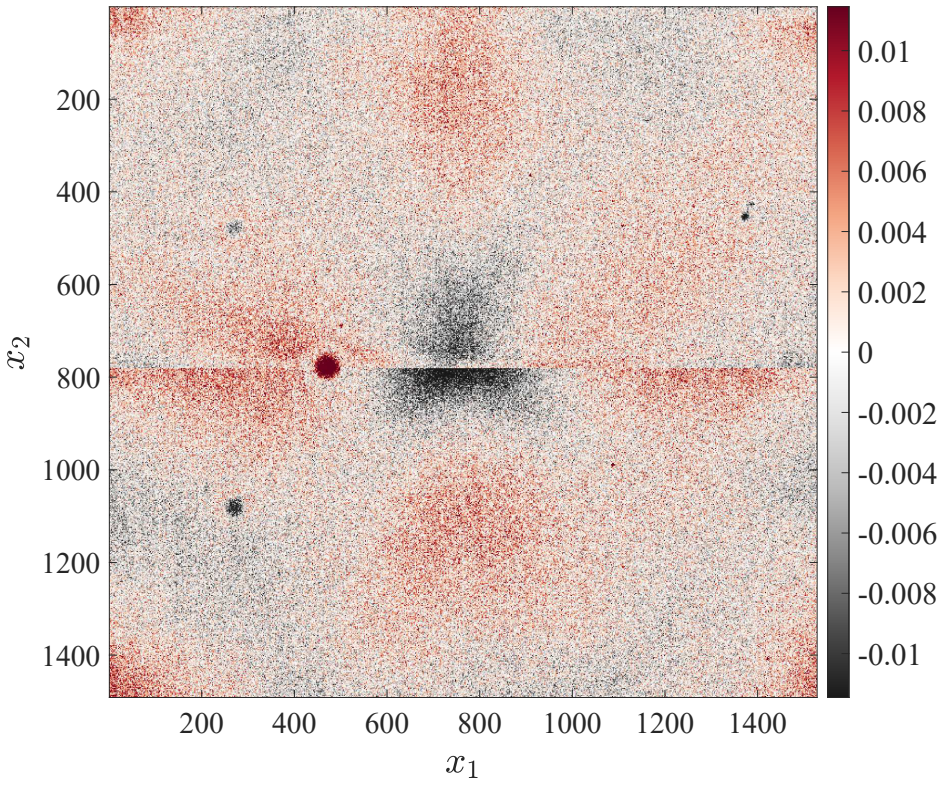

Figure 2.12: Fitting residual $\rho(\boldsymbol{x}, t)|_{t=1}$, *i.e.* difference between our description of a flat-field image and an observed one.

2.2.1 Variance

The noise variance is given by $V_\rho(\boldsymbol{x}) := \mathrm{Var}_t\,(\rho(\boldsymbol{x}, t))$. Figure 2.13 indicates that the analyzed flat-field images are similar to one another (low dynamic range, in the order of 10^{-5}). The low standard deviation of the noise attests to the need to account for the phenomena underlying image formation (beam hardening, Compton scattering) which produce imaging artifacts more significant and visible than the noise.

The image $V_\rho(\boldsymbol{x})$, Figure 2.14a, very subtly exhibits a grid structure, similar to the one observed in Figure 2.4b. In addition, the upper right and left edges are darker,

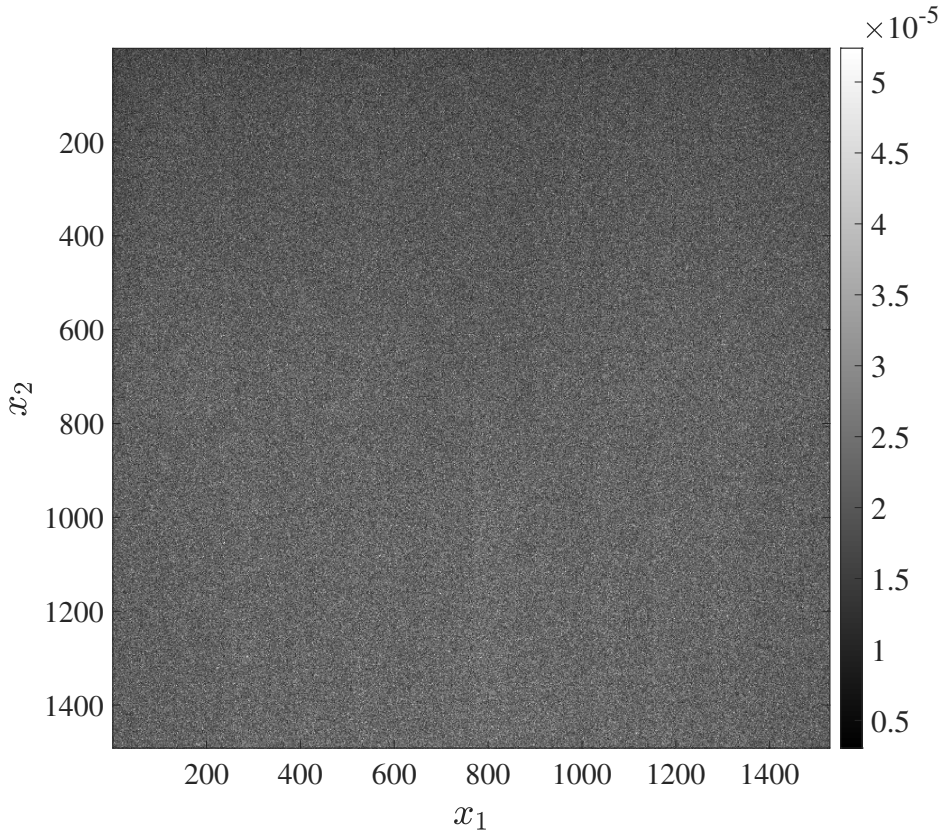

Figure 2.13: Relative noise variance $V_\rho(\boldsymbol{x})/\langle M\rangle_{\boldsymbol{x}}^2$, where $M(\boldsymbol{x})$ denotes the mean flat-field image.

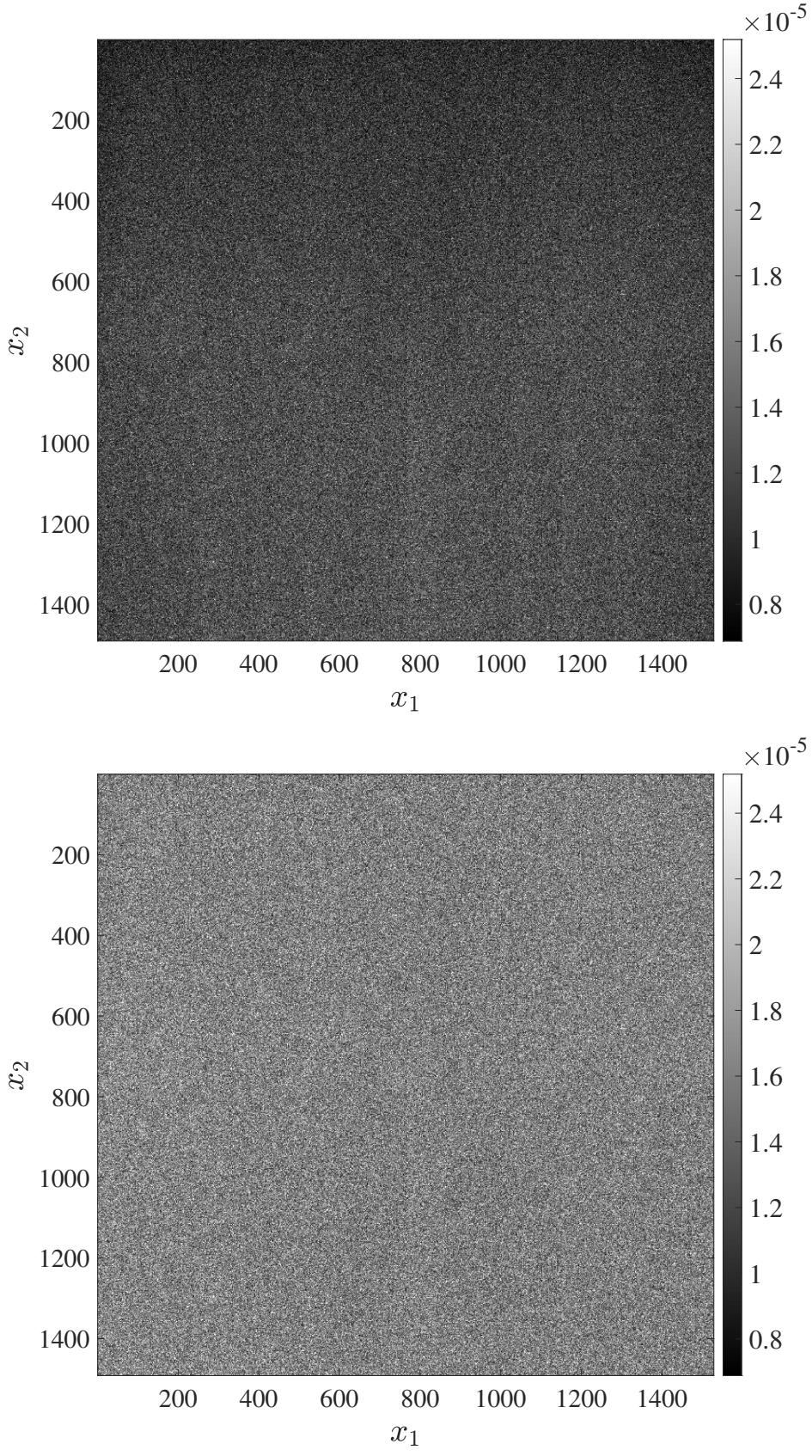

Figure 2.14: Comparison between (a) $V_\rho(\boldsymbol{x})$ and (b) $V_\rho^M(\boldsymbol{x})$. The latter appears to be more homogeneous.

and the bottom right is (slightly) lighter. These two patterns are particularly visible in the first spatial mode $\phi_1(\boldsymbol{x})$ of the POD of $I_0(\boldsymbol{x}, t)$, or equivalently in the mean flat-field image $M(\boldsymbol{x}) := \langle I_0(\boldsymbol{x}, \cdot)\rangle_t$. This observation suggests a dependence of $M(\boldsymbol{x})$ on $V_\rho(\boldsymbol{x})$. Thus, we considered $V_\rho^M(\boldsymbol{x}) := V_\rho(\boldsymbol{x})/M(\boldsymbol{x})$ and compared it to $V_\rho(\boldsymbol{x})$.

$V_\rho^M(\boldsymbol{x})$ appears to be more homogeneous than $V_\rho(\boldsymbol{x})$ (Figure 2.14b). This can be quantitatively established by computing the intercorrelation coefficient between V_ρ and M on the one hand, γ_1, and between V_ρ^M and M on the other hand, γ_2. As a reminder, the intercorrelation coefficient between two images A and B is given by

$$\gamma = \frac{\sum_{\boldsymbol{x}'} \left[A(\boldsymbol{x}') - \langle A\rangle_{\boldsymbol{x}}\right]\left[B(\boldsymbol{x}') - \langle B\rangle_{\boldsymbol{x}}\right]}{\sqrt{\sum_{\boldsymbol{x}'} \left[A(\boldsymbol{x}') - \langle A\rangle_{\boldsymbol{x}}\right]^2 \sum_{\boldsymbol{x}'} \left[B(\boldsymbol{x}') - \langle B\rangle_{\boldsymbol{x}}\right]^2}} \tag{2.23}$$

We get $\gamma_1 \approx 0.313$ and $\gamma_2 \approx 0.011$, meaning that V_ρ^M is much less correlated to M than V_ρ is (almost by a factor of 30). This result indicates that, at a pixel $\boldsymbol{x}$ of a flat-field image, the noise variance $V_\rho(\boldsymbol{x})$ is proportional to $M(\boldsymbol{x})$. In order to estimate the factor linking these two quantities, we compute $\sigma^2 := \left\langle V_\rho^M \right\rangle_{\boldsymbol{x}} \approx 1.69\text{e-}5$. Thus, the noise variance is given by $V_\rho(\boldsymbol{x}) = \sigma^2 M(\boldsymbol{x})$.

The images $f_t(\boldsymbol{x})$ defined by

$$f_t(\boldsymbol{x}) = \frac{I_0(\boldsymbol{x}, t) - M(\boldsymbol{x})}{\sigma\sqrt{M(\boldsymbol{x})}} \tag{2.24}$$

thus represent the realization of noise, normalized by its standard deviation.

2.2.2 Normality

The Gaussian nature of the noise is investigated by considering the statistical distribution of $f_t(\boldsymbol{x})$. Figure 2.15 displays the probability density function (PDF) estimate of the noise given by the values $f_t(\boldsymbol{x})$ (blue rectangles). The PDF of the standard normal distribution (red curve) is superimposed over these rectangles. The perfect match suggests that the noise follows the Gaussian distribution of zero mean. This normality was quantitatively confirmed through the computation of the skewness and kurtosis, respectively the third and fourth standardized moment, for each image $f_t(\boldsymbol{x})$. The normal distribution is characterized by a zero skewness and a kurtosis equal to 3. The minor difference between these values and those calculated, summarized in Table 2.3, supports our assumption.

	Average value
Skewness	0.01
Kurtosis	3.00

Table 2.3: Average value of skewness and kurtosis of $f_t(\boldsymbol{x})$ (values rounded to two decimal places).

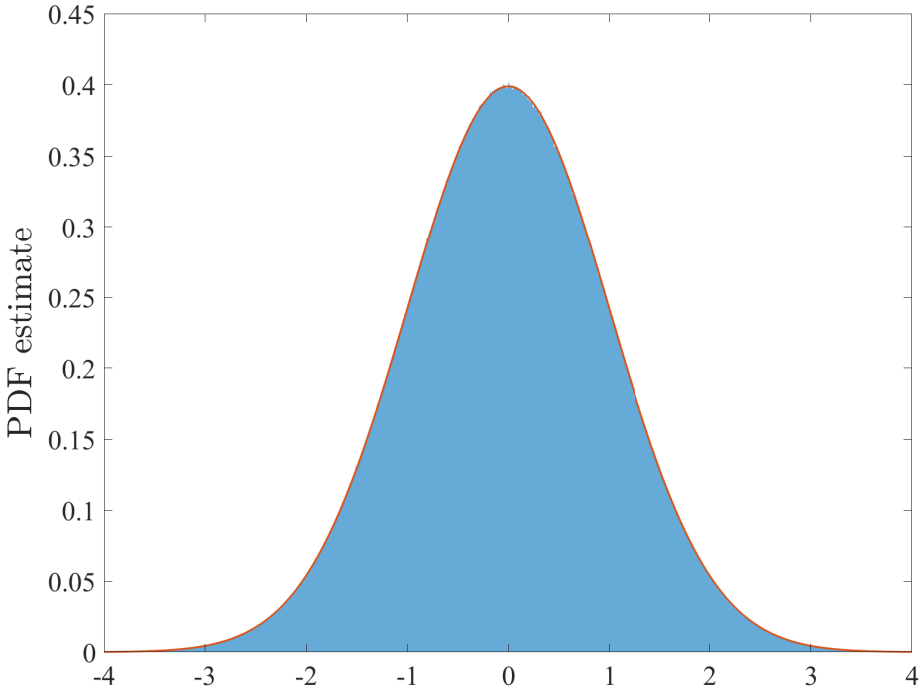

Figure 2.15: Statistical distribution of $f_t(\boldsymbol{x})$.

2.2.3 White noise

The whiteness of the noise is determined by calculating the autocorrelation functions $\Gamma_t(\boldsymbol{u})$

$$\Gamma_t(\boldsymbol{u}) = \frac{1}{N_{\boldsymbol{x}}} \sum_{\boldsymbol{x'}} \left[f_t(\boldsymbol{x'}) - \langle f_t \rangle_{\boldsymbol{x}} \right] \left[f_t(\boldsymbol{x'} - \boldsymbol{u}) - \langle f_t \rangle_{\boldsymbol{x}} \right] \tag{2.25}$$

with $\boldsymbol{u} = (u, v)$. An example of such a function is displayed in Figure 2.16. A null autocorrelation is observed everywhere, except at the origin $\boldsymbol{u} = (0, 0)$ (and at the four adjacent pixels, to a lesser extent). This observation indicates that two noise values measured at two distinct pixel positions are uncorrelated, meaning that the noise is white.

Eventually, the noise polluting a flat-field image $I_0(\boldsymbol{x})$ is gaussian, white, and with a variance $V(\boldsymbol{x}) = \sigma^2 M(\boldsymbol{x})$, where $M(\boldsymbol{x})$ denotes the noiseless flat-field image.

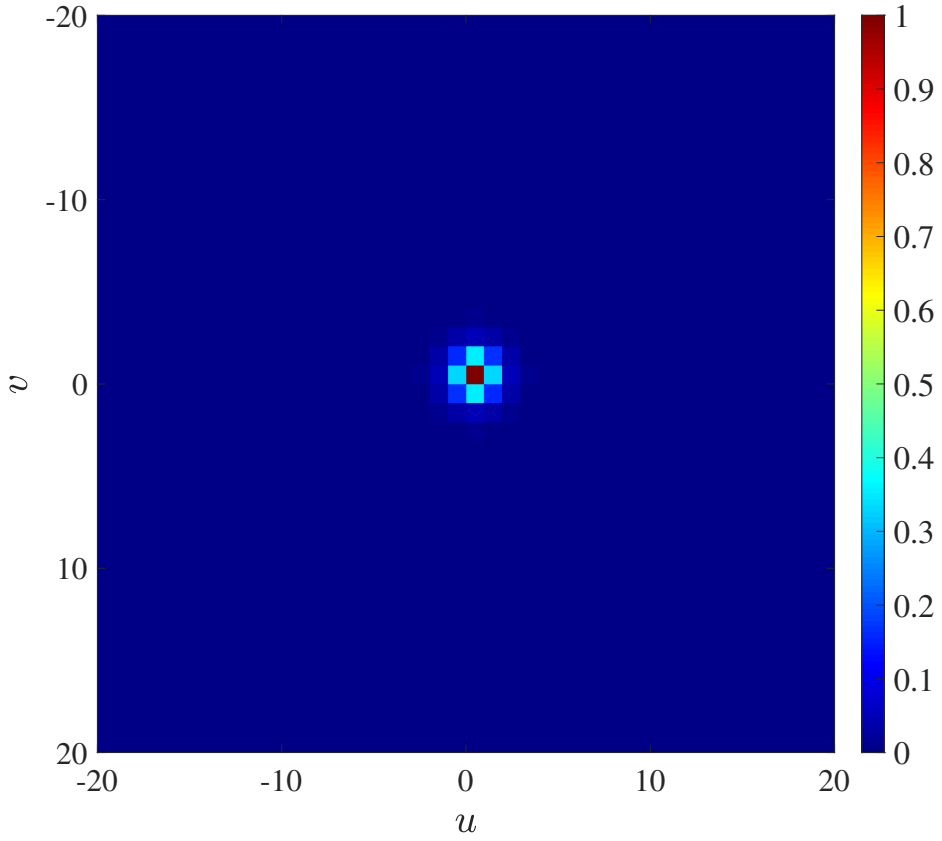

Figure 2.16: $\Gamma_t(\boldsymbol{u})$ for $t = 1$. A peak is observed at the origin, *i.e.* for $\boldsymbol{u} = (0, 0)$.

2.3 Noise in a radiographic image

The noise polluting the logarithm of the radiographic image $I(\boldsymbol{x})$ normalized by the flat-field image $I_0(\boldsymbol{x})$ is given by

$$\begin{aligned}
\ln\left(\widetilde{I}(\boldsymbol{x})\right) &= \ln\left(\frac{I(\boldsymbol{x})}{I_0(\boldsymbol{x})}\right) + \ln\left(\frac{1+\dfrac{\eta_I(\boldsymbol{x})}{I(\boldsymbol{x})}}{1+\dfrac{\eta_{I_0}(\boldsymbol{x})}{I_0(\boldsymbol{x})}}\right) \\
&= -P(\boldsymbol{x}) + \ln\left(1+\frac{\eta_I(\boldsymbol{x})}{I(\boldsymbol{x})}\right) - \ln\left(1+\frac{\eta_{I_0}(\boldsymbol{x})}{I_0(\boldsymbol{x})}\right) \\
&\simeq -P(\boldsymbol{x}) + \frac{\eta_I(\boldsymbol{x})}{I(\boldsymbol{x})} - \frac{\eta_{I_0}(\boldsymbol{x})}{I_0(\boldsymbol{x})}
\end{aligned} \tag{2.26}$$

which has been obtained by applying a first order approximation of the attenuation, and where $\eta_I(\boldsymbol{x})$, resp. $\eta_{I_0}(\boldsymbol{x})$, denotes the noise contained in $I(\boldsymbol{x})$, resp. $I_0(\boldsymbol{x})$. The first term of eq. (2.26) corresponds to the noiseless normalized projection (better known as the attenuation image). The second and third term represent the noise due to the radiographic image $I(\boldsymbol{x})$ and to the flat-field image $I_0(\boldsymbol{x})$, respectively.

Using the results from the previous section, the noise $\eta = \dfrac{\eta_I}{I} - \dfrac{\eta_{I_0}}{I_0}$ polluting

$\ln\left(\frac{I}{I_0}\right)$ is expected to be white, gaussian, with a variance equal to

$$\mathrm{Var}\left(\frac{\eta_I}{I}\right) + \mathrm{Var}\left(\frac{\eta_{I_0}}{I_0}\right) = \sigma^2\left(\frac{1}{I} + \frac{1}{I_0}\right) \tag{2.27}$$

These properties need to be verified experimentally. A set of projections, denoted $P^n(\boldsymbol{x})$, representing the same (static) object has been acquired. The mean, noiseless, projection is defined as $N(\boldsymbol{x}) := \langle P^n(\boldsymbol{x})\rangle_n$. The noise of the projections is contained in the residuals

$$\rho^n(\boldsymbol{x}) := P^n(\boldsymbol{x}) - N(\boldsymbol{x}) \tag{2.28}$$

The theoretical variance of this noise is to be compared to the experimental one, and its Gaussian and white nature investigated.

2.3.1 Variance

The variance of the noise, given by $V(\boldsymbol{x}) := \mathrm{Var}_n\left(P^n(\boldsymbol{x})\right)$, is calculated and compared with

$$V_{\mathrm{th}}(\boldsymbol{x}) = \sigma^2\left(\frac{1}{I(\boldsymbol{x})} + \frac{1}{M(\boldsymbol{x})}\right) \tag{2.29}$$

where $I(\boldsymbol{x}) = M(\boldsymbol{x})\exp\left(-N(\boldsymbol{x})\right)$ represents the noiseless X-ray image. Fig. 2.17 displays the comparison between the theoretical and experimental results for the noise variance. Although discrepancies are observed, particularly in areas of high thicknesses, the agreement is satisfactory. Applying a small multiplicative factor of 1.3 on the gray levels of V_{th} provides an even better agreement. This factor, however, is identified manually, *i.e.* independently from the results of the discussions from Sections 2.1 and 2.2.

In the same way as above, the images $g_n(\boldsymbol{x})$ defined by

$$g_n(\boldsymbol{x}) = \frac{P^n(\boldsymbol{x}) - N(\boldsymbol{x})}{\sqrt{V_{\mathrm{th}}(\boldsymbol{x})}} \tag{2.30}$$

represent the realization of noise, normalized by its standard deviation.

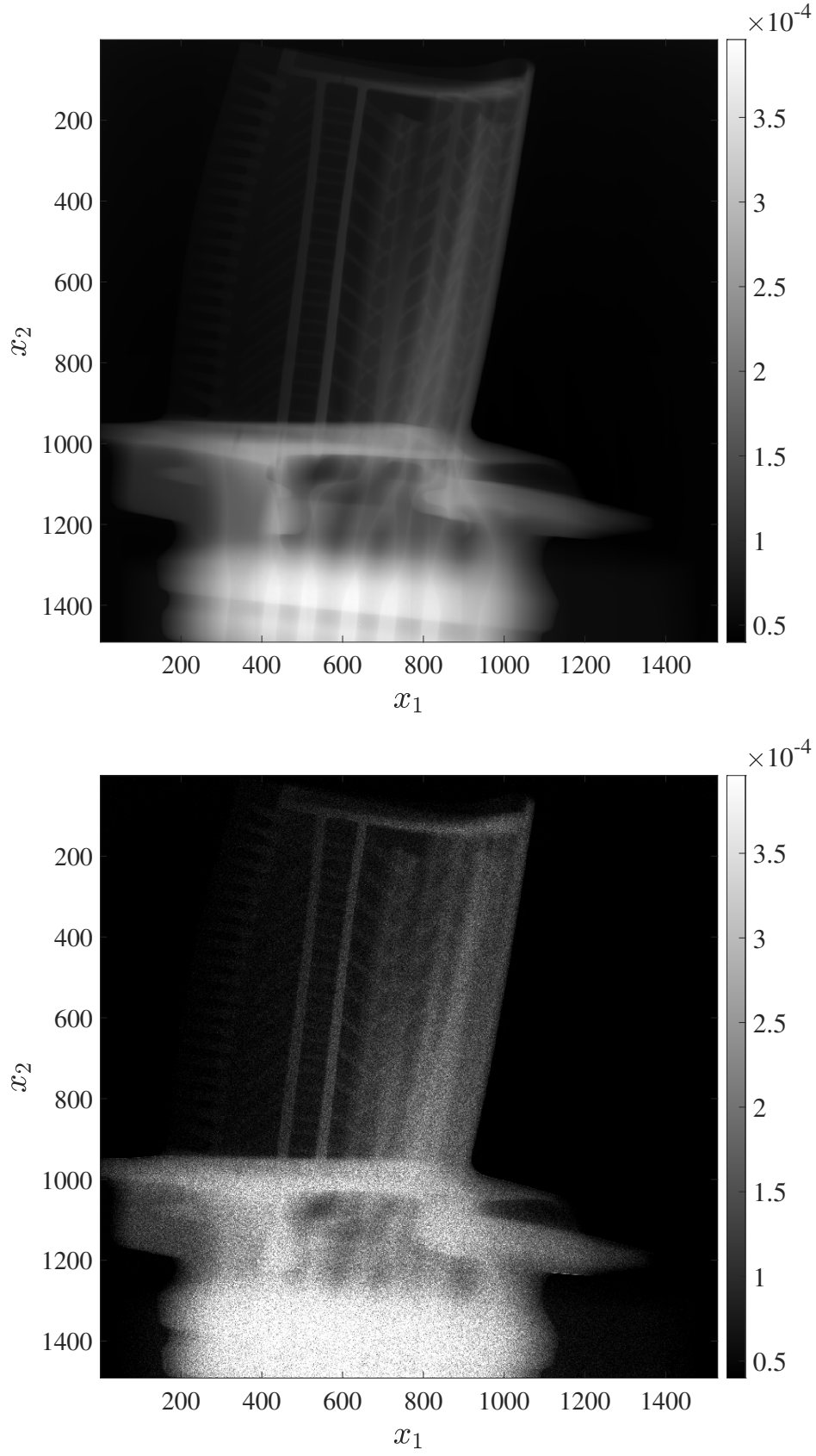

Figure 2.17: Comparison between (a) the theoretically expected noise variance $V_{\text{th}}(\boldsymbol{x})$ and (b) the experimental one $V(\boldsymbol{x})$.

2.3.2 Normality

In Figure 2.18, the probability density function of a zero-mean gaussian distribution is fitted to the probability density function of the noise, given by the values of $g_n(\boldsymbol{x})$. It suggests that the statistical distribution of $g_n(\boldsymbol{x})$ is a Gaussian one. This is confirmed by calculating the skewness and kurtosis for each image $g_n(\boldsymbol{x})$, as shown in Table 2.4.

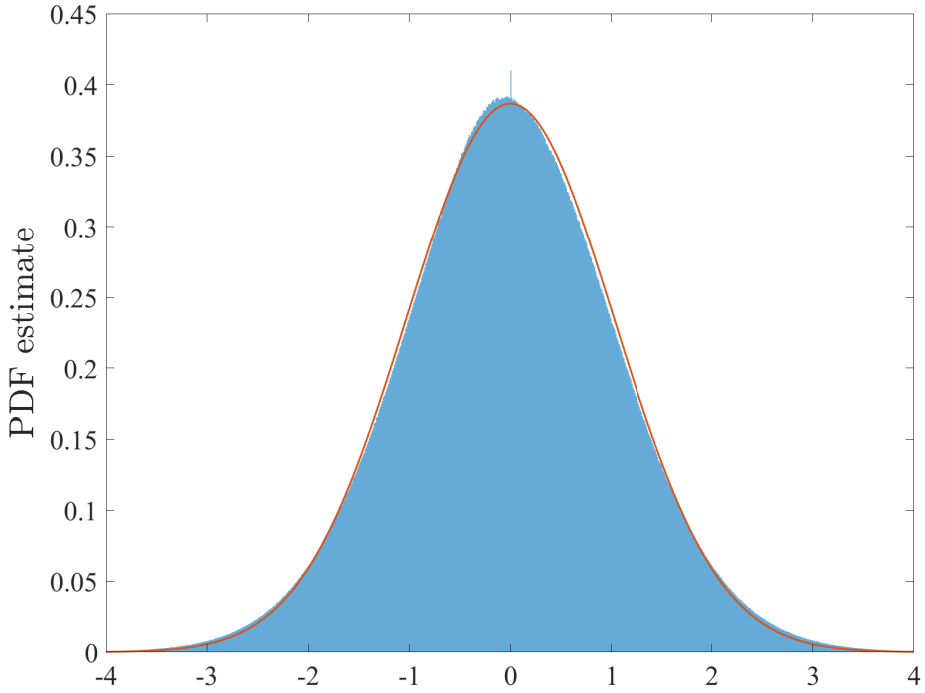

Figure 2.18: Statistical Distribution of $g_n(\boldsymbol{x})$.

	Average value
Skewness	0.02
Kurtosis	3.32

Table 2.4: Average value of skewness and kurtosis of $g_n(\boldsymbol{x})$ (values rounded to two decimal places).

2.3.3 White noise

The autocorrelation functions

$$\Gamma_n(\boldsymbol{u}) = \frac{1}{N_{\boldsymbol{x}}} \sum_{\boldsymbol{x'}} \left[g_n(\boldsymbol{x'}) - \langle g_n \rangle_{\boldsymbol{x}}\right] \left[g_n(\boldsymbol{x'} - \boldsymbol{u}) - \langle g_n \rangle_{\boldsymbol{x}}\right] \tag{2.31}$$

are used to determine whether the noise is white. An example of such a function is displayed in Figure 2.19. The image shows a peak at the origin $\boldsymbol{u} = (0, 0)$. It should be noted that the non-zero values observed in the pixels adjacent to the origin are higher than those in the autocorrelation function Γ_n. These values are still considered negligible (< 0.4), such that the noise polluting $-\ln(I/I_0)$ is regarded as white.

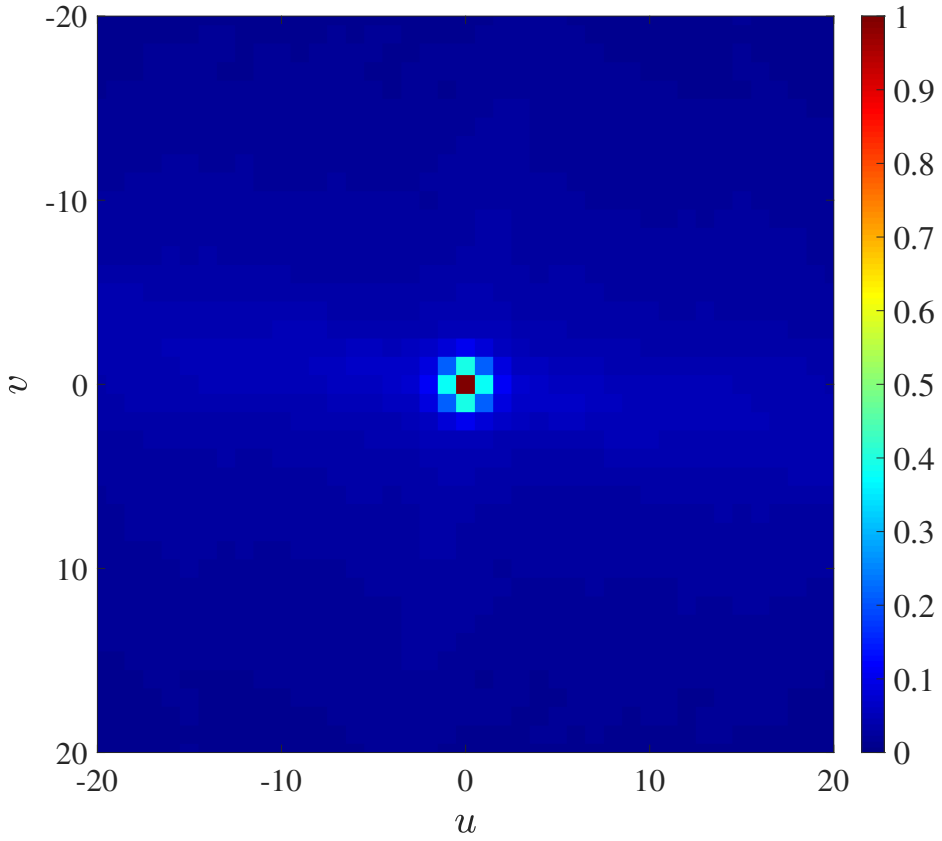

Figure 2.19: $\Gamma_n(\boldsymbol{u})$ for $n = 1$.

2.4 Conclusion

In this section, we built a sparse yet representative description of a flat-field image. This description first rests on the space-time decomposition of the flat-field images. Then, patterns observed in the spatial mode are studied and explained by the incorporation of the characteristic acquisition features, namely the X-ray source (with a cone-beam geometry) and the detector (panel assembly).

Using this description, the noise polluting a flat field image may be extracted by computing the fitting residual. The properties of this noise were investigated and was found to be white, Gaussian, with a (weakly pixelwise-dependent) variance proportional to the measured beam intensity.

The noise affecting a radiographic image was deduced, and its properties predicted. These predictions were experimentally validated. In the end, it was established that this noise is white, Gaussian, with a variance given by the formula (2.27). These properties are used in the rest of this dissertation, as they provide a way to formulate optimization problems designed to minimize acquisition noise error.

Bibliography

[1] Anindya Chatterjee. An introduction to the proper orthogonal decomposition. *Current science*, 78(7):808–817, 2000.

[2] Svante Wold, Kim Esbensen, and Paul Geladi. Principal component analysis. *Chemometrics and Intelligent Laboratory Systems*, 2(1):37–52, 1987.

[3] Gene H. Golub and Charles F. Van Loan. *Matrix computations*. JHU press, 2013.

[4] Kari Karhunen. *Zur spektraltheorie stochastischer prozesse*. Annales Academiae scientiarum Fennicae. Series A. 1, Mathematica-physica. 1946.

[5] Richard Everson and Lawrence Sirovich. Karhunen–Loeve procedure for gappy data. *Journal of the Optical Society of America A*, 12(8):1657–1664, 1995.

[6] Karen Willcox. Unsteady flow sensing and estimation via the gappy proper orthogonal decomposition. *Computers & fluids*, 35(2):208–226, 2006.

[7] Nathan E. Murray and Lawrence S. Ukeiley. An application of Gappy POD. *Experiments in Fluids*, 42(1):79–91, 2007.

[8] Pankaj Saini, Christoph M. Arndt, and Adam M. Steinberg. Development and evaluation of gappy-POD as a data reconstruction technique for noisy PIV measurements in gas turbine combustors. *Experiments in Fluids*, 57(7):1–15, 2016.

[9] Clément Jailin and Stéphane Roux. Modal decomposition from partial measurements. *Comptes Rendus Mécanique*, 347(11):863–872, 2019.

Chapter 3

Definition of the projective model

Contents

Reproduced from

Cédric Fragnaud, Clément Remacha, Julián Betancur, and Stéphane Roux. CAD-based X-ray CT calibration and error compensation. *Measurement Science and Technology*, 33(6):065024, 2022.

Artifacts due to imperfect determination of the scanner geometry, beam hardening (BH), and diffuse Compton scattering, limit the quantitative exploitation of radiographs or tomographies for Non-Destructive Evaluation. Exploiting the Computer-Aided Design (CAD) model of an industrial part, a methodology is proposed to refine the estimation of the Computed Tomography (CT)-scanner geometry up to a scale factor, to correct or account for artifacts, and to assess the metrology of the part. A projective model describing the formation of X-ray images in CT-scanners is first introduced. The optimal parameters of the projective model are identified using a novel CAD-based calibration method that relies on the registration of simulated projections onto experimental ones. A metrological analysis based on the comparison between acquired and simulated X-ray images is proposed. A turbine blade, for which an automatic inspection procedure from few views is under development, is used as an example to illustrate the proposed methodology. The parametrization accounts for the refinement of the projection geometry, the calibration of BH, and the estimation of scattering. It is shown that, using the proposed procedure, the differences between acquired and simulated radiographic images are significantly reduced, indicating that the optimal parameters are properly identified. These differences are then exploited to detect indications in the part.

3.1 Introduction

After outstanding developments in medical applications [1, 2], X-ray Computed Tomography (CT) is rapidly being adopted for Non-Destructive Evaluation (NDE) in industry [3, 4]. X-ray CT enables the verification of the integrity of industrial parts by, for instance, detecting porosities and cracks [5], verifying weaving patterns in 3D woven composites [6], and by performing dimensional metrology [3]. In particular, the detection of geometrical imperfections of turbine blades is of great importance in aeronautics to ensure the safety of passengers. Trained operators perform metrological analyses of turbine blades using radiographic imaging, usually either by examining a CT volume computed by a reconstruction algorithm [7, 8], or through the meticulous inspection of the images when insufficient projections are available. In this chapter, an alternative approach is proposed: the comparison of projections acquired with a CT-scanner to projections simulated from the reference volume representing the ideal part, *i.e.* one without defects, allows the detection of geometrical imperfections of the inspected part.

Estimating accurate geometrical measurements is essential for an exhaustive detection of dimensional flaws. In these metrological applications, artifacts and time are limiting factors, especially in production where few projections are available.

Artifacts result from the deviation between the physical phenomena responsible for the formation of the image and the model used to describe it during the metrological analysis [9]. Indeed, the model is usually simplified as a geometrical projective model and with recourse to Beer–Lambert's law to account for X-ray attenuation. Tomographic reconstruction methods or the raw analysis of X-ray images require an accurate determination of the projection geometry (*e.g.* source-to-object distance (SOD), projection angles). An inaccurate geometry definition undermines the quality of the reconstruction, *e.g.* generating blur artifacts, and the metrological analysis, *e.g.* from magnification effects. Tomographic reconstructions often rely on the strict application of Beer-Lambert's law, which is not perfectly obeyed in CT-scanners used for NDE. In this work, two main sources of errors that deteriorate X-ray image quality or fidelity are considered: beam hardening (BH) [10, 11] and Compton scattering [12, 13].

The other limiting factor is time, which can be reduced but at the cost of increased noise. When using very noisy images, distinguishing noise from artifact-induced systematic deviations between measured and computed radiographs becomes increasingly difficult. Thus, a proper usage of fast scans calls for a very accurate determination of all artifacts.

Various techniques have been developed to mitigate X-ray CT artifacts.

- Projection geometry is usually determined via the study of the projections representing a calibration object whose geometry is known with a great accuracy [14, 15]. It can be further refined in software products when applying reconstruction algorithms to account for rotation axis offset. However, these steps may be insufficient to provide an accurate description of the tomograph set-up.

- The calibration of BH consists of acquiring radiographs of a known reference part and fitting a parametric function to the point cloud of pixelwise detector attenuation versus traversed thickness by the least-squares method [10, 16]. This

method produces satisfactory results but only a few parameters can be safely determined for the attenuation function.

- Signal processing techniques have been used to estimate scattered X-ray beams, *e.g.* by modeling the effect of scattered rays in pixel intensities as the convolution of the primary signal with a kernel to be identified [17, 18]. Deconvolution algorithms have also been proposed to obtain scatter-free projections [19, 20], but the numerical stability of such algorithms is poor [21, 22], leading to unreliable results.

This chapter proposes a CAD-based calibration method to estimate and correct projection geometry parameters, up to a scale factor, and artifacts in a unique formalism. It uses only the projection images of the inspected object and its numerical model (*e.g.* CAD model), *i.e.* it does not require additional projection data, phantom object, or landmarks. The use of prior knowledge of the object shape and material yields an improvement in the quality of the estimation and the correction. Section 3.2 details the challenges addressed in this chapter, namely the correction of the projection geometry, the calibration of BH, and the estimation of scattering. Projection geometry parameters include the source-to-detector distance, the rotation axis, and the orientation of the imaged object. For BH, a parametric representation of the absorption length curve is used, which reduces the absorption calibration to the estimation of few parameters. Likewise, scattering is approximated by a convolution of the geometrical projection by a scattering kernel which is itself parametrized. In these three cases, it is proposed to formulate the problem as a parametric model, and fine-tune those parameters so as to match observations. A description of the proposed methodology used to identify the optimal parameters for the model is given in Section 3.3. Section 3.4 is devoted to the presentation of an example on which the CAD-based calibration procedure has been applied. It consists of the identification of the optimal parameters based on a reduced number of radiographic images of a turbine blade. The results are presented and discussed in Section 3.5.

3.2 Problems addressed

The intensity $I(\boldsymbol{x})$ measured at detector position $\boldsymbol{x} \in \boldsymbol{\Omega} \subseteq \mathbb{R}^2$ is defined as the intensity of the incident X-ray beam attenuated along its path through the sample. The image $I_0(\boldsymbol{x})$ obtained when no sample lies between the source and the detector is called the flat-field image.

The attenuation image P, also called the projection, is derived from the intensity image I and the flat-field image I_0: $P = -\ln(I/I_0)$. Beer-Lambert's law states that $P(\boldsymbol{x})$ is equal to the line integral of the material absorption coefficient along the line joining the source to the detector position $\boldsymbol{x}$. This relation is the main assumption used in all tomographic applications as it relates the measured data to the object geometry and composition. It is an excellent approximation for monochromatic and incoherent X-ray sources. However, scanner sources typically have a broad spectrum of energy, and hence Beer-Lambert's law is usually no more than an approximation.

The projection images are processed via reconstruction algorithms, image processing methods, or simulation of X-ray images, to get a better vision of the inspected

part. Therefore, for CT, numerical tools are of fundamental importance. The simulation of radiographic images is an easy linear problem, but it makes use of an enormous amount of data. It is essential that such computations be very fast. One has the choice of commercial products or open-source tools. Commercial tools implement methods to simulate projections, taking into account multiple artifacts with elaborated physics-based models, however, they are not well fitted to inverse problem analyses which is the purpose of reconstruction and of quantitative NDE. Open-source tools with high numerical efficiency, including GPU optimized codes (such as GPU-accelerated operations, optimized algorithms), are available [23], but are based on the unmodified Beer-Lambert's law. Such powerful open-source tools can still be used efficiently for optimizing image reconstructions if an accurate description of the formation of the images is established.

3.2.1 Projection geometry

The information on the projection geometry is usually determined before or after a tomographic acquisition, often using a calibration object with a well-known geometry and which is easily readable from its projection [14, 24]. This step aims to deliver the geometrical description of the X-ray tomograph scanner captured in a set of parameters, *e.g.* position of the source, axis of rotation (position and orientation), detector (position and orientation). However, these geometrical parameters may be inexact. The fine tuning of these parameters may be proposed to operators by the commercial reconstruction software based on a subjective assessment of the reconstruction quality which is useful because an inaccurate geometry description may compromise a proper reconstruction in particular for metrology assessment [25].

3.2.2 Beam Hardening

In CT systems, X-ray beams are polychromatic and the attenuation coefficient varies with photon energy, thus the simple Beer–Lambert attenuation law does not describe the absorption phenomenon well. Specifically, the distribution of X-ray energies changes with the traveled distance in the material, and consequently the effective (*i.e.* integrating over all X-ray energies) absorption is no longer a material property. This phenomenon, known as beam hardening (BH), implies for a monomaterial, a nonlinear relationship between the gray level of an attenuation image and the thickness of the part the beam passed through. Should Beer–Lambert's law still be used in the polychromatic case, a deviation between the model and the actual measurements would be observed. This would lead to a misinterpretation of the grayscale values where thicknesses get underestimated, yielding overestimated attenuation coefficients, which in turn deteriorates the quality of the reconstructed volume in the form of streaks and flares, known as BH artifacts [11].

In the case of monomaterial parts, these artifacts can be corrected through the calibration of the attenuation. It consists in identifying the relationship between the gray level $P(\boldsymbol{x})$ of the measured attenuation image and the thickness $T(\boldsymbol{x})$ of material the X-ray beam has gone through before hitting the pixel detector at $\boldsymbol{x}$. T is called a thickness map. It thus reduces to a non-linear gray level re-encoding represented by a function $U : \mathbb{R}^+ \mapsto \mathbb{R}^+$ such that $U(T(\boldsymbol{x})) = P(\boldsymbol{x})$, see Figure 3.1. A mere gray level re-encoding with U^{-1} allows an attenuation image P to be transformed into

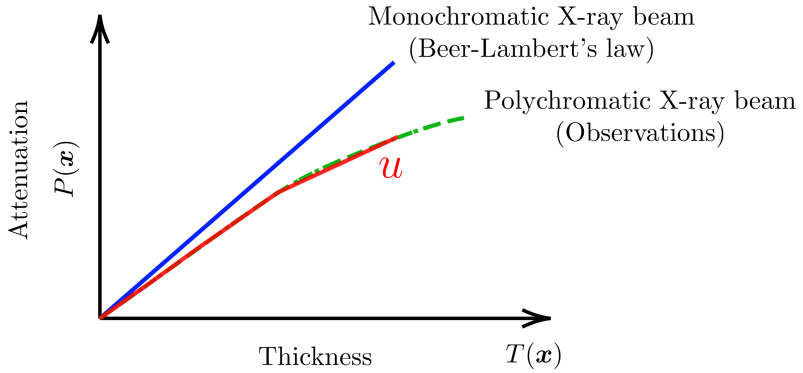

Figure 3.1: Differences between monochromatic assumptions (blue line), and polychromatic measurements (green dashed line). The aim is to determine the relationship between the two curves through the fit of a parametric function u (red line) to observations.

a thickness map T, hence enabling a legitimate use of Beer–Lambert's law even for polychromatic sources. The aim of BH correction is to determine the function u that best approximates U. Because it depends on the source technology and settings, u cannot be precomputed and is instead inferred from observations. The parameters of the correction function are usually identified by acquiring projections of a known reference part, then fitting the function to the point cloud — pixelwise detector attenuation versus thickness — by the least-squares method [10, 16]. This fit is performed via the minimization of the error between observation and estimation, on a pixel-per-pixel basis. Such an approach does not allow for many parameters to describe the attenuation. Usually, odd-order polynomials are chosen to keep the correction function monotonous, and a maximum polynomial order may be typically 5, leaving two unknown parameters [26, 27] since the linear term may be conventionally set to a unit prefactor. The proposed CAD-based calibration procedure permits many more degrees of freedom to be chosen while avoiding regression stability issues.

The function u is discretized over a basis of shape functions ϕ_k,

$$u(\xi) = \sum_{k=1}^{K} c_k \, \phi_k(\xi) \tag{3.1}$$

where c_k are parameters to be determined, and ξ is a dummy variable representing the thickness of material. u being defined up to an arbitrary scale factor, a convention is used to lift this degeneracy, for instance by imposing $\frac{\mathrm{d}u}{\mathrm{d}\xi} = 1$ for $\xi \sim 0$. A desirable property for ϕ_k is that the addition or removal of one of these functions has only a local effect on the function u. This amounts to saying that, for a given k, ϕ_k acts on a restricted range of values for ξ, *i.e.* ϕ_k has a compact support.

In this work, a piecewise-linear function for u is used. Besides its simplicity, it has the advantage of being a good interpolant of U with the property that the more parameters, the better the interpolation, without loss of stability. Considering a discretization $\xi_0, \xi_1, \ldots, \xi_{K+1}$ of the gray levels of the thickness map, ϕ_k is the triangular

function, compactly supported, defined by

$$\phi_k(\xi) = \begin{cases} \frac{\xi - \xi_{k-1}}{\xi_k - \xi_{k-1}} & \text{if } \xi_{k-1} \leq \xi < \xi_k \\ \frac{\xi_{k+1} - \xi}{\xi_{k+1} - \xi_k} & \text{if } \xi_k \leq \xi < \xi_{k+1} \\ 0 & \text{otherwise} \end{cases} \tag{3.2}$$

Once the function u described by (3.1) and (3.2) is identified, it can be applied to each pixel of the simulated projections. The relevance of this choice of model may be appreciated by studying the differences between acquired and simulated projections with the BH correction.

An optimal discretization must meet two conditions:

1. The discretization must properly reflect the curvature of the BH calibration function: the resolution of the mesh must be higher in zones of high curvature than in zones of low curvature.
2. The number of points observations covered by the shape function ϕ_k has to be large enough to estimate the corresponding parameter c_k.

To perform an ideal discretization satisfying condition 2., it is suggested to carry out a sampling via an arithmetic sequence on the cumulative frequency of the gray levels of T. This produces a sequence $\xi_0, \xi_1, \ldots, \xi_K$. The last shape function is extended to infinity assuming a constant value so that the model can cope with the highest material thicknesses: $\xi_{K+1} = +\text{“}\infty\text{”}$ (in practice, a sufficiently high value, *e.g.* maximum thickness, is chosen). This discretization can be further refined so that condition 1. is verified, potentially at the expense of increasing the number of interpolation shape functions and thus the number of parameters.

3.2.3 Compton scattering

In a radiographic image, over-intensities are observed in regions away from the part where the absorption of X-rays is null or negligible. They originate from X-rays scattered away by the sample due to, *inter alia*, the Compton effect (Figure 3.2).

The measured intensity at pixel $\boldsymbol{x}$ is described as the sum of two components: a primary one $I_P(\boldsymbol{x})$, derived from photons passing directly through the object without scattering or absorption, and a secondary contribution $I_S(\boldsymbol{x})$, that corresponds to photons scattered away from the initial trajectory by the Compton effect. Although scattering leads to complications in the analysis of radiographic images, it has a very minor effect in most applications of materials science where energies are large (in contrast to medical applications). Hence scattering is treated as a small perturbation and multiple scattering is neglected in front of single scattering (*cf.* Section 1.3.2.3). Usually, CT reconstruction does not account for scatter, leading to artifacts in the reconstructed volume such as streaking or cupping [11, 13]. It may also cause a deviation of dimensional measurements from their actual values because of the difficulty to localize edges precisely.

Methods using signal processing techniques have been developed to estimate and correct for scattering effects. The scattered X-ray distribution can be predicted via Monte-Carlo (MC) simulations [28, 29]. Although it is a powerful tool, the poor convergence properties of MC sampling leads to time-consuming calculations. Point-Spread Functions (PSFs) have been used to describe single scattering of the pencil

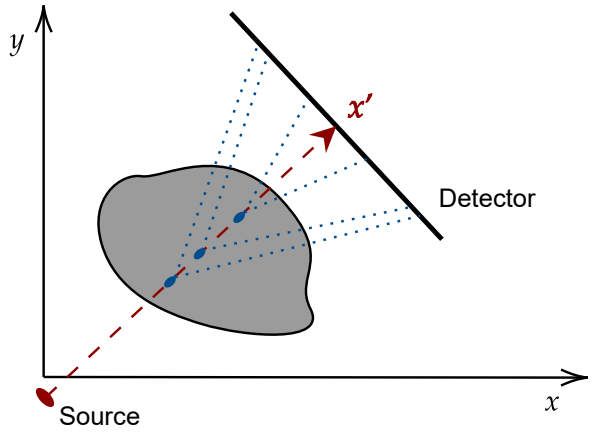

Figure 3.2: Illustration of the Compton effect. A beam emerging from the source interacts along its path with the atoms of the object: X-ray photons are scattered away from their initial trajectory, leading to an additional signal captured by the elements of the detector around $\boldsymbol{x'}$.

beam [30, 31, 32, 33]. PSFs are represented as the convolution between the incident photon flux and a kernel to be determined.

The above modeling is 3D and thus costly and difficult to couple to tomographic reconstruction. Following [18, 19, 20], it is proposed to resort to an approximation that captures a large part of the scattering. The approximation formulas are derived from an expression of the scattered intensity based on the interactions a beam undergoes as it propagates through the object [34]. The intensity $I_S(\boldsymbol{x})$ received at a pixel $\boldsymbol{x}$ from all the scattered rays is expressed as

$$I_S(\boldsymbol{x}) = \int_{\boldsymbol{x'}} T(\boldsymbol{x'})\, I_0(\boldsymbol{x'})\, e^{-T(\boldsymbol{x'})/\xi_a}\, G(\boldsymbol{x'} - \boldsymbol{x})\, \mathrm{d}\boldsymbol{x'} \tag{3.3}$$

where ξ_a is the attenuation length of the radiation, and G is a scatter kernel to be estimated. As long as the scattering occurs in a short range ($\boldsymbol{x'} - \boldsymbol{x}$ small as compared to ξ_a), the gradient of I_0 may be ignored so that $I_0(\boldsymbol{x'})/I_0(\boldsymbol{x}) \approx 1$, and thus

$$I_S(\boldsymbol{x})/I_0(\boldsymbol{x}) = (I_A * G)\,(\boldsymbol{x}) \tag{3.4}$$

with $I_A(\boldsymbol{x}) = T(\boldsymbol{x})\, e^{-T(\boldsymbol{x})/\xi_a}$.

Complementary notes

The expression of the scattered intensity is derived from the interactions a beam undergoes as it propagates through the object. Only single scattering, in which photons experience solely one scatter interaction with the sample, is considered here as it constitutes the prevailing part of the actual secondary signal.

A beam is emitted towards a direction identified by its intersection with the detector at $\boldsymbol{x'}$ and enters the object at a point $\boldsymbol{u_0}$. On its path, it is deflected at a point $\boldsymbol{u}$, exits the object at $\boldsymbol{u_1}$ before reaching the detector at $\boldsymbol{x}$ with an

intensity equal to

$$J(\boldsymbol{x'}, \boldsymbol{u}, \boldsymbol{x}) = I_0(\boldsymbol{x'})\, e^{-\|\boldsymbol{u}-\boldsymbol{u_0}\|/\xi_a}\, e^{-\|\boldsymbol{u_1}-\boldsymbol{u}\|/\xi_a}\, \phi(\boldsymbol{x'}, \boldsymbol{u}, \boldsymbol{x}) \tag{3.5}$$

where ξ_a is the attenuation length of the radiation, and $\phi(\boldsymbol{x'}, \boldsymbol{u}, \boldsymbol{x})$ represents the probability for the beam to be deflected towards the pixel $\boldsymbol{x}$. It is worth insisting that the object is assumed to be monomaterial, which translates into a single ξ_a in eq. 3.5. The intensity $I_S(\boldsymbol{x})$ received at $\boldsymbol{x}$ from all the scattered rays is given by integrating (3.5) over all possible $\boldsymbol{x'}$ and $\boldsymbol{u}$. The idea proposed here is to condense the 3D volume onto a single plane, namely the median plane between the source and the detector. Considering that the entire scatter signal is concentrated on it, one has $\phi(\boldsymbol{x'}, \boldsymbol{u}, \boldsymbol{x}) = \phi(\boldsymbol{x'}, \boldsymbol{x})$, leading to

$$I_S(\boldsymbol{x}) = \int_{\boldsymbol{x'}} I_0(\boldsymbol{x'})\, \phi(\boldsymbol{x'}, \boldsymbol{x}) \int_{\boldsymbol{u}} e^{-(\|\boldsymbol{u}-\boldsymbol{u_0}\|+\|\boldsymbol{u_1}-\boldsymbol{u}\|)/\xi_a}\, \mathrm{d}\boldsymbol{x'}\, \mathrm{d}\boldsymbol{u} \tag{3.6}$$

Provided the scattering angle is low and assuming the normal to the detector is close to the vector pointing towards the source, ϕ is a function of $\boldsymbol{x'} - \boldsymbol{x}$, *i.e.* $\phi(\boldsymbol{x'}, \boldsymbol{x}) = G(\boldsymbol{x'} - \boldsymbol{x})$, and $\|\boldsymbol{u} - \boldsymbol{u_0}\| + \|\boldsymbol{u_1} - \boldsymbol{u}\| \approx T(\boldsymbol{x'})$, which yields

$$I_S(\boldsymbol{x}) = \int_{\boldsymbol{x'}} I_0(\boldsymbol{x'})\, T(\boldsymbol{x'})\, e^{-T(\boldsymbol{x'})/\xi_a}\, G(\boldsymbol{x'} - \boldsymbol{x})\, \mathrm{d}\boldsymbol{x'} \tag{3.7}$$

that corresponds to the expression in (3.3).

The kernel G is parametrized as the weighted sum of basic kernels k_σ,

$$G(\boldsymbol{x}) = \sum_{\sigma \in \Sigma} a_\sigma\, k_\sigma(\boldsymbol{x}) \tag{3.8}$$

with $\Sigma \subset \mathbb{R}^+$. Coefficients a_σ need to be adjusted to the best fit of the observations. This parametrization is expected to account for the effective scatter distribution with a reasonable number of parameters. The contribution of Compton scattering suggests that the kernel is bell-shaped and symmetric. A superposition of Gaussian functions can be chosen to describe it, so that the kernels k_σ are modeled as

$$k_\sigma(\boldsymbol{x}) = g_\sigma(\boldsymbol{x}) - \frac{\delta(\boldsymbol{x})}{2\pi\sigma^2} \tag{3.9}$$

where g_σ is the 2D-Gaussian kernel with standard deviation σ. The introduction of the Dirac function δ is based on the observation that photons that were supposed to reach the detector at pixel $\boldsymbol{x}$, but that have been deflected, reach the detector at another pixel. Hence, its contribution is removed from the measured signal. This part of the kernel is merely equivalent to increasing the absorption in proportion to the crossed thickness $T(\boldsymbol{x})$, as if the coefficient of absorption of the material were slightly increased by the total amount of scattering. Note that the beam may also be scattered away from the detector, and here again contributes to an additional attenuation. In the end, provided that an adjustment of the attenuation coefficient is considered (as for BH correction), δ in (3.9) may be omitted.

In order to account for the scattered photons that reach the detector over a wide range of distances from pixel $\boldsymbol{x}$, the set $\Sigma = \left\{2^k, k \in \mathcal{L} \subset \mathbb{R}^+\right\}$ is suggested. This geometric progression is introduced to limit the overlap of Gaussian kernels g_σ which would render the determination of the kernel ill-conditioned.

Once the kernel G is identified, the correction of the images produced by the system via deconvolution techniques should be avoided because it is known to be an ill-behaved problem generating spurious high frequency signals [21]. Instead, an alternative method consists in computing the scatter signal by numerically simulating the radiographic images and by convolving them with the kernel G. The subtraction of this signal from the acquired images is expected to produce close to scatter-free radiographic images provided they are properly registered.

The correction of the above artifacts as well as the determination of the precise geometry of the tomograph finally reduce to a single problem: the identification of the optimal parameters needed to produce an accurate synthetic radiographic image from a known object geometry.

3.3 Calibration of parameters

A calibration procedure, based on sensitivity fields, is proposed to identify optimal parameters for the model describing the formation of images in X-ray CT-scanners. This model is defined by the projection geometry parameters $\boldsymbol{p} = (p_k)$, the coefficients $\boldsymbol{c} = (c_k)$ of the BH calibration function (3.1), and the amplitudes $\boldsymbol{a} = (a_\sigma)$ of the scattering kernel (3.9).

Suppose the K parameters d_k, gathered in a vector $\boldsymbol{d} = (d_k)$, are to be identified. Let $P_{\mathrm{a}}^n(\boldsymbol{x})$, $n \leq N$, be the N projections acquired with a CT-scanner, regarded as reference images. Given an initial estimate $\boldsymbol{d^0}$ and a reference volume of the inspected part, projections $P_{\mathrm{s}}^n(\boldsymbol{x}; \boldsymbol{d^0})$ are numerically simulated. The reference volume representing the ideal design can have several formats including a CAD model described by analytical functions or by a polygon mesh, or a tomographic volume. The sensitivity fields

$$s_k^n(\boldsymbol{x}) = \left.\frac{\partial P_{\mathrm{s}}^n(\boldsymbol{x}; \boldsymbol{d})}{\partial d_k}\right|_{\boldsymbol{d}=\boldsymbol{d^0}} \tag{3.10}$$

are then computed. The partial derivatives involved in the calculation of these fields may be approximated by finite differences

$$s_k^n(\boldsymbol{x}) = \frac{P_{\mathrm{s}}^n\left(\boldsymbol{x}; \boldsymbol{d^0} + h\,\boldsymbol{e}_k\right) - P_{\mathrm{s}}^n\left(\boldsymbol{x}; \boldsymbol{d^0}\right)}{h} \tag{3.11}$$

where $\boldsymbol{e}_k$ refers to the k^{th} vector of the canonical basis of the space of parameters, *i.e.* $(\boldsymbol{e}_k)_i = \delta_{ki}$. These sensitivity fields quantify how small perturbations around the value $\boldsymbol{d^0}$ affect the simulated projections $P_{\mathrm{s}}^n(\boldsymbol{x})$ for each parameter d_k.

Projection residuals $\rho_{\boldsymbol{d^0}}^n(\boldsymbol{x}) = P_{\mathrm{a}}^n(\boldsymbol{x}) - P_{\mathrm{s}}^n(\boldsymbol{x}; \boldsymbol{d^0})$, *i.e.* the differences between X-ray acquisitions and simulated projections, are interpreted as resulting from the misidentification of the parameters. In order to quantify the discrepancy between estimated and optimal parameters, these residuals are projected in the least-squares sense onto

the sensitivity vectors,

$$\boldsymbol{\delta d}^* = \arg\min_{\boldsymbol{\delta d}} \sum_{n=1}^{N} \|\rho^n_{\boldsymbol{d^0}}(\boldsymbol{x}) - \boldsymbol{s^n}(\boldsymbol{x})\ \boldsymbol{\delta d}\|_2^2 \tag{3.12}$$

where the notation $\boldsymbol{s^n}(\boldsymbol{x}) = \begin{pmatrix} s^n_1(\boldsymbol{x}) & \dots & s^n_K(\boldsymbol{x}) \end{pmatrix}$ is used, and $\boldsymbol{\delta d}$ is the column vector containing the variables of the minimization problem. The use of the L_2-norm can be justified as being optimal when the images $P^n_a(\boldsymbol{x})$ are polluted by white Gaussian noise: the maximum of the log-likelihood corresponds to the minimum of the L_2-norm. Equation 3.12 can be seen as minimizing a function that is a linearized version (using a Gauss-Newton scheme) of the cost function defined by the L_2-norm of the differences between the acquired images $P^n_{\mathrm{a}}(\boldsymbol{x})$ and the simulated images $P^n_{\mathrm{s}}(\boldsymbol{x};\boldsymbol{d})$, as described in Section 4.2.2. Assuming a Poisson noise on $I(\boldsymbol{x})$ and $I_0(\boldsymbol{x})$, a change in the expression of equation (3.12) into a weighted sum may be used to take into account the local uncertainty. $\boldsymbol{\delta d}^*$ represents the error made in the identification of the parameters and thus provides the amount by which the parameters $\boldsymbol{d^0}$ are to be changed to reduce the discrepancy between $P^n_{\mathrm{a}}(\boldsymbol{x})$ and $P^n_{\mathrm{s}}(\boldsymbol{x};\boldsymbol{d^0})$. This value is given by

$$\boldsymbol{\delta d}^* = \boldsymbol{H}^{-1}\boldsymbol{b} \tag{3.13}$$

where the matrix $\boldsymbol{H}$ is defined by

$$H_{ij} = \sum_n \sum_{\boldsymbol{x}} s^n_i(\boldsymbol{x})\, s^n_j(\boldsymbol{x})\, w^n(\boldsymbol{x}) \tag{3.14}$$

and $\boldsymbol{b}$ is the vector whose components b_k are given by

$$b_k = \sum_n \sum_{\boldsymbol{x}} s^n_k(\boldsymbol{x})\, \rho^n_{\boldsymbol{d^0}}(\boldsymbol{x})\, w^n(\boldsymbol{x}) \tag{3.15}$$

with $w^n(\boldsymbol{x})$ the reciprocal of the variance of the noise polluting $P^n_a(\boldsymbol{x})$. Note that $\boldsymbol{H}$ represents the matrix of the second derivatives of the cost function (3.12) with respect to $\boldsymbol{\delta d}$, assuming the sensitivity fields $s^n_k(\boldsymbol{x})$ do not depend on $\boldsymbol{\delta d}$, and is thus referred to as the Hessian matrix.

Repeating this CAD-based calibration procedure usually leads to a fixed point solution (one that no longer evolves) after few iterations. Although there is no guarantee to obtain a unique solution, the proposed parametrization together with the use of a complex shape CAD model (with high and low frequency power) and a good initialization make the problem well behaved.

It is important to emphasize that if the observed object differs from its model by a mere homothety, the projection geometry parameters can be adjusted to inexact values and yet produce a perfect match of the projections. Assuming the analyzed object has a complex shape, this scale factor is the only degeneracy of the geometrical calibration. It can only be lifted if one additional length measurement is performed and used jointly in the calibration process.

It should be noted that the very same procedure holds for any set or subset of parameters. Because of non-linearities, the order in which subsets may be considered is important. An appropriate rule is to rank the impact of the projection geometry, BH and Compton scattering, and fit corresponding parameters in descending impact order. The impact can be assessed by the observation of the projection residuals computed before any correction, as it is the case here.

3.4 Case study

The inspection of a turbine blade (Figure 3.3) was selected as a case study. This monomaterial part is made of a monocrystalline nickel alloy.

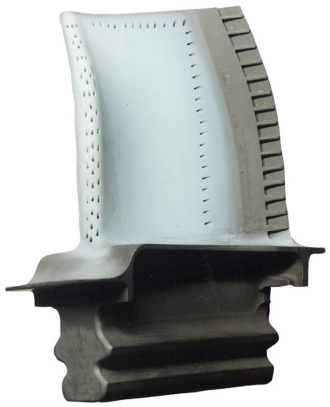

Figure 3.3: View of a turbine blade. Reproduced with permission from [35].

The reference volume representing the ideal part was the CAD model of the part described by a polygon mesh. To obtain a universal structure — *i.e.* usable by a vast majority of software — describing the 3D volume, it was discretized into voxels whose size were 0.05 mm using a ray tracing algorithm similar to that described in [36]. Each voxel was characterized by a binary numerical value (0 or 1) depending on whether it belongs to air or to metal.

A set of $N = 6$ intensity images representing one turbine blade from complementary points of view were exploited, each image being obtained from the average of two frames with an exposure time of 354 ms each. This is in line with the number of views routinely used for their inspection. The images have been acquired with the XT H 450 system developed by Nikon Metrology, with a high-energy source of 390kV. The tube current was set to 641 μA. The system produced 2000 $\times$ 2000-pixel radiographs, each pixel being encoded as a 16-bit unsigned integer. The associated attenuation images were denoted $P_{\mathrm{a}}^n, n \leq N$.

From the reference volume, attenuation images $P_{\mathrm{s}}^n, n \leq N$, were simulated using the ASTRA Toolbox [23]. The latter proposes projection operators with highly flexible source/detector positioning and GPU-acceleration, and is callable from Matlab and Python. A scale factor for the gray levels of the reference volume has been adjusted (by taking into account the actual attenuation coefficient of the nickel alloy) so that the projection P_{s}^n of the binarized volume matches the true projection P_{a}^n.

The following parameters were used to perform the calibration:

- The projection geometry was controlled by a vector $\boldsymbol{p}$ of 14 parameters: the size of detector pixels, the SOD, the six components of the position of the detector (three translations, one of which with respect to the source via the source-to-detector distance (SDD) and three rotations), and the six components of the position of the studied object (three rotations and three translations). Although the size of detector pixels is supposedly known, a readjustment is permitted, which in practice is very small. The translation and rotation parameters of the detector are used to model the rotation axis offset.

- The BH calibration function u was modeled as a sum of $K = 8$ triangular functions ϕ_k controlled by a K-component vector $\boldsymbol{c}$. In the simulated images, prior to reproducing the BH using the proposed model, the attenuation of the X-ray beam follows Beer-Lambert's law, so that $P_s^n(\boldsymbol{x}) \propto T^n(\boldsymbol{x})$ where T^n denotes the n^{th} thickness map. This relation is based on the assumption that the simulated (uncorrected) images perfectly match the acquired images. Although it may not be actually the case at the beginning of the CAD-based calibration procedure, it becomes more and more valid with each iteration. Hence, the discretization described in Section 3.2.2 was performed, not on the gray levels of the unknown T^n, but on those of the uncorrected P_{s}^n. The last discretization point was set to $\xi_{k+1} = 20$.

- Regarding the scatter kernel used to reproduce the scatter signals and described by a vector $\boldsymbol{a}$ of seven parameters, the Gaussian standard deviations σ are defined by the sequence $\Sigma = \left\{2^k, 2 \leq k \leq 8\right\}$.

The CAD-based calibration procedure was performed using restricted (rectangular) Regions Of Interest (ROIs) of the images. The information on the projection geometry and BH only come from the region containing the projection of the object. On the other hand, the scatter is more observable in regions outside of it (as it is clearly due only to scattering and does not depend on the other parameters such as geometry or BH), more specifically next to regions containing the projection of the thickest part of the object. Based on these elements, two ROIs were considered for each view, as illustrated in Figure 3.4, depending on which parameters were being fine-tuned. If only a subset of images is considered, the procedure is not optimal but is much faster (less data to process), and the benefit of using all data is modest provided the subregions are well chosen.

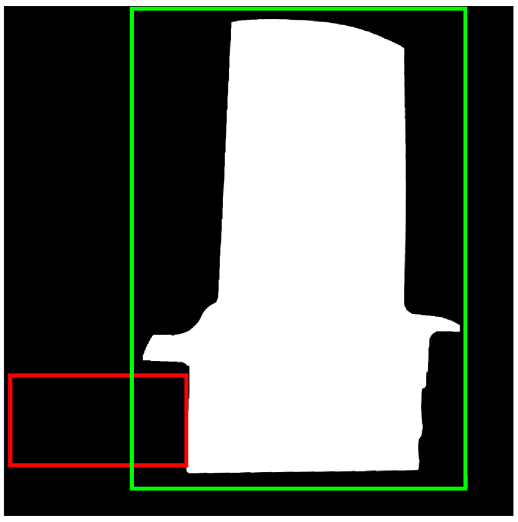

Figure 3.4: Example of the two ROIs for one view. The ROI associated to the calibration of the projection geometry and BH is displayed in green, the one associated to the calibration of scattering is displayed in red.

The calibration of the parameters $\boldsymbol{p}$, $\boldsymbol{c}$ and $\boldsymbol{a}$ was conducted iteratively according to the procedure described in Algorithm 2. A misregistration between observed and simulated images is likely to be confused with small angle scattering, distorting the entire calibration procedure. Hence, the scatter parameters were at first not considered, and were added to the procedure after the parameters $\boldsymbol{p}$ and $\boldsymbol{c}$ first converge. The first and final convergence criteria can be based on a maximum number of iterations, on the computed increments ($\boldsymbol{\delta p}^*$, $\boldsymbol{\delta c}^*$ and $\boldsymbol{\delta a}^*$), or, as used in this work, on the discrepancies between observed and simulated projections after the iteration. The order in which the calibrations were performed was based on the abovementioned principle. Close to the fixed point, one may refine the parameters in any order.

A study has been performed to quantify the noise polluting a projection and thus determine $w^n(\boldsymbol{x})$, *cf.* Chapter 2. It was found that this noise variance is given by $V(\boldsymbol{x}) = \sigma^2 \left(\frac{1}{N(\boldsymbol{x})} + \frac{1}{M(\boldsymbol{x})} \right)$, with $\sigma^2 \approx 1.65 \times 10^{-5}$ (for the CT-scanner and acquisition parameters used), and where $N(\boldsymbol{x})$ and $M(\boldsymbol{x})$ correspond to the noiseless (*i.e.* simulated) intensity image and flat-field image, respectively.

Once the parameters are estimated, the BH and scatter are reproduced on the simulated images, which are then denoted with a star superscript, $P_s^{n,*}$.

Algorithm 2: Iterative calibration procedure

Data: Initial estimations $\boldsymbol{p^0}$, $\boldsymbol{c^0}$, $\boldsymbol{a^0}$
Result: Optimal values $\boldsymbol{p^*}$, $\boldsymbol{c^*}$, $\boldsymbol{a^*}$
do
  Simulate images with the current parameters $\boldsymbol{p}$, $\boldsymbol{c}$ and $\boldsymbol{a}$;
  Compute $\boldsymbol{\delta p}^*$ using (3.13) and update $\boldsymbol{p} \leftarrow \boldsymbol{p} + \boldsymbol{\delta p}^*$;
  Simulate images with the current parameters $\boldsymbol{p}$, $\boldsymbol{c}$ and $\boldsymbol{a}$;
  Compute $\boldsymbol{\delta c}^*$ using(3.13) and update $\boldsymbol{c} \leftarrow \boldsymbol{c} + \boldsymbol{\delta c}^*$;
  if *First convergence criterion reached* **then**
    Simulate images with the current parameters $\boldsymbol{p}$, $\boldsymbol{c}$ and $\boldsymbol{a}$;
    Compute $\boldsymbol{\delta a}^*$ using (3.13) and update $\boldsymbol{a} \leftarrow \boldsymbol{a} + \boldsymbol{\delta a}^*$;
while *Final convergence criterion reached*;

3.5 Results and discussions

The discrepancy between a simulated and acquired intensity image before and after the CAD-based calibration procedures for restricted ROIs of the image is displayed in Figure 3.5. Prior to any adjustment, the differences were mostly due to an incorrect projection geometry, whose correction is illustrated in Figure 3.6. The major change concerns the adjustment of the position and orientation of the volume, and of the position of the detector, see Table 3.1. The second most important factor was the correction of gray levels brought by BH corrections. The reproduction of BH lead to an attenuation of the differences inside the part, thus allowing a better interpretation of the gray level intensities as the thickness of material crossed by the beam. By reproducing scattering, the differences around the part were reduced, resulting in a finer edge definition. Figure 3.5 shows that the misestimation of the projection geometry and the BH phenomena have a greater impact than the scatter (most visible in panels

(c) and (d)). This observation confirms the order chosen in Algorithm 2. Figure 3.7 indicates that a stable solution was reached after only a few iterations. The norms of residuals were reduced on average from 959 to 96, that is by a factor of 10.

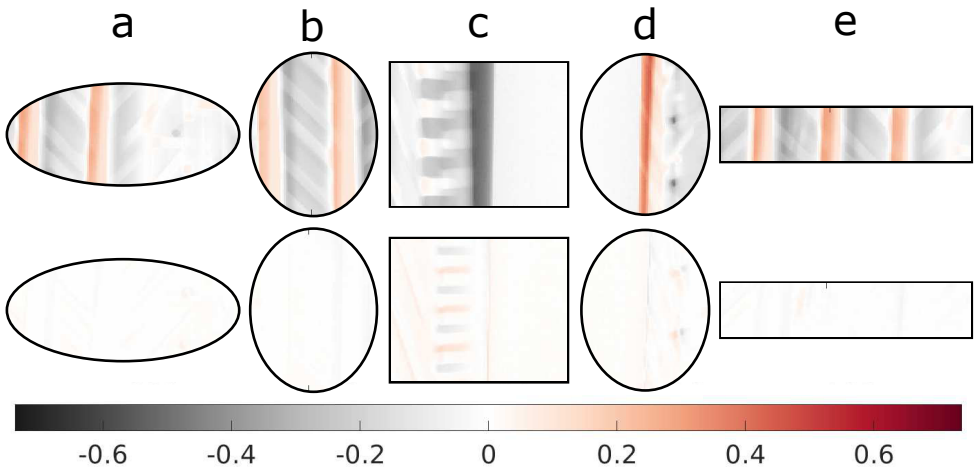

Figure 3.5: Difference (color) between acquired and simulated intensity images, before (top) and after (bottom) identification of the projection geometry and consideration of BH and scatter artifacts. The different panels show: (a) internal air cooling cavities in the airfoil, (b) internal air cooling cavities and internal structure, known as a rib structure, in the airfoil, (c) slots on the trailing edge, (d) cooling holes in the leading edge, (e) internal air cooling cavities and rib structure in the airfoil.

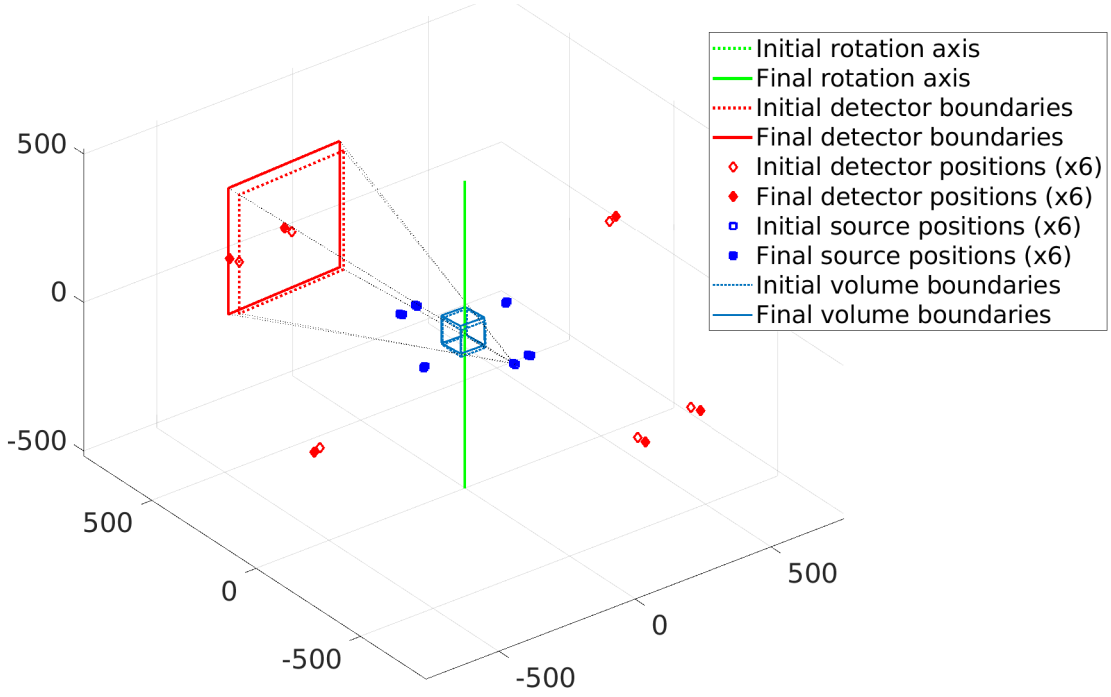

Figure 3.6: Modification of the projection geometry using the proposed CAD-based calibration method for $N = 6$ (distance expressed in mm).

Parameter	Initial estimation	Final estimation	Change
Size of detector pixels (mm)	0.20	0.21	0.01
SOD (mm)	226.43	217.96	-8.47
SDD (mm)	1009.67	1034.67	24.99
Translation vector of the detector (mm)	0.00 0.00	-2.60 13.64	-2.60 13.64
Rotation angles of the detector (deg)	0.00 0.00 0.00	-0.16 -0.18 -0.15	-0.16 -0.18 -0.15
Translation vector of the studied object (mm)	3.14 8.97 0.45	5.99 17.20 4.26	2.85 8.23 3.81
Rotation angles of the studied object (deg)	0.00 0.00 0.00	-3.30 2.07 1.03	-3.30 2.07 1.03

Table 3.1: Change in the projection geometry.

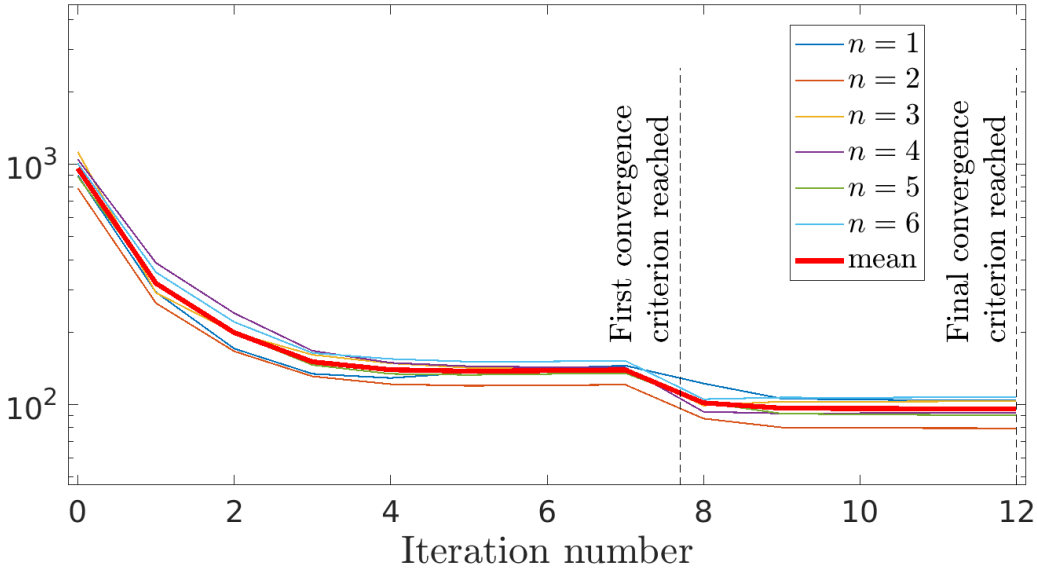

Figure 3.7: Evolution of the L_2-norm of residuals over iterations.

It is assumed that, after the CAD-based calibration procedure, $P_s^{n,*}$ perfectly matches P_a^n, $\forall n$. Let $P_s^{n,+}$ be the simulated attenuation images after the calibration procedure, but for which the BH is left uncorrected. As stated before, the simulation of radiographic images is based on Beer-Lambert's law, so that $P_s^{n,+}(\boldsymbol{x}) \propto T^n(\boldsymbol{x})$. Thus, by generating the point cloud $(P_s^{n,+}, P_a^n)$ one can observe the discrepancy between Beer-Lambert's law and the experimental measurements, see Figure 3.8a. The estimated function u provides a good approximation of the scatter plot of the projection data P_a^n. It is shown that a different discretization, from 4 to 12 parameters (Figure 3.8b), leads to a similar function. By applying u to each pixel of $P_s^{n,+}$, the simulated images $P_s^{n,*}$ were more faithful to reality, as shown by the residuals in Figure 3.5.

This quality of calibration can be explained by the fact that, unlike the usual approaches, the spatial correlations of the projection were exploited. The measured image resulted from the projection of a part on the detector. This part provided information on the expected gray levels given its geometry, position and orientation in space, and chemical composition. The proposed methodology used this knowledge to produce a more stable and accurate calibration of BH.

The estimated scatter kernel G is represented in Figure 3.9. At high energy, the scattering probabilities are rather small, and a photon is mostly scattered in the forward direction. Then, the intensity of the scatter signal is negligible compared to that of the primary signal. These characteristics were observed here as the scatter kernel had a low amplitude and a small radius. In CT, the correction of such a signal is not necessary, but it becomes crucial when individual radiographs are to be quantitatively analyzed.

The final differences, bottom of Figure 3.5, represent the deviation between the ideal part (CAD model) and the inspected part. A small difference in thickness at the trailing edge of the blade (panel c) is observed, and two cooling holes (panel d) are misplaced. These two differences have no consequence on the quality of the produced part, but simply reveals the excellent sensitivity of the analysis after proper calibration. They would not be detectable from the raw data (Figure 3.5, top).

The identified parameters are used to enhance the quality of the tomographic volume. A set of 3000 projections have been acquired using the same CT-scanner and acquisition parameters as previously. The associated tomographic volume is calculated (i) without any gray level correction on the projections and (ii) after using the function u^{-1} on the gray levels of the projections. Two regions of slices of the reconstructed volume are displayed in Figure 3.10. They indicate that the gray level gradients in homogeneous areas are highly reduced, while being increased at the frontiers between the part and the background. This phenomenon is observed at a global scale (exterior surface, see Figures 3.10a and 3.10c) and at a more local scale (cooling holes, see Figures 3.10b and 3.10d). During the industrial inspection process, the tomographic volume is segmented into two parts: the object and the background. The volume reconstructed using corrected projections would lead to a more faithful segmentation and thus a more accurate control.

The findings of this study do have some limitations. Some phenomena that result in artifacts, *e.g.* afterglow, are still to be included in the model. The proposed method renders such additional corrections easily accessible once a suitable parametrization is

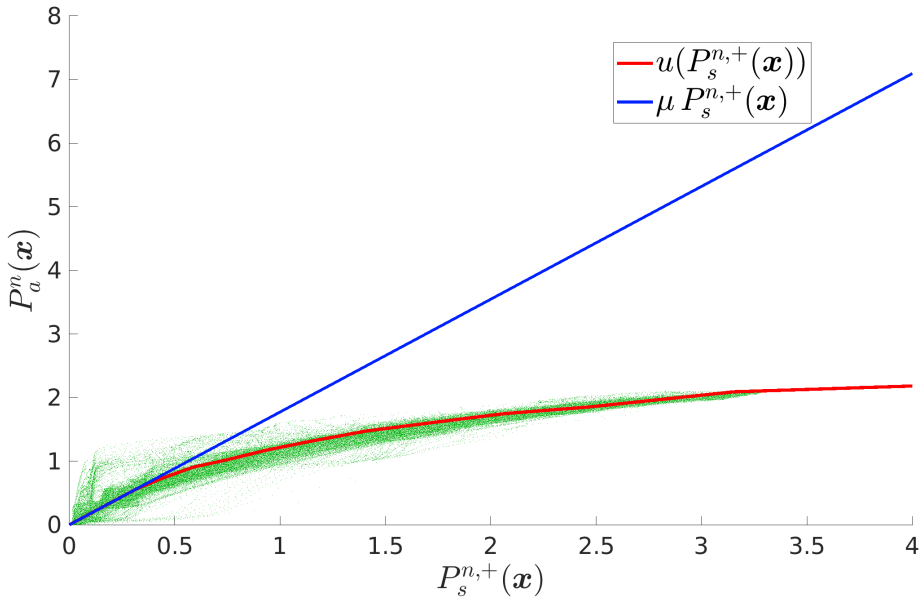

(a)

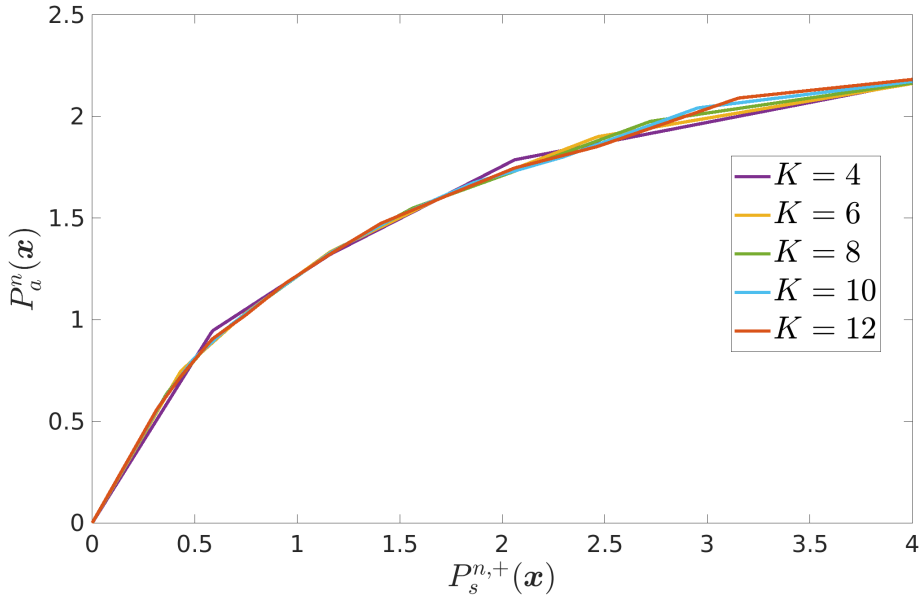

(b)

Figure 3.8: Result of the calibration of BH. (a) Result for a view n restricted to the associated ROI with K=8. The blue line shows the ideal case given by Beer-Lambert's law, *i.e.* no BH. The green point cloud presents the measurement $P_a^n(\boldsymbol{x})$. The red curve shows the piece-wise linear function u after calibration of the parameters c_k. (b) Estimated piece-wise linear function u with fewer and more parameters.

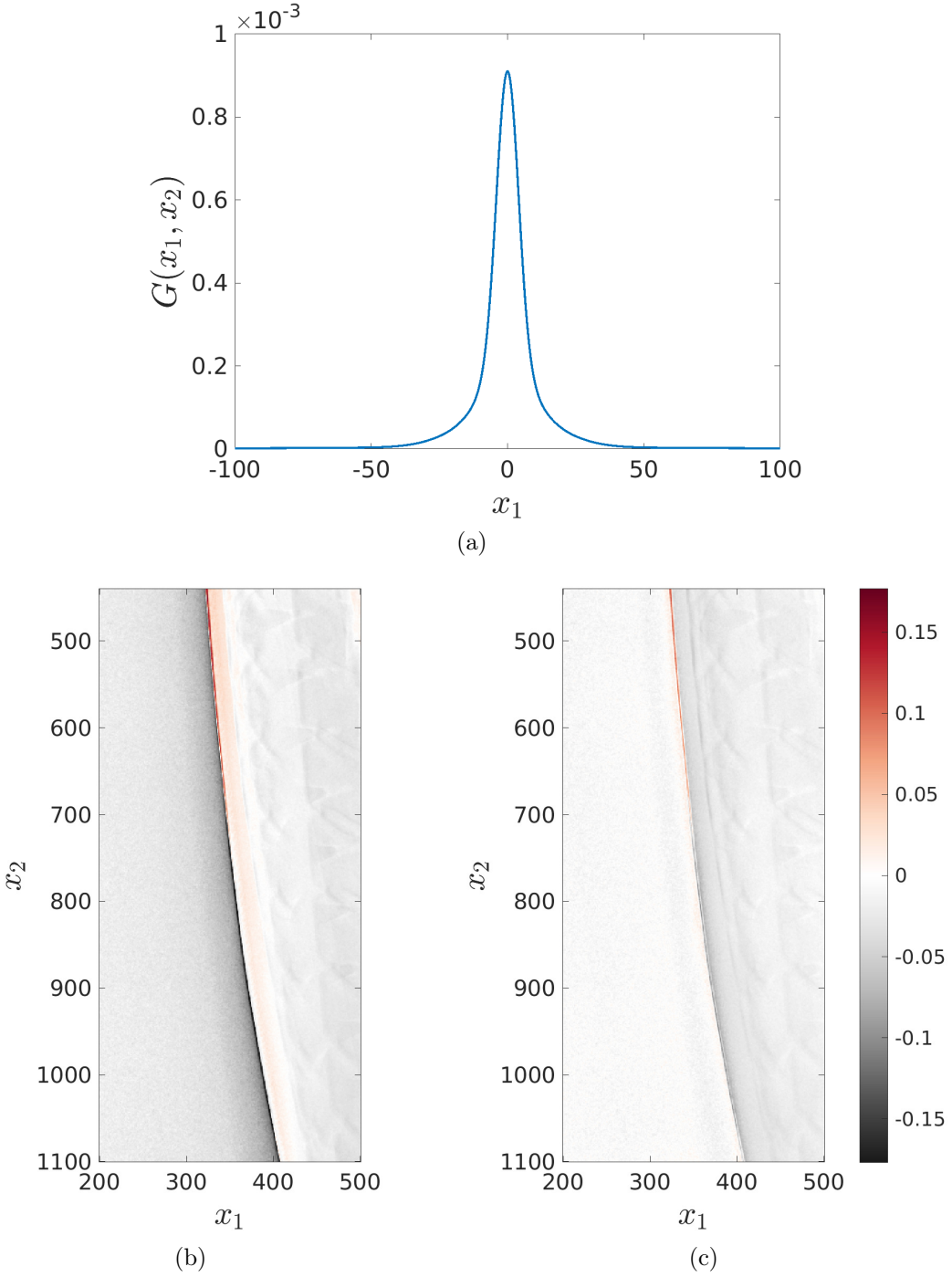

Figure 3.9: (a) Estimated scatter kernel G over x_1 for $x_2 = 0$. Difference (color) between acquired and simulated intensity images (b) without and (c) with scatter correction.

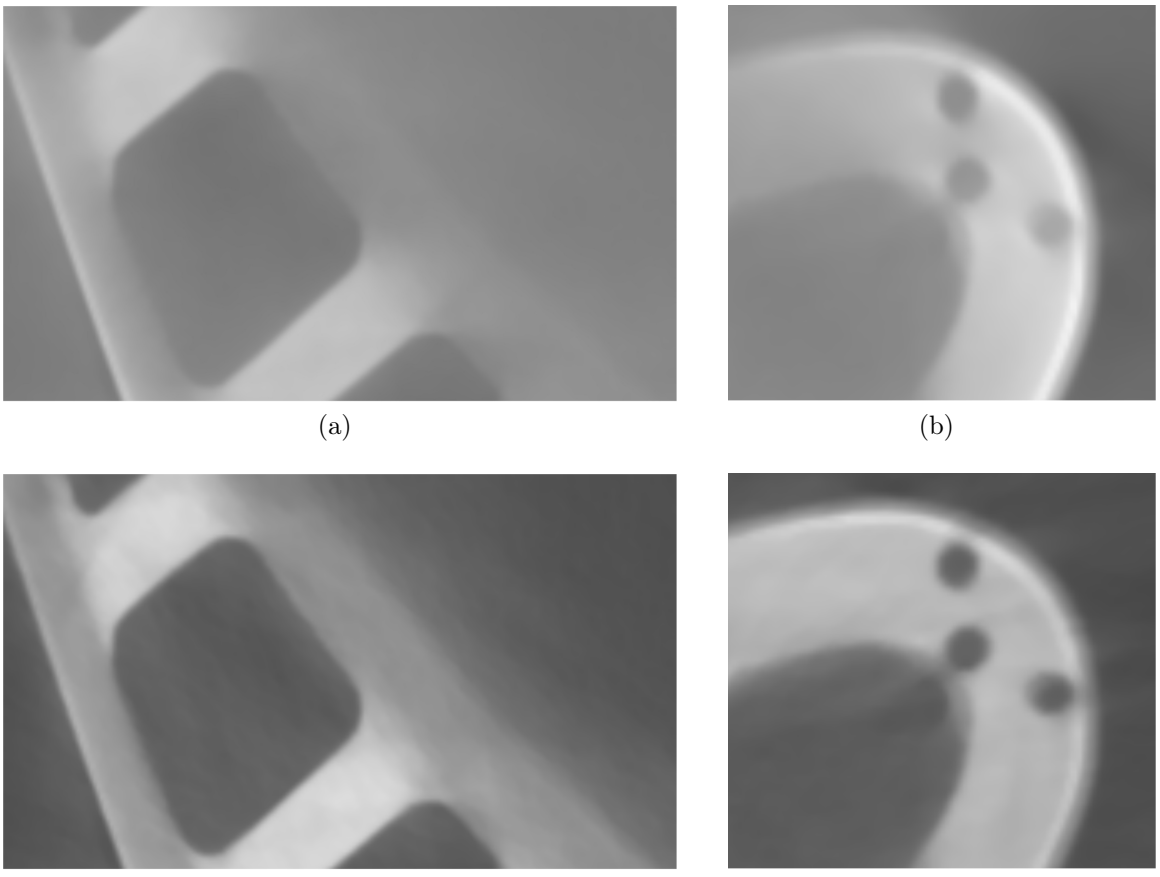

(a) (b)

(c) (d)

Figure 3.10: Tomographic volumes using (a) and (b) uncorrected projections, (c) and (d) projections corrected with the identified function u^{-1}.

formulated. Moreover, it is worth emphasizing that we addressed here the two phenomena (BH, Compton scattering) that are responsible for the largest deviation from the (monoenergetic) Beer Lambert's attenuation law. Regarding the identification of the projection geometry, the use of a simple geometry part might lead to an ill-posed problem. This point was not addressed nor studied in this work as it is not within the scope of this thesis. Additionally, the sensitivity fields rely on a linearization of the problem, which suggests that only small corrections are accessible to the procedure. This can be relaxed by a coarse-grained (*i.e.* multiscale) procedure, in which the residuals and sensitivity fields are observed at the most relevant scale. Finally, in practice, another limitation is the important computation time due to the voxelization step. The voxelization algorithm may be improved (*e.g.* parallelized) to make this step faster. Other strategies can be adopted to improve the execution time, *e.g.* compute the sensitivity fields in a single judiciously chosen direction and deduce the sensitivity fields in the other directions from the ones of the previous iteration. This limits the number of voxelization steps by iteration. Other X-ray simulation tools that use the CAD model directly, and thus do not require a voxelization step, might reduce the computation time. The ASTRA toolbox was used here as it was considered appropriate and sufficient for the scope of the thesis.

Complementary notes

Computing the sensitivity fields at each iteration tends to make the procedure time-consuming. A suggestion to avoid this problem consists in computing only one sensitivity field at each iteration (along a particular direction) and deriving the others by utilizing those computed at the previous iteration.

Consider iteration $t > 0$, such that all the sensitivity fields $s_k^n(\boldsymbol{x})$ have been calculated at least once in the iterative algorithm. The correction made at iteration $t-1$ leads to a modification of the parameters in a direction $\boldsymbol{v}$ (unit vector), from point $\boldsymbol{d^{t-2}}$ to point $\boldsymbol{d^{t-1}}$.

The directional derivatives of P_{s}^n at $\boldsymbol{d^{t-1}}$ in the direction of $\boldsymbol{v}$ are assumed to be different from those at $\boldsymbol{d^{t-2}}$ in the same direction. In the contrary, in a direction $\boldsymbol{w} \in \boldsymbol{v}^{\perp}$, the directional derivatives of P_{s}^n at $\boldsymbol{d^{t-1}}$ are assumed to remain close to those at $\boldsymbol{d^{t-2}}$ in the same direction.

Therefore, the sensitivity field is to be calculated in the direction of $\boldsymbol{v}$ only

$$\widetilde{s}_{\boldsymbol{v}}^n(\boldsymbol{x}) = \left.\frac{\partial P_{\mathrm{s}}^n(\boldsymbol{x};\boldsymbol{d})}{\partial \boldsymbol{v}}\right|_{\boldsymbol{d}=\boldsymbol{d^{t-1}}} \tag{3.16}$$

The projection tensors in the direction $\boldsymbol{v}$, $\mathbf{P}_{\boldsymbol{v}}^{\parallel} := \boldsymbol{v} \otimes \boldsymbol{v}$, and in the orthogonal space, $\mathbf{P}_{\boldsymbol{v}}^{\perp} := \boldsymbol{I} - \mathbf{P}_{\boldsymbol{v}}^{\parallel}$, are introduced. Then the sensitivity field $s_k^n(\boldsymbol{x})$ at the current iteration t, denoted $s_k^{n,t}(\boldsymbol{x})$, is approximated by the following decomposition

$$\begin{aligned} s_k^{n,t}(\boldsymbol{x}) &= \left[\left(\mathbf{P}_{\boldsymbol{v}}^{\parallel}\,\boldsymbol{e}_k\right)\cdot\boldsymbol{v}\right]\ \widetilde{s}_{\boldsymbol{v}}^n(\boldsymbol{x}) + \sum_j \left[\left(\mathbf{P}_{\boldsymbol{v}}^{\perp}\,\boldsymbol{e}_k\right)\cdot\boldsymbol{e}_j\right]\ s_j^{n,t-1}(\boldsymbol{x}) \\ &= v_k\,\widetilde{s}_{\boldsymbol{v}}^n(\boldsymbol{x}) + \sum_j \left[\delta_{kj} - v_k v_j\right]\ s_j^{n,t-1}(\boldsymbol{x}) \end{aligned}$$

The computation of the sensitivity fields using this formula may not be close enough to the actual sensitivity fields after a few iterations. It is therefore recommended to regularly recalculate exactly all the sensitivity fields. However, in between two global updates of all sensitivity fields, a single sensitivity is needed at each iteration, saving a considerable amount of time.

3.6 Conclusion

A parametric model describing the formation of images in X-ray CT-scanners that embeds phenomena occurring during acquisition, namely Compton scattering and BH, is presented. A calibration procedure is proposed to estimate the optimal values of the model parameters. Using the differences between observations and numerical simulations from the CAD model, their norm is minimized through the use of sensitivity fields. This method requires the acquisition of a few projections, without any calibration object, phantom, or landmark. Applied to a case study, the associated iterative algorithm has shown the feasibility and interest of the method as the residuals were significantly attenuated throughout the procedure. Only a few iterations are needed to obtain a stable solution with a reduced number of views. The CAD-based calibration procedure introduced in this paper allowed the determination of the projection geometry and estimation of X-ray artifacts arising from different phenomena.

The chosen parametrization ensures a well-behaved problem. The geometric correction however suffers from a degeneracy issue involving a scale factor, which is easily lifted by one additional length measurement. The number of parameters involved in the calibration procedure appears to have no impact on the quality of the calibration, provided that no degeneracy of the parametrization is introduced. The multi-view nature of the procedure is essential to produce a good estimate as it permits the model to take full advantage of different angles of projection.

In this study, the procedure has been carried out with a reduced number of views to meet the industrial demand for NDE of turbine blades. The final residuals reveal the discrepancies between the inspected part and the ideal design given by the CAD model. Based on this analysis, an NDE can be performed to control the part under inspection. For instance, a baseline measurement, *e.g.* derived from the noise found in a radiographic image, allows the detection of dimensional irregularities. It is shown that the estimated artifact corrections enhance the quality and reliability of the reconstructed tomographic volumes.

The question of the number of projections to be exploited is interesting. The method requires a minimal amount of information to estimate the various parameters. As more images N are considered, the accuracy in the estimation of the parameters is expected to improve asymptotically while the processing time is expected to increase linearly.

Acknowledgement

This work was supported by the French "Association Nationale de la Recherche et de la Technologie" (CIFRE n°2019/0793). The authors would like to thank Ms. Tonya Rose from the Digital Sciences and Technologies Departement at Safran for constructive feedback of the manuscript.

Bibliography

[1] Willi A. Kalender. *Computed tomography: fundamentals, system technology, image quality, applications*. John Wiley & Sons, 2011.

[2] Benjamin Pooya Fahimian, Yunzhe Zhao, Zhifeng Huang, Russell Fung, Yu Mao, Chun Zhu, Maryam Khatonabadi, John J. DeMarco, Stanley Joel Osher, Michael F. McNitt-Gray, and Jianwei Miao. Radiation dose reduction in medical x-ray CT via Fourier-based iterative reconstruction. *Medical Physics*, 40(3):031914, 2013.

[3] Jean-Pierre Kruth, Markus Bartscher, Simone Carmignato, Robert Schmitt, Leonardo De Chiffre, and Albert Weckenmann. Computed tomography for dimensional metrology. *CIRP Annals*, 60(2):821–842, 2011.

[4] Thomas De Schryver, Jelle Dhaene, Manuel Dierick, Matthieu N. Boone, Eline Janssens, Jan Sijbers, Mattias van Dael, Pieter Verboven, Bart Nicolai, and Luc Van Hoorebeke. In-line NDT with X-Ray CT combining sample rotation and translation. *NDT & E International*, 84:89–98, 2016.

[5] Petr Hermanek and Simone Carmignato. Porosity measurements by X-ray computed tomography: Accuracy evaluation using a calibrated object. *Precision Engineering*, 49:377–387, 2017.

[6] Arturo Mendoza, Julien Schneider, Estelle Parra-Denis, and Stéphane Roux. Measuring yarn deformations induced by the manufacturing process of woven composites. *Composites Part A: Applied Science and Manufacturing*, 120:127–139, 2019.

[7] Lee A. Feldkamp, Lloyd C. Davis, and James W. Kress. Practical cone-beam algorithm. *Journal of the Optical Society of America A*, 1(6):612–619, 1984.

[8] Marcel Beister, Daniel Kolditz, and Willi A. Kalender. Iterative reconstruction methods in X-ray CT. *Physica Medica*, 28(2):94–108, 2012.

[9] Thorsten Buzug. *Computed Tomography : From Photon Statistics to Modern Cone-Beam CT*. Springer, 2008.

[10] Rodney A. Brooks and Giovanni Di Chiro. Beam hardening in X-ray reconstructive tomography. *Physics in Medicine & Biology*, 21(3):390–398, 1976.

[11] Bruno De Man, Johan Nuyts, Patrick Dupont, Guy Marchal, and Paul Suetens. Metal streak artifacts in X-ray computed tomography: a simulation study. In *1998 IEEE Nuclear Science Symposium Conference Record. 1998 IEEE Nuclear Science Symposium and Medical Imaging Conference (Cat. No. 98CH36255)*, volume 3, pages 1860–1865. IEEE, 1998.

[12] Avinash C. Kak, Malcolm Slaney, and Ge Wang. Principles of computerized tomographic imaging. *Medical Physics*, 29(1):107, 2002.

[13] Ralf Schulze, Ulrich Heil, Daniel Gross, Dan Dominik Bruellmann, Egor Dranischnikow, Ulrich Schwanecke, and Elmar Schoemer. Artefacts in CBCT: a review. *Dentomaxillofacial Radiology*, 40(5):265–273, 2011.

[14] Pavel Müller. *Coordinate Metrology by Traceable Computed Tomography*. PhD thesis, Technical University of Denmark, Kgs. Lyngby, 2013.

[15] Timm Weitkamp and Pierre Bleuet. Automatic geometrical calibration for x-ray microtomography based on Fourier and Radon analysis. In *Developments in X-Ray Tomography IV*, volume 5535, pages 623–627. International Society for Optics and Photonics, 2004.

[16] Elke Van de Casteele, Dirk Van Dyck, Jan Sijbers, and Erik Raman. A Model-Based Correction Method for Beam Hardening Artefacts in X-ray microtomography. *Journal of X-Ray Science and Technology*, 12(1):43–57, 2003.

[17] Lane Alan Love and Robert A. Kruger. Scatter estimation for a digital radiographic system using convolution filtering. *Medical Physics*, 14(2):178–185, 1987.

[18] Miguel Sun and Josh M. Star-Lack. Improved scatter correction using adaptive scatter kernel superposition. *Physics in Medicine & Biology*, 55(22):6695–6720, 2010.

[19] Josh Star-Lack, Mingshan Sun, Anders Kaestner, Rene Hassanein, Gary Virshup, Timo Berkus, and Markus Oelhafen. Efficient scatter correction using asymmetric kernels. In Ehsan Samei and Jiang Hsieh, editors, *Medical Imaging 2009: Physics of Medical Imaging*, volume 7258, pages 644 – 655, 2009. Backup Publisher: International Society for Optics and Photonics.

[20] Navnina Bhatia, David Tisseur, Fanny Buyens, and Jean Michel Létang. Scattering correction using continuously thickness-adapted kernels. *NDT & E International*, 78:52–60, 2016. Publisher: Elsevier.

[21] B. Baygü, Fikri J. Kuchuk, and Orhan Arikan. Deconvolution Under Normalized Autocorrelation Constraints. *Spe Journal*, 2:246–253, 1997.

[22] Boukrouche Abdelhani. Une Technique de Minimisation pour la Déconvolution d'images. 05 2009.

[23] Wim Van Aarle, Willem Jan Palenstijn, Jeroen Cant, Eline Janssens, Folkert Bleichrodt, Andrei Dabravolski, Jan De Beenhouwer, Kees Joost Batenburg, and Jan Sijbers. Fast and flexible X-ray tomography using the ASTRA toolbox. *Optics express*, 24(22):25129–25147, 2016. Publisher: Optical Society of America.

[24] Yi Sun, Ying Hou, Fengyong Zhao, and Jiasheng Hu. A calibration method for misaligned scanner geometry in cone-beam computed tomography. *NDT & E International*, 39(6):499–513, 2006.

[25] Jochen Hiller, Michael Maisl, and Leo Reindl. Physical characterization and performance evaluation of an x-ray micro-computed tomography system for

dimensional metrology applications. *Measurement Science and Technology*, 23(8):085404, 2012.

[26] Michael Krumm, Stefan Kasperl, and Matthias Franz. Reducing non-linear artifacts of multi-material objects in industrial 3D computed tomography. *NDT & E International*, 41(4):242–251, 2008.

[27] Krishanan Arunmuthu, M. Ashish, Thangavelu Saravanan, John Philip, B. P. C. Rao, and T. Jayakumar. Simulation of beam hardening in X-ray tomography and its correction using linearisation and pre-filtering approaches. *Insight - Non-Destructive Testing and Condition Monitoring*, 55(10):540–547, 2013.

[28] Chalinee Thanasupsombat, Saowapak S. Thongvigitmanee, Sorapong Aootaphao, and Pairash Thajchayapong. A Simple Scatter Reduction Method in Cone-Beam Computed Tomography for Dental and Maxillofacial Applications Based on Monte Carlo Simulation. *BioMed Research International*, 2018:1–15, 2018.

[29] Ammar Alsaffar, Gasim Mammadov, and Sven Simon. Scattering Correction of CBCT Projections for the Quality Enhanced CT Reconstruction Using an Efficient Monte Carlo Photon Transport Model. In *10th Conference on Industrial Computed Tomography, Wels, Austria (iCT 2020)*, 2020.

[30] A signal processing model of diagnostic x-ray scatter.

[31] John M. Boone, Ben A. Arnold, and James Anthony Seibert. Characterization of the point spread function and modulation transfer function of scattered radiation using a digital imaging system. *Medical Physics*, 13(2):254–256, 1986.

[32] James Anthony Seibert and John M. Boone. X-ray scatter removal by deconvolution. *Medical Physics*, 15(4):567–575, 1988.

[33] Heng Li, Radhe Mohan, and Xiaorong Ronald Zhu. Scatter kernel estimation with an edge-spread function method for cone-beam computed tomography imaging. *Physics in Medicine & Biology*, 53(23):6729–6748, 2008.

[34] Bernd Ohnesorge, Thomas Flohr, and Klaus Klingenbeck-Regn. Efficient object scatter correction algorithm for third and fourth generation CT scanners. *European Radiology*, 9(3):563–569, 1999.

[35] Robin Degeilh. *Développement expérimental et modélisation d'un essai de fatigue avec gradient thermique de paroi pour application aube de turbine monocristalline*. PhD thesis, École normale supérieure de Cachan-ENS Cachan, 2013.

[36] Sandeep Patil and Bhallamudi Ravi. Voxel-based Representation, Display and Thickness Analysis of Intricate Shapes. In *Ninth International Conference on Computer Aided Design and Computer Graphics (CAD-CG'05)*, pages 415–422, Hong Kong, China, 2005. IEEE.

Chapter 4

Model-based measurement method

Contents

Reproduced from

Cédric Fragnaud, Clément Remacha, Julián Betancur, and Stéphane Roux. Model-based dimensional NDE from few X-ray radiographs: Application to the evaluation of wall thickness in metallic turbine blades. Submitted to *Precision Engineering*.

The extraction of 3D dimensional measurements based on a *limited* number of 2D X-ray radiographs of a part would offer a significant speed up of quality control procedures in industry. However, there are challenges with respect to both measurements and uncertainties. This chapter addresses these questions by creating an estimated numerical model of the imaged part, on which dimensional measurements can be made. The numerical model is chosen as a parametric deformation model that encodes the expected shape variability of the part resulting from the manufacturing process. The value of the deformation model parameters, and their uncertainties, are estimated by the registration of the computed projections of the model and the observed radiographs. The proposed approach is applied to the NDE of turbine blades manufactured by investment casting, and in particular to the measurement of their wall thickness, which is a critical element. The deformable model consists in partitioning the inner ceramic core into multiple subparts, which may undergo a rigid body motion with respect to the master die. Wall thickness measurements and their uncertainties can be determined from the estimation of these rigid body motions. To assess the reliability of the proposed procedure, a repeatability study has been performed, as well as a direct

comparison with "ground truth" measurements from a reconstructed tomogram. Both of them show the reliability and efficiency of the proposed approach for wall thickness measurement. Residual differences between captured and computed projections were observed. Despite these model errors revealing localized shape mismatches, the approach has been demonstrated to be operable.

4.1 Introduction

Non Destructive Evaluation (NDE) is performed in industry to control the quality of produced parts ensuring that they meet their technical specifications. The increasing complexity of part geometry calls for developing more advanced NDE methods. The necessity of NDE is even more stringent in sectors where safety is critical, such as aeronautics.

Turbine blades are key parts of aircraft engines. Their complex geometry is meticulously designed and optimized [1, 2, 3, 4] to improve the performance of the engine. In particular, internal air cooling channels allow metal blades to operate at temperatures *higher* than their melting point [5, 6, 7]. These extremely high temperatures are necessary to increase the power and fuel efficiency of aircraft engines. Turbine blades are fabricated following a high precision manufacturing process; nevertheless, geometrical indications — *i.e.* dimensional irregularities of the part that may result in a sub-optimal behavior of the engine — may appear [8]. To ensure the structural integrity of the manufactured turbine blades, it is crucial to have high precision measurements regarding the geometry of the part for quality control.

Coordinate Measuring Machines (CMM) [9, 10] have been used to identify external dimensional imperfections. However, they are not suited to detect internal dimensional imperfections (such as cavities or just complex non-convex shapes). To this end, radiographic imaging methods, and in particular X-ray imaging, have been adopted [11, 12, 13]. The acquisition of a large number of X-ray radiographs allows the 3D image (tomography or tomogram) of the part to be reconstructed. By aligning the nominal model to the reconstructed volume, it is possible to compare the inspected part with its ideal design and extract measurements of deviation. However, this process requires long acquisition and processing times considering production needs. Thus, in production lines, each part is observed from a limited number of views. These images are then inspected by specialist operators seeking an unusual gray level difference indicating an irregularity of the part. The measurement of 3D indications from 2D radiographs remains a complex problem for which automated methodology and procedures are highly desirable.

This chapter presents an NDE method exploiting a limited number of X-ray images of the part. It relies on the simulation of the X-ray images from a numerical model of the part using an adequate and calibrated projective model [14, 15]. The CAD model is extended to a parametric deformable model so that the projections of the inspected part are registered onto the acquired X-ray images. 3D measurements and the associated uncertainty can be computed on the corrected model, which corresponds to the deformable model computed for the optimal transformation parameters. Section 4.2 is devoted to describing the developed method. More specifically, a discussion regarding the studied dimensional control, namely the wall thickness measurement,

is provided in Section 4.2.1. There, a discussion is proposed on the uncertainty of kinematics based on rigid body motion. The method to identify the optimal transformation parameters is then presented in Section 4.2.2. A deformable model derived from the manufacturing process of turbine blades is proposed in Section 4.2.3. The parameter identification method and the deformable model are the key features to generate a corrected numerical model. A repeatability study to assess the reliability of the proposed approach to measure the wall thickness of a turbine blade is formalized in Section 4.2.4. It consists of the wall thickness measurement of various samples of a turbine blade, each inspection being repeated multiple times. Section 4.3 reports and discusses the results of this study. They reveal that, even with the presence of model errors, the method is capable of generating a corrected model comparable to the ground truth (tomogram), which implies similar calculated wall thicknesses.

4.2 Methods

An NDE procedure to compute variations in the wall thickness of turbine blades based on a limited number of X-ray images has been developed. It requires a deformable model M of the inspected part whose shape is controlled by a set of *transformation parameters*. A registration methodology is proposed to identify the transformation parameters of a reference model of the imaged part that best describe the difference between computed projections and observed radiographs.

Prior to discussing the model parametrization and the method employed to identify the optimal transformation parameters, the principle of the studied dimensional control is introduced.

4.2.1 Wall thickness metrology

Wall thickness corresponds to the distance between two surfaces $\mathcal{S}_1$ and $\mathcal{S}_2$, be they internal or external. This distance W_{12} is classically defined as

$$W_{12} = \min_{\substack{\boldsymbol{p}_1 \in \mathcal{S}_1 \\ \boldsymbol{p}_2 \in \mathcal{S}_2}} \|\boldsymbol{p}_1 - \boldsymbol{p}_2\|_2 \tag{4.1}$$

where $\boldsymbol{p}_1$ and $\boldsymbol{p}_2$ correspond to points on surfaces $\mathcal{S}_1$ and $\mathcal{S}_2$, respectively. This definition is however not very convenient from an operational point of view since $\boldsymbol{p}_1$ (resp. $\boldsymbol{p}_2$) has to visit the entire surface $\mathcal{S}_1$ (resp. $\mathcal{S}_2$), and the minimum may not be unique. Hence, in practice, further restrictions can be enforced on $\boldsymbol{p}_1$ or $\boldsymbol{p}_2$. In the following, this distance is computed using the "Ray method" implemented in VG Studio MAX (Volume Graphics GmbH, v 2.2). Namely, an initial point $\boldsymbol{p}_1^0$ is chosen along surface $\mathcal{S}_1$, together with a solid angle of possible search. The closest point to $\boldsymbol{p}_1^0$ along surface $\mathcal{S}_2$ is found, and denoted $\boldsymbol{p}_2^1$. Then, the role of the two surfaces is interchanged, and the closest point to $\boldsymbol{p}_2^1$ along surface $\mathcal{S}_1$ is sought (with the same solid angle restrictions), and its minimum is denoted $\boldsymbol{p}_2^1$. This process is repeated until convergence, where a stationary solution $(\boldsymbol{p}_1, \boldsymbol{p}_2)$ is found. To avoid that the points get out of a neighborhood of the initial point $\boldsymbol{p}_1^0$, it is necessary to consider escape conditions where the process does not converge. In case of success, the resulting distance is noted as $W_{12}(\boldsymbol{p}_1^0)$. This procedure is applied starting for all nodes of the mesh that lie on surface $\mathcal{S}_1$, and finally $W_{12} = \min_{\boldsymbol{p}_1^0} W_{12}(\boldsymbol{p}_1^0)$. Although not strictly identical to the

above mathematical definition, eq. (4.1), this evaluation of the distance is a very good approximation when a careful choice of neighborhood is made, and hence the exact definition will be considered when required in the theoretical analysis.

In the following, a specific class of transformations applied to the surfaces defining the deformation model will be considered, namely rigid body motions. A brief discussion about their uncertainty is proposed before assessing the fluctuation of wall thickness measurement resulting from a rigid body motion.

4.2.1.1 Rigid body motion uncertainty

A rigid body motion is mathematically described by the screw theory [16] and can be represented by a rotation $\boldsymbol{R}$ and translation $\boldsymbol{T}(\boldsymbol{q})$ at an arbitrary point $\boldsymbol{q}$. Although $\boldsymbol{R}$ is intrinsic, the translation depends on the chosen reference point $\boldsymbol{q}$. More precisely, if another point $\boldsymbol{q'}$ is chosen, then $\boldsymbol{T}(\boldsymbol{q'}) = \boldsymbol{T}(\boldsymbol{q}) + (\boldsymbol{q'q}) \times \boldsymbol{R}$.

An aspect that deserves specific comments is the uncertainty of the measured rigid body motion. From image registration, a displacement field can be calculated which can be described by its average $\mathcal{M}_{\boldsymbol{q}} = (\boldsymbol{T}(\boldsymbol{q}), \boldsymbol{R})$ and its fluctuation, $\delta\mathcal{M}_{\boldsymbol{q}} = (\delta\boldsymbol{T}(\boldsymbol{q}), \delta\boldsymbol{R})$. This fluctuation is characterized by a null expectation value and a covariance matrix $\mathbf{C}_{\boldsymbol{q}}$, embedding the rigid body motion uncertainty, composed of three terms, each of which is a 3×3 matrix:

$$\begin{aligned} \mathbf{C}_{\boldsymbol{q}}^{(1)} &:= \langle \delta\boldsymbol{T}(\boldsymbol{q}) \otimes \delta\boldsymbol{T}(\boldsymbol{q}) \rangle \\ \mathbf{C}_{\boldsymbol{q}}^{(2)} &:= \langle \delta\boldsymbol{T}(\boldsymbol{q}) \otimes \delta\boldsymbol{R} \rangle \\ \mathbf{C}^{(3)} &:= \langle \delta\boldsymbol{R} \otimes \delta\boldsymbol{R} \rangle \end{aligned} \tag{4.2}$$

where $\langle \cdot \rangle$ denotes the average of the quantities within the angle braces, and $\otimes$ the tensor product. These terms completely define $\mathbf{C}_{\boldsymbol{q}}$ which reads $\mathbf{C}_{\boldsymbol{q}} = \begin{pmatrix} \mathbf{C}_{\boldsymbol{q}}^{(1)} & \mathbf{C}_{\boldsymbol{q}}^{(2)} \\ \mathbf{C}_{\boldsymbol{q}}^{(2)\top} & \mathbf{C}^{(3)} \end{pmatrix}$. The covariance matrix of the rotation $\mathbf{C}^{(3)}$ is intrinsic. Considering it is a symmetric positive matrix, it can be diagonalized in the basis of eigenvectors $\mathcal{B}$. However, the full covariance matrix $\mathbf{C}_{\boldsymbol{q}}$ is not intrinsic. In particular, the non-diagonal terms of the cross-correlation $\mathbf{C}_{\boldsymbol{q}}^{(2)}$ depend on the chosen reference point $\boldsymbol{q}$. It can be shown that there exists a unique point, denoted $\boldsymbol{q}^*$, such that the antisymmetric part of $\mathbf{C}_{\boldsymbol{q}^*}^{(2)}$ is exactly zero. A privileged frame of reference is then $\boldsymbol{q}^*$ as the origin while the axes orientations are given by $\mathcal{B}$.

Complementary notes

In order to find the expression for the point $\boldsymbol{q}^*$ such that the antisymmetric part of $\mathbf{C}_{\boldsymbol{q}^*}^{(2)}$ is zero, let us first define the antisymmetric tensor $\boldsymbol{A}(\boldsymbol{q})$ of $\mathbf{C}_{\boldsymbol{q}}^{(2)}$:

$$[A(\boldsymbol{q})]_{ij} := \frac{1}{2}\left(\left[\mathrm{C}_{\boldsymbol{q}}^{(2)}\right]_{ij} - \left[\mathrm{C}_{\boldsymbol{q}}^{(2)}\right]_{ji} \right) \tag{4.3}$$

The associated *dual* (or *axial*) vector $\boldsymbol{a}(\boldsymbol{q})$ reads

$$\begin{aligned}
[a(\boldsymbol{q})]_k &:= -\frac{1}{2}\epsilon_{ijk}\,[A(\boldsymbol{q})]_{ij} \\
&= -\frac{1}{4}\,\epsilon_{ijk}\left(\left[\mathrm{C}_{\boldsymbol{q}}^{(2)}\right]_{ij} - \left[\mathrm{C}_{\boldsymbol{q}}^{(2)}\right]_{ji}\right) \\
&= -\frac{1}{4}\,(\epsilon_{ijk} - \epsilon_{jik})\left[\mathrm{C}_{\boldsymbol{q}}^{(2)}\right]_{ij} \\
&= -\frac{1}{2}\,\epsilon_{ijk}\left[\mathrm{C}_{\boldsymbol{q}}^{(2)}\right]_{ij}
\end{aligned} \tag{4.4}$$

where ϵ_{ijk} denotes the Levi-Civita symbol and the Einstein summation convention is used. Considering another point $\boldsymbol{q'}$, it is written as

$$\begin{aligned}
[a(\boldsymbol{q'})]_k &= -\frac{1}{2}\,\epsilon_{ijk}\left[\mathrm{C}_{\boldsymbol{q'}}^{(2)}\right]_{ij} \\
&= -\frac{1}{2}\,\epsilon_{ijk}\left(\left[\mathrm{C}_{\boldsymbol{q}}^{(2)}\right]_{ij} + \epsilon_{ilm}\,[\boldsymbol{q}\boldsymbol{q'}]_l\left[\mathrm{C}_{\boldsymbol{q}}^{(3)}\right]_{mj}\right) \\
&= -\frac{1}{2}\,\epsilon_{ijk}\left[\mathrm{C}_{\boldsymbol{q}}^{(2)}\right]_{ij} - \frac{1}{2}\,\epsilon_{ijk}\,\epsilon_{ilm}\,[\boldsymbol{q}\boldsymbol{q'}]_l\left[\mathrm{C}_{\boldsymbol{q}}^{(3)}\right]_{mj}
\end{aligned} \tag{4.5}$$

Using

$$\sum_i \epsilon_{ijk}\,\epsilon_{ilm} = \delta_{jl}\,\delta_{km} - \delta_{jm}\,\delta_{kl} \tag{4.6}$$

with δ_{jl} the Kronecker symbol, we can rewrite $[a(\boldsymbol{q'})]_k$ as

$$[a(\boldsymbol{q'})]_k = [a(\boldsymbol{q})]_k - \frac{1}{2}\left([\boldsymbol{q}\boldsymbol{q'}]_j\left[\mathrm{C}_{\boldsymbol{q}}^{(3)}\right]_{kj} - [\boldsymbol{q}\boldsymbol{q'}]_k\left[\mathrm{C}_{\boldsymbol{q}}^{(3)}\right]_{jj}\right) \tag{4.7}$$

Finally

$$\boldsymbol{a}(\boldsymbol{q'}) = \boldsymbol{a}(\boldsymbol{q}) - \frac{1}{2}\left(\mathbf{C}_{\boldsymbol{q}}^{(3)} - tr\left(\mathbf{C}_{\boldsymbol{q}}^{(3)}\right)\boldsymbol{I}\right)(\boldsymbol{q}\boldsymbol{q'}) \tag{4.8}$$

with I the identity matrix, and tr the trace operator. Then there exist a unique point, denoted $\boldsymbol{q}^*$, such that $\boldsymbol{a}(\boldsymbol{q}^*) = 0$, given by

$$(\boldsymbol{q}\boldsymbol{q}^*) = 2\left(\mathbf{C}_{\boldsymbol{q}}^{(3)} - tr\left(\mathbf{C}_{\boldsymbol{q}}^{(3)}\right)\boldsymbol{I}\right)^{-1}\boldsymbol{a}(\boldsymbol{q}) \tag{4.9}$$

$$\implies \boldsymbol{q}^* = \boldsymbol{q} + 2\left(\mathbf{C}_{\boldsymbol{q}}^{(3)} - tr\left(\mathbf{C}_{\boldsymbol{q}}^{(3)}\right)\boldsymbol{I}\right)^{-1}\boldsymbol{a}(\boldsymbol{q}) \tag{4.10}$$

4.2.1.2 Uncertainty of the distance between surfaces

Rigid body motions are applied to the surfaces $\mathcal{S}_1$ and $\mathcal{S}_2$. Because the definition of the distance between surfaces, eq. (4.1), is not affected by a global rigid body motion affecting both surfaces, only the relative displacement of one surface with respect to the other matters. Thus only $\mathcal{S}_2$ may be considered to be moving while $\mathcal{S}_1$ remains static. The uncertainty of the measurement of W_{12} results from the uncertainty of the

rigid body motion affecting $\mathcal{S}_2$. This question is addressed subsequently.

Let $\boldsymbol{p}_1^*$ denote the point on surface $\mathcal{S}_1$ where the minimum distance to $\mathcal{S}_2$ is found, at point $\boldsymbol{p}_2^*$. The surfaces are supposed to be smooth (no angular edge or corner) in the neighborhood of $\boldsymbol{p}_1^*$ and $\boldsymbol{p}_2^*$ so that the surface around them can be described as parabolic. After applying the transformation $\delta\mathcal{M}_{\boldsymbol{q}}$ to $\mathcal{S}_2$, the shortest distance between the surfaces changes. Assuming the rigid body motion $\delta\mathcal{M}_{\boldsymbol{q}}$ is of small amplitude, a first order expansion of the change in distance δW_{12} is found to be a translation along the normal common to both surfaces $\boldsymbol{n} = \boldsymbol{p}_1^*\boldsymbol{p}_2^* / \left|\boldsymbol{p}_1^*\boldsymbol{p}_2^*\right|$.

This translation is however not intrinsic as it depends on the point at which the rigid body motion is expressed (section 4.2.1.1). There exists a unique point $\boldsymbol{q}^*$ for which the antisymmetric part of the cross-correlation between $\delta\boldsymbol{R}$ and $\delta\boldsymbol{T}(\boldsymbol{q}^*)$ in the covariance matrix is null. Thus, this point is chosen to compute the statistics of the correlation $\mathbf{C}_{\boldsymbol{q}^*}$, and the orientation of the frame is chosen to be given by the above introduced basis of eigenvectors $\mathcal{B}$. The variance of δW_{12} then reads

$$\left\langle \delta W_{12}^2 \right\rangle = \left(\mathbf{C}_{\boldsymbol{q}^*}^{(1)} + \left|\boldsymbol{q}^*\boldsymbol{p}_2^*\right|^2 \mathbf{C}^{(3)} \right) : (\boldsymbol{n} \otimes \boldsymbol{n}) + \mathbf{C}_{\boldsymbol{q}^*}^{(2)} : ((\boldsymbol{q}^*\boldsymbol{p}_2^*) \otimes \boldsymbol{n}) \tag{4.11}$$

where : denotes the double dot product.

These findings rely on the assumption that surfaces are smooth in the neighborhood of $\boldsymbol{p}_1^*$ and $\boldsymbol{p}_2^*$. Additionally, the determination of $\boldsymbol{p}_i^*$ after the transformation $\delta\mathcal{M}_{\boldsymbol{q}}$ requires the curvature tensor $(\boldsymbol{\kappa}_1 + \boldsymbol{\kappa}_2 + W_{12}\,\boldsymbol{\kappa}_1\,\boldsymbol{\kappa}_2)$ to be inverted, where $\boldsymbol{\kappa}_1$ and $\boldsymbol{\kappa}_2$ denote the curvature tensor of surfaces $\mathcal{S}_1$ and $\mathcal{S}_2$, respectively. When the two surfaces approach a flat configuration, the inversion gives rise to high values, so that the first order approximation assumption must be carefully assessed. The curvature tensor may even become negative, in which case the determination of $\boldsymbol{p}_i^*$ may be unstable. One should note that, even if the position of the points $\boldsymbol{p}_i^*$ becomes variable, the distance W_{12} itself may remain well behaved, but firm conclusions using the above development rest on the assumption that the change in $\boldsymbol{p}_i^*$ remains small.

Therefore, wall thickness should be computed on smooth surfaces and for which the curvature tensor $(\boldsymbol{\kappa}_1 + \boldsymbol{\kappa}_2 + W_{12}\,\boldsymbol{\kappa}_1\,\boldsymbol{\kappa}_2)$ is well-conditioned (stable inversion) to obtain consistent and reliable measurements. In the following, wall thickness is measured at measurement points located in the airfoil of the blade, in accordance with these recommendations.

Complementary notes

The expression of δW_{12} is here detailled. The two surfaces may be described locally as parabolic with a tangent plane perpendicular to $\boldsymbol{p}_1^*\boldsymbol{p}_2^*$. Let us introduce a coordinate system such that the first two coordinates $(u, v) = \boldsymbol{u}$ are that of the tangent plane, and the third coordinate, denoted w, is along $\boldsymbol{p}_1^*\boldsymbol{p}_2^*$. Then surfaces $\mathcal{S}_1$ and $\mathcal{S}_2$ can be respectively written as

$$w = -W_{12} - \frac{1}{2}\,\boldsymbol{u}^\top\,\boldsymbol{\kappa}_1\,\boldsymbol{u} \tag{4.12}$$

$$w = \frac{1}{2}\,\boldsymbol{u}^\top\,\boldsymbol{\kappa}_2\,\boldsymbol{u} \tag{4.13}$$

where $\boldsymbol{\kappa}_i$ is a 2×2 matrix describing the curvature of the surface $\mathcal{S}_i$.

Let $(\boldsymbol{u}_2, w_2)$ be a point on surface $\mathcal{S}_2$, w_2 being given by $w_2 = \frac{1}{2}\,\boldsymbol{u}_2\,\boldsymbol{\kappa}_2\,\boldsymbol{u}_2$.

The surface $\mathcal{S}_2$ is subjected to the fluctuating part of the rigid body motion $\delta\mathcal{M}_{\boldsymbol{q}}$ (while the surface $\mathcal{S}_1$ stays invariant), causing the point to be moved to $(\boldsymbol{u}_2', w_2')$:

$$\boldsymbol{u}_2' = \boldsymbol{A}\boldsymbol{u}_2 + \boldsymbol{B}w_2 + \boldsymbol{D} \tag{4.14}$$
$$w_2' = -\boldsymbol{B}\cdot\boldsymbol{u}_2 + Cw_2 + E \tag{4.15}$$

where we have introduced $\boldsymbol{A}$ (2×2 matrix) which is a rotation transformation in the tangent plane (of axis w), $\boldsymbol{B}$ a vector of the tangent plane that results from rotations about an axis in the tangent plane and C is the corresponding translation along w, $\boldsymbol{D}$ is a translation in the tangent plane, and E along w. The rigid body motion $\delta\mathcal{M}_{\boldsymbol{q}}$ is assumed to be of small amplitude, so that only a first order expansion with respect to the rotation (off diagonal term in $\boldsymbol{A}$ and vector $\boldsymbol{B}$) and translation ($\boldsymbol{D}$ and E) is needed. The diagonal terms of $\boldsymbol{A}$ and C are thus valued 1 up to second order corrections which are neglected.

After moving surface $\mathcal{S}_2$, the shortest distance between the surfaces changes. Point $\boldsymbol{p}_1^*$ is now at position $(\boldsymbol{u}_1, w_1)$, and on the displaced surface $\mathcal{S}_2$, $\boldsymbol{p}_2^*$ is now denoted $(\boldsymbol{u}_2', w_2')$. The question is now to determine those two points and the resulting distance W_{12}'. The latter reads

$$\begin{aligned} W_{12}'^2 &= (\boldsymbol{u}_1 - \boldsymbol{u}_2')^2 + (w_1 - w_2')^2 \\ &= \left(\boldsymbol{u}_1 - \boldsymbol{A}\boldsymbol{u}_2 + \frac{1}{2}(\,\boldsymbol{u}_2^\top\,\boldsymbol{\kappa}_2\,\boldsymbol{u}_2)\boldsymbol{B} + \boldsymbol{D}\right)^2 \\ &\quad + \left(-W_{12} - \frac{1}{2}\boldsymbol{u}_1^\top\,\boldsymbol{\kappa}_1\,\boldsymbol{u}_1 + \boldsymbol{B}^\top\boldsymbol{u}_2 - \frac{1}{2}\boldsymbol{u}_2^\top\,\boldsymbol{\kappa}_2\,\boldsymbol{u}_2 - E\right)^2 \end{aligned} \tag{4.16}$$

The two points $\boldsymbol{p}_i^*$ are determined from $\left.\dfrac{\partial W_{12}'^2}{\partial \boldsymbol{p}_i}\right|_{\boldsymbol{p}_i=\boldsymbol{p}_i^*} = 0$. Hence, $\partial W_{12}'^2/\partial\boldsymbol{u}_1$ and $\partial W_{12}'^2/\partial\boldsymbol{u}_2$ are computed and set to 0. Only the first-order terms in the rigid body motion are retained in their expressions, assuming that $\boldsymbol{u}_1$ and $\boldsymbol{u}_2$ are themselves of order 1. We first keep their expressions truncated at order 1 in $\boldsymbol{u}_i$, and we further simplify ($E \ll W_{12}$, $\boldsymbol{A} = \boldsymbol{I} + \mathcal{O}(\epsilon)$, …), yielding

$$(\boldsymbol{I} + W_{12}\,\boldsymbol{\kappa}_1)\,\boldsymbol{u}_1 - \boldsymbol{I}\boldsymbol{u}_2 = -\boldsymbol{D} \tag{4.17}$$
$$-\boldsymbol{I}\boldsymbol{u}_1 + (\boldsymbol{I} + W_{12}\,\boldsymbol{\kappa}_2)\,\boldsymbol{u}_2 = \boldsymbol{D} + W_{12}\,\boldsymbol{B} \tag{4.18}$$

hence

$$\boldsymbol{u}_1 = (\boldsymbol{I} + W_{12}\,\boldsymbol{\kappa}_2)\,\boldsymbol{u}_2 - \boldsymbol{D} - W_{12}\boldsymbol{B} \tag{4.19}$$
$$(\boldsymbol{\kappa}_1 + \boldsymbol{\kappa}_2 + W_{12}\,\boldsymbol{\kappa}_1\,\boldsymbol{\kappa}_2)\,\boldsymbol{u}_2 = \boldsymbol{B} + \boldsymbol{\kappa}_1\boldsymbol{D} + W_{12}\,\boldsymbol{\kappa}_1\boldsymbol{B} \tag{4.20}$$

One is finally interested in the distance between the surfaces after this motion.

$$W_{12}'^2 = W_{12}^2 + 2\,W_{12}\,\delta W_{12} + \mathcal{O}(\epsilon^2) \tag{4.21}$$
$$= W_{12}^2 + 2\,W_{12}\,(E - \boldsymbol{B}^\top\boldsymbol{u}_2) + \mathcal{O}(\epsilon^2) \tag{4.22}$$

Hence

$$\delta W_{12} = E - \boldsymbol{B}^\top\boldsymbol{u}_2 \tag{4.23}$$

The change in distance has a first contribution which is the translation along the common surface normals E and since the closest point on surface $\mathcal{S}_2$ has been moved by $\boldsymbol{u}_2$, the rotation induces a motion along this normal which reads $\boldsymbol{B} \cdot \boldsymbol{u}_2$. Using eq. (4.20), δW_{12} reads

$$\delta W_{12} = E - \boldsymbol{B}^\top \left(\boldsymbol{\kappa}_1 + \boldsymbol{\kappa}_2 + W_{12}\, \boldsymbol{\kappa}_1\, \boldsymbol{\kappa}_2\right)^{-1} \left(\boldsymbol{B} + \boldsymbol{\kappa}_1 \left(\boldsymbol{D} + W_{12}\, \boldsymbol{B}\right)\right) \tag{4.24}$$

Let us note that the second term is of order $\boldsymbol{B}^2$ or $\boldsymbol{B}\boldsymbol{D}$, and is thus negligible. This corresponds to expanding the cosine of a small angle θ which departs from 1 by $\theta^2/2$, and which can be discarded in a perturbative expansion to first order.

4.2.2 Identification of transformation parameters

Transformation parameters are identified by registering numerically simulated X-ray projections onto the corresponding set of radiographs that constitutes the observations. It is thus essential to consider a simulation tool capable of producing realistic X-ray images accounting for multiple phenomena such as beam hardening and/or scattering, and the appropriate projection geometry [15]. The N acquired radiographs of the inspected part are denoted $P_{\mathrm{a}}^n(\boldsymbol{x})\,, n \leq N$, where $\boldsymbol{x}$ represents the pixel position and n is the index of the view (different views implying different orientations of the part). Let Π^n be the projection operator for the view n acting on the model M. The acquired images correspond to the projections of a modified version of the model polluted by noise

$$P_{\mathrm{a}}^n(\boldsymbol{x}) \approx \Pi^n[M(\boldsymbol{d})](\boldsymbol{x}) + \eta^n(\boldsymbol{x}) \tag{4.25}$$

where $\boldsymbol{d}$ is the K-component vector containing the transformation parameters d_k, and $\eta^n(\boldsymbol{x})$ denotes the acquisition noise. Because of the detector and the cone-beam geometry of the source, acquisition noise is not homogeneous and is characterized by a variance that depends on pixel localization, noted as $V^n(\boldsymbol{x})$. Although a dependence on n is not generally expected, the averaging of the images performed during the acquisition of the radiographs is likely to depend on the projection angle to compensate for different attenuations related to the part orientation. The following cost function is introduced

$$\Psi(\boldsymbol{d}) = \sum_n \left\| \frac{1}{\sqrt{V^n(\boldsymbol{x})}} \left(P_{\mathrm{a}}^n(\boldsymbol{x}) - \Pi^n[M(\boldsymbol{d})](\boldsymbol{x})\right) \right\|_2^2 \tag{4.26}$$

Minimizing this function with respect to $\boldsymbol{d}$ leads to the identification of the optimal transformation parameters. The weight term involving $V^n(\boldsymbol{x})$ accounts for local uncertainties brought by the noise. The weighted L_2-norm in eq (4.26) is justified as being optimal for the acquisition noise. This problem is solved iteratively using a gradient descent algorithm. At iteration t, the correction vector $\boldsymbol{\delta d}$ corresponds to small perturbations, so that the above cost function is linearized about the solution $\boldsymbol{d}^t = \boldsymbol{d}^{t-1} + \boldsymbol{\delta d}$

$$\Psi_{\text{lin}}(\boldsymbol{\delta d}) = \sum_n \left\| \frac{1}{\sqrt{V^n(\boldsymbol{x})}} \left(P_{\text{a}}^n(\boldsymbol{x}) - \Pi^n\big[M\big(\boldsymbol{d}^{t-1}\big)\big](\boldsymbol{x}) - \Pi^n\big[\boldsymbol{\nabla}_{\boldsymbol{d}} M\big(\boldsymbol{d}^{t-1}\big)\big](\boldsymbol{x}) \cdot \boldsymbol{\delta d} \right) \right\|_2^2 \tag{4.27}$$

where $\boldsymbol{\nabla}_{\boldsymbol{d}} M$ denotes the derivative of M with respect to $\boldsymbol{d}$. The projection residuals and the sensitivity fields are defined respectively as

$$\rho^n(\boldsymbol{x}) = P_{\text{a}}^n(\boldsymbol{x}) - \Pi^n\big[M\big(\boldsymbol{d}^{t-1}\big)\big](\boldsymbol{x}) \tag{4.28}$$

$$s_k^n(\boldsymbol{x}) = \Pi^n\left[\frac{\partial M}{\partial d_k}\big(\boldsymbol{d}^{t-1}\big)\right](\boldsymbol{x}) \tag{4.29}$$

Applying (4.28) and (4.29) in (4.27), the linearized cost function is rewritten as

$$\Psi_{\text{lin}}(\boldsymbol{\delta d}) = \sum_n \left\| \frac{1}{\sqrt{V^n(\boldsymbol{x})}} \left(\rho^n(\boldsymbol{x}) - \sum_k s_k^n(\boldsymbol{x}) \cdot \delta d_k \right) \right\|_2^2 \tag{4.30}$$

The vector minimizing (4.27), noted $\boldsymbol{\delta d}^*$, is

$$\boldsymbol{\delta d}^* = \boldsymbol{H}^{-1}\, \boldsymbol{b} \tag{4.31}$$

where the matrix $\boldsymbol{H} = (H_{ij})$, the Hessian of Ψ_{lin}, and the vector $\boldsymbol{b} = (b_k)$ are given by

$$H_{ij} = \sum_n \sum_{\boldsymbol{x}} \frac{1}{V^n(\boldsymbol{x})}\, s_i^n(\boldsymbol{x})\, s_j^n(\boldsymbol{x}) \tag{4.32}$$

$$b_k = \sum_n \sum_{\boldsymbol{x}} \frac{1}{V^n(\boldsymbol{x})}\, s_k^n(\boldsymbol{x})\, \rho^n(\boldsymbol{x}) \tag{4.33}$$

This approach converges towards the minimum of the cost function (4.26), leading to the identification of the sought vector of transformation parameters $\boldsymbol{d}$. The analysis of the uncertainties in the computed optimal parameters is an indicator of their reliability and is used to assess the quality of the registration. Assuming that the residuals $\rho^n(\boldsymbol{x})$ at convergence mostly contains noise $\eta^n(\boldsymbol{x})$, these uncertainties are extracted from the registration procedure. The uncertainties associated with the estimates δd_i together with their correlations are given by the covariance matrix $\mathrm{C}_{ij} = \langle \delta d_i\ \delta d_j \rangle$

$$\langle \delta d_i\ \delta d_j \rangle = \sum_{k,l} H_{ik}^{-1} H_{lj}^{-1} \sum_{n,m} \sum_{\boldsymbol{x},\boldsymbol{y}} s_k^n(\boldsymbol{x})\ s_l^m(\boldsymbol{y}) \left\langle \frac{\eta^n(\boldsymbol{x})}{V^n(\boldsymbol{x})}\ \frac{\eta^m(\boldsymbol{y})}{V^m(\boldsymbol{y})} \right\rangle \tag{4.34}$$

The noise is considered to be Gaussian and white (spatially and temporally uncorrelated), see Chapter 2, such that

$$\langle \eta^n(\boldsymbol{x})\ \eta^m(\boldsymbol{y}) \rangle = \delta_{nm}\, \delta_{\boldsymbol{xy}}\, V^n(\boldsymbol{x}) \tag{4.35}$$

where $\delta_{..}$ denotes the Kronecker symbol. Using the previous expression, eq. (4.34) reads

$$\mathrm{C}_{ij} = \langle \delta d_i\ \delta d_j \rangle = H_{ij}^{-1} \implies \mathbf{C} = \boldsymbol{H}^{-1} \tag{4.36}$$

The associated correlation matrix $\mathbf{R}$ is defined as

$$\mathrm{R}_{ij} = \frac{\mathrm{C}_{ij}}{\sqrt{\mathrm{C}_{ii}\, \mathrm{C}_{jj}}} \tag{4.37}$$

Complementary notes

Considering a white noise $\eta^n(\boldsymbol{x})$ (spatially and temporally uncorrelated) with variance $V^n(\boldsymbol{x})$, the probability of obtaining a projection residual $\rho^n_{\boldsymbol{d}}(\boldsymbol{x}) := P^n_{\mathrm{a}}(\boldsymbol{x}) - \Pi^n[M(\boldsymbol{d})](\boldsymbol{x})$ is given by the likelihood function

$$\begin{aligned}
\mathbb{P}(\rho^n_{\boldsymbol{d}}) &:= \prod_{\boldsymbol{x}} \mathbb{P}(\rho^n_{\boldsymbol{d}}(\boldsymbol{x})) \\
&= \prod_{\boldsymbol{x}} \frac{1}{\sqrt{2\pi\, V^n(\boldsymbol{x})}} \exp\left(-\frac{[\rho^n_{\boldsymbol{d}}(\boldsymbol{x})]^2}{2V^n(\boldsymbol{x})}\right) \\
&= \left[\frac{1}{\sqrt{2\pi}}\right]^{N_{\boldsymbol{x}}} \left[\prod_{\boldsymbol{x}} \frac{1}{\sqrt{V^n(\boldsymbol{x})}}\right] \left[\exp\left(-\sum_{\boldsymbol{x}} \frac{[\rho^n_{\boldsymbol{d}}(\boldsymbol{x})]^2}{2V^n(\boldsymbol{x})}\right)\right]
\end{aligned} \tag{4.38}$$

with $N_{\boldsymbol{x}}$ the number of pixel. The associated log-likelihood is

$$\begin{aligned}
\mathcal{L}^n(\boldsymbol{d}) &:= \ln\left(\mathbb{P}(\rho^n_{\boldsymbol{d}})\right) \\
&= \ln\left(\left[\frac{1}{\sqrt{2\pi}}\right]^{N_{\boldsymbol{x}}} \left[\prod_{\boldsymbol{x}} \frac{1}{\sqrt{V^n(\boldsymbol{x})}}\right] \left[\exp\left(-\sum_{\boldsymbol{x}} \frac{[\rho^n_{\boldsymbol{d}}(\boldsymbol{x})]^2}{2V^n(\boldsymbol{x})}\right)\right]\right) \\
&= -\frac{1}{2} N_{\boldsymbol{x}} \ln(2\pi) + \sum_{\boldsymbol{x}} \ln\left(\frac{1}{\sqrt{V^n(\boldsymbol{x})}}\right) - \sum_{\boldsymbol{x}} \frac{[\rho^n_{\boldsymbol{d}}(\boldsymbol{x})]^2}{2V^n(\boldsymbol{x})} \\
&= -\frac{1}{2}\left(N_{\boldsymbol{x}} \ln(2\pi) + \sum_{\boldsymbol{x}} \ln(V^n(\boldsymbol{x})) + \sum_{\boldsymbol{x}} \frac{[\rho^n_{\boldsymbol{d}}(\boldsymbol{x})]^2}{V^n(\boldsymbol{x})}\right)
\end{aligned} \tag{4.39}$$

Hence

$$\begin{aligned}
\arg\max_{\boldsymbol{d}} \mathcal{L}^n(\boldsymbol{d}) &= \arg\min_{\boldsymbol{d}} \left(N_{\boldsymbol{x}} \ln(2\pi) + \sum_{\boldsymbol{x}} \ln(V^n(\boldsymbol{x})) + \sum_{\boldsymbol{x}} \frac{[\rho^n_{\boldsymbol{d}}(\boldsymbol{x})]^2}{V^n(\boldsymbol{x})}\right) \\
&= \arg\min_{\boldsymbol{d}} \sum_{\boldsymbol{x}} \frac{[\rho^n_{\boldsymbol{d}}(\boldsymbol{x})]^2}{V^n(\boldsymbol{x})} \\
&= \arg\min_{\boldsymbol{d}} \left\| \frac{1}{\sqrt{V^n(\boldsymbol{x})}} \rho^n_{\boldsymbol{d}}(\boldsymbol{x}) \right\|_2^2
\end{aligned} \tag{4.40}$$

The above quadratic norm corresponds to the cost function Ψ introduced in eq. (4.26), for a single view indexed by n.

4.2.3 Deformable model of a turbine blade

To best capture the shape of the part, it is necessary to consider a deformable model M describing the expected shape variability. If the chosen deformable model provides a large flexibility, it will involve many degrees of freedom, at the risk of rendering the registration procedure ill-conditioned or even ill-posed. The deformable model thus needs to contain a reasonable number of parameters while describing the desired range of shapes. A deformable model derived from the *a priori* information

on the manufacturing process is ideal to mitigate the lack of information due to the limited number of views.

The internal air cooling cavity of a turbine blade describing the internal structure is manufactured by an investment casting process. A ceramic core reproducing the shape of the desired cavity is positioned in the injection mold, known as *master die*. A slight misalignment of the core results in thinner or thicker walls in different regions of the blade compared to its ideal CAD model. Moreover, the core and master die may expand or shrink during the manufacturing process due to thermal constraints, which leads to thickness differences with the blade CAD model. Another potential source of thickness variation is a manufacturing defect in the core or in the master die themselves. However, they are considered negligible as compared to those induced by the core misalignment.

This manufacturing process may be exploited to generate the deformable model. The model M consists in the partition of the part into two main subparts: the master die and the core. The shape of the core is then extracted from the master die (see Figure 4.1). This model can be enriched depending on the structure or the manufacturing process of the core, for instance by further dividing the core into subparts. In this study, the core has been partitioned into five subparts, as illustrated in Figure 4.1 (middle). Each subpart indexed by k is associated with a transformation denoted τ_k that maps the model of the corresponding subpart into the corrected one. To correctly interpret transformations, they need to be expressed in the same frame of reference, for instance, that of the ideal part CAD model. A corrected model is obtained by applying the transformations τ_k to each subpart.

The kinematics of the subparts that define a simple yet representative deformable model is given by a rigid body motion of the independent subpart k parametrized by $(\boldsymbol{t}_k, \boldsymbol{\alpha}_k)$. $\boldsymbol{t}_k$ denotes the translation vector of the k^{th} subpart, and $\boldsymbol{\alpha}_k$ its rotation with respect to the center of the bounding box surrounding the initial master die (black point on Figure 4.1 (right)) which coincides with the origin $\boldsymbol{O}$ of the coordinate system of reference. To account for thermal shrinkage/dilatation of the core, an additional scale factor s affecting all subparts of the core is introduced. This representation assumes that the geometry of each individual subpart perfectly matches its CAD model without deformation of its surface. This parametric deformable model of the turbine blade takes advantage of information about the manufacturing process, and is well suited for NDE. Moreover, the parametric representation of the corrected model allows for a direct interpretation of the origin of possible deviations from the conceived nominal model, and hence it provides insights about the manufacturing process itself and keys for correcting it.

The estimation of the parameters s and $(\boldsymbol{t}_k, \boldsymbol{\alpha}_k)$ is achieved following the procedure described in Algorithm 3. The parameters are initialized from the ideal design of the core and of the master die. The convergence criterion is based on the norm of the residuals after each iteration.

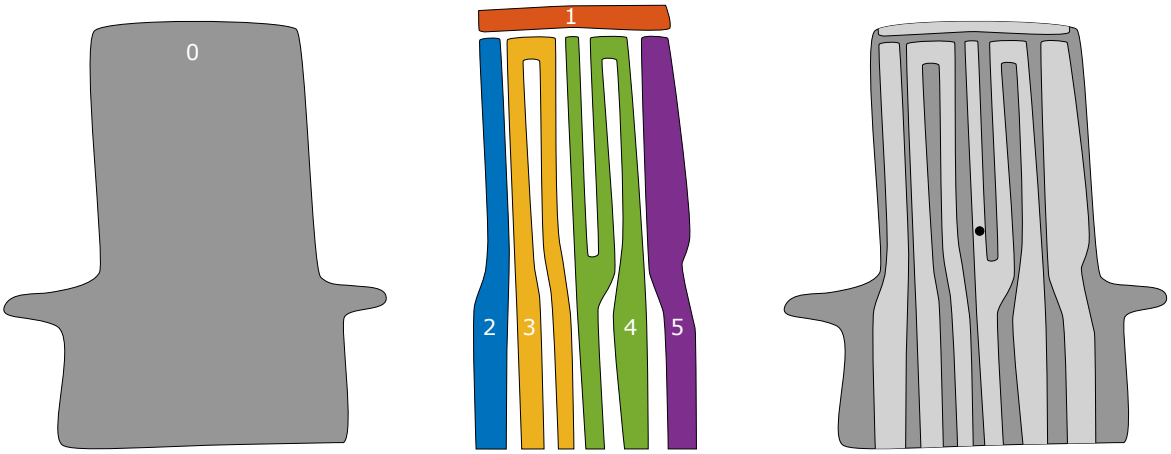

Figure 4.1: Illustration of the part divided into six subparts: the master die (left) and five subparts of the core (middle); and their association (right).

Algorithm 3: Iterative registration procedure

Input: Meshes of each subpart, Initial estimates of parameters $\boldsymbol{\mathcal{T}}_c := (s, \boldsymbol{t}_1, \ldots, \boldsymbol{\alpha}_5)$ and $\boldsymbol{\mathcal{T}}_0 := (\boldsymbol{t}_0, \boldsymbol{\alpha}_0)$

Output: Optimal values $\boldsymbol{\mathcal{T}}_c^* = (s^*, \boldsymbol{t}_1^*, \ldots, \boldsymbol{\alpha}_5^*)$ and $\boldsymbol{\mathcal{T}}_0^* = (\boldsymbol{t}_0^*, \boldsymbol{\alpha}_0^*)$

Load meshes;

do

  for $k \leftarrow 0$ **to** 5 **do**

    Apply the transformation τ_k to the corresponding mesh of the k^{th} subpart;

  Compute the sensitivity fields for $\boldsymbol{\mathcal{T}}_c$;

  Compute the sensitivity fields for $\boldsymbol{\mathcal{T}}_0$;

  Compute $\boldsymbol{\delta\mathcal{T}}_c^*$ using (4.31) from the sensitivity fields computed at lines 3;

  Compute $\boldsymbol{\delta\mathcal{T}}_0^*$ using (4.31) from the sensitivity fields computed at line 3;

  Update $\boldsymbol{\mathcal{T}}_c \leftarrow \boldsymbol{\mathcal{T}}_c + \boldsymbol{\delta\mathcal{T}}_c^*$ and $\boldsymbol{\mathcal{T}}_0 \leftarrow \boldsymbol{\mathcal{T}}_0 + \boldsymbol{\delta\mathcal{T}}_0^*$;

while *Convergence criterion reached*;

4.2.4 Repeatability study

A repeatability study was performed to assess the stability of the method and to evaluate the ability of the deformable model to cope with different parts. Indeed, the acquisition of X-ray images to control a part involves the manual positioning of the sample in the acquisition system which induces human variability. In practice, each control is then realized with a set of (slightly) different viewpoints. Because of their limited number, these viewpoints would contribute greatly to the determination of the transformations τ_k. To eliminate the dependence on the sample positioning in the acquisition system, the transformation τ_0^{-1} is to be applied to the computed corrected model. The idea behind this is to capture the *relative* motion of the core with respect to the master die, which fully determines the wall thickness. It also allows the computation of wall thicknesses in the same reference frame for all samples. This amounts to only applying the relative transformations $\tau_k^0 := \tau_0^{-1}\tau_k$, $k > 0$ to each

subpart of the core. Although it theoretically solves the issue, it is essential for the reliability of the NDE procedure to validate this point.

During the repeatability study, X-ray images of six metallic turbine blades, selected so that they cover or exceed the tolerance interval for the wall thickness measurements, were acquired nine times each. The inspected turbine blades are referred to as samples in the following. The images were acquired with the XT H 450 system developed by Nikon Metrology at the Safran Advanced Turbine Airfoils (PFX) research center; the acquisition parameters are listed in Table 4.1. During acquisition, the sample was manually positioned in the acquisition system and rotated by intervals of 30°, leading to a total of $N = 12$ projections. The procedure was reproduced for all six samples and all nine repetitions.

For each batch of observed radiographs, the above described parametric deformable model was fitted using Algorithm 3 to generate a corrected model. Wall thickness was measured for 80 points in the airfoil, as mentioned in Section 4.2.1, using an automatic routine. Surfaces $\mathcal{S}_1$ and $\mathcal{S}_2$ introduced in eq. (4.1) correspond in practice to sub-surfaces around these measurement points. These sub-surfaces contain between 10 and 30 points each.

For each sample, nine sets of optimal transformation parameters were identified, one for each batch of images. A reasonable assumption of a Gaussian dispersion of the nine batches of transformation parameters allows the uncertainties on the measurements to be computed. This assumption was verified using Shapiro-Wilk normality test [17].

Acceleration voltage	400 kV	Frames per projection	32
Tube current	500 μA	Size of images	2000×2000 pixels
Pre-filtering	4 mm of copper	Voxel size (spatial resolution)	50.55 μm
Exposure time	354 ms	Encoding	16-bit uint

Table 4.1: Parameters for X-ray image acquisition using an XT H 450 (Nikon Metrology).

4.3 Results and discussion

Each identified relative transformation τ_k^0 is a combination of a scaling by a factor s, a translation $\boldsymbol{T}_k$ and a rotation specified by Euler angles $\boldsymbol{\theta}_k$. For every sample, the average values of the associated estimates over the 9 sets are presented in Figure 4.2.

Figure 4.2 suggests that the transformation parameters show some variability among the different samples. This observation is due to the selection of the parts such that they would represent the production operating range. In this sense, Figure 4.2 shows the ability of the registration procedure to handle parts that have the same ideal design but whose actual geometry differs due to production variability. In addition, considering that the transformation parameters are noticeable, it confirms to the necessity of taking into account the transformation of the core to perform accurate measurements of wall thicknesses. The large variability of the translation vectors $\boldsymbol{T}_1$ and $\boldsymbol{T}_5$ is due to the choice of the point about which rotations are computed. For rigid body motions, translations are not intrinsic as they depend on the chosen point

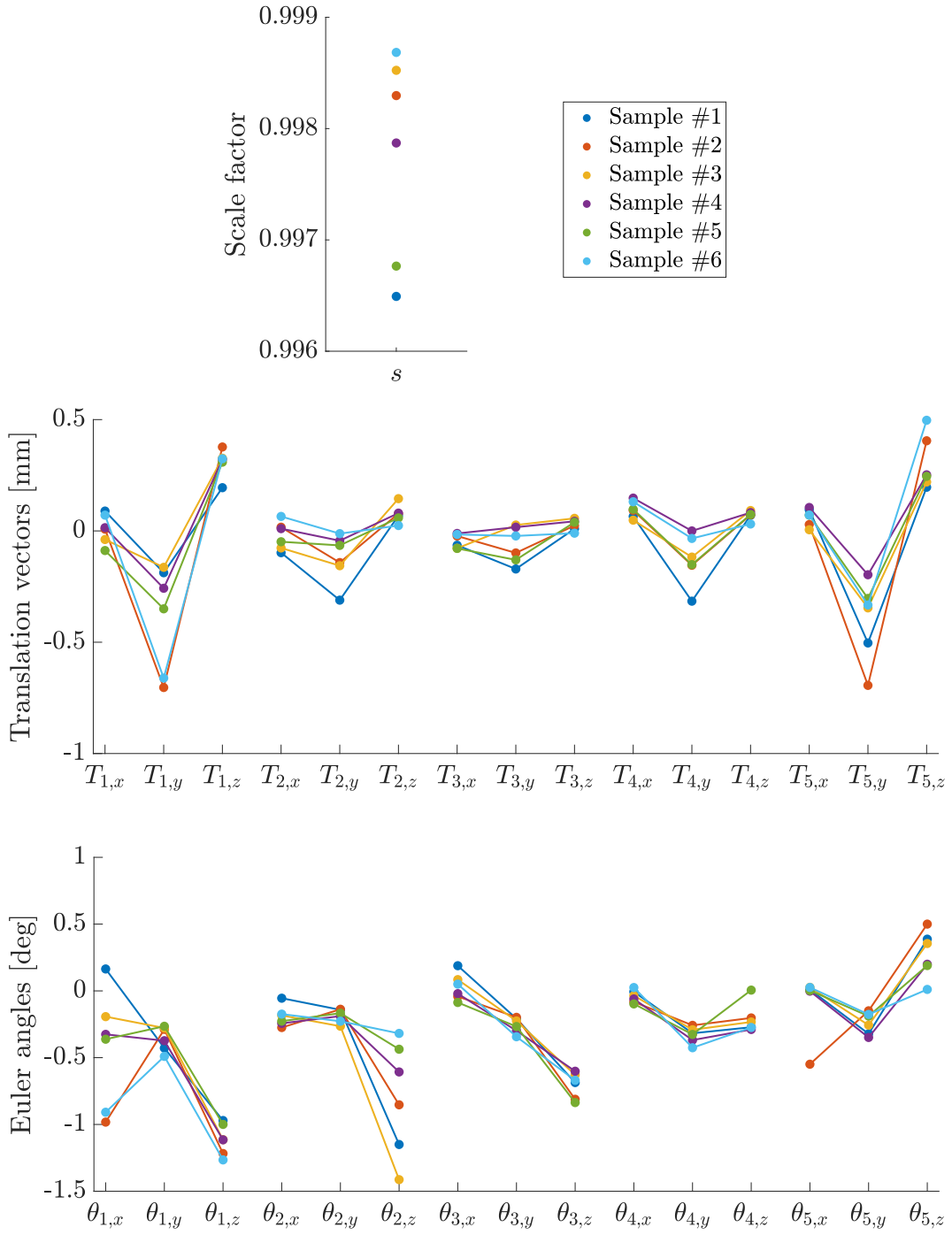

Figure 4.2: Average values of the transformation parameters for all samples: scale factor s (top), components of the translation vectors $\boldsymbol{T}_k$ (middle), Euler angles $\boldsymbol{\theta}_k$ (bottom).

of rotation (*cf.* subsection 4.2.1.1). As seen in Figure 4.1, subpart 1 (red) is far from the center of rotation (black). The curved nature of the blade, not visible in Figure 4.1, leads to the same conclusion for subpart 5 (purple).

In the following, results will be presented for the sample number 1 as conclusions are similar for all samples. The variability of the identified transformation parameters over the 9 sets is presented in Figure 4.3. Values have been centered around their median m to better visualize their spread. The figure shows that the variability of the

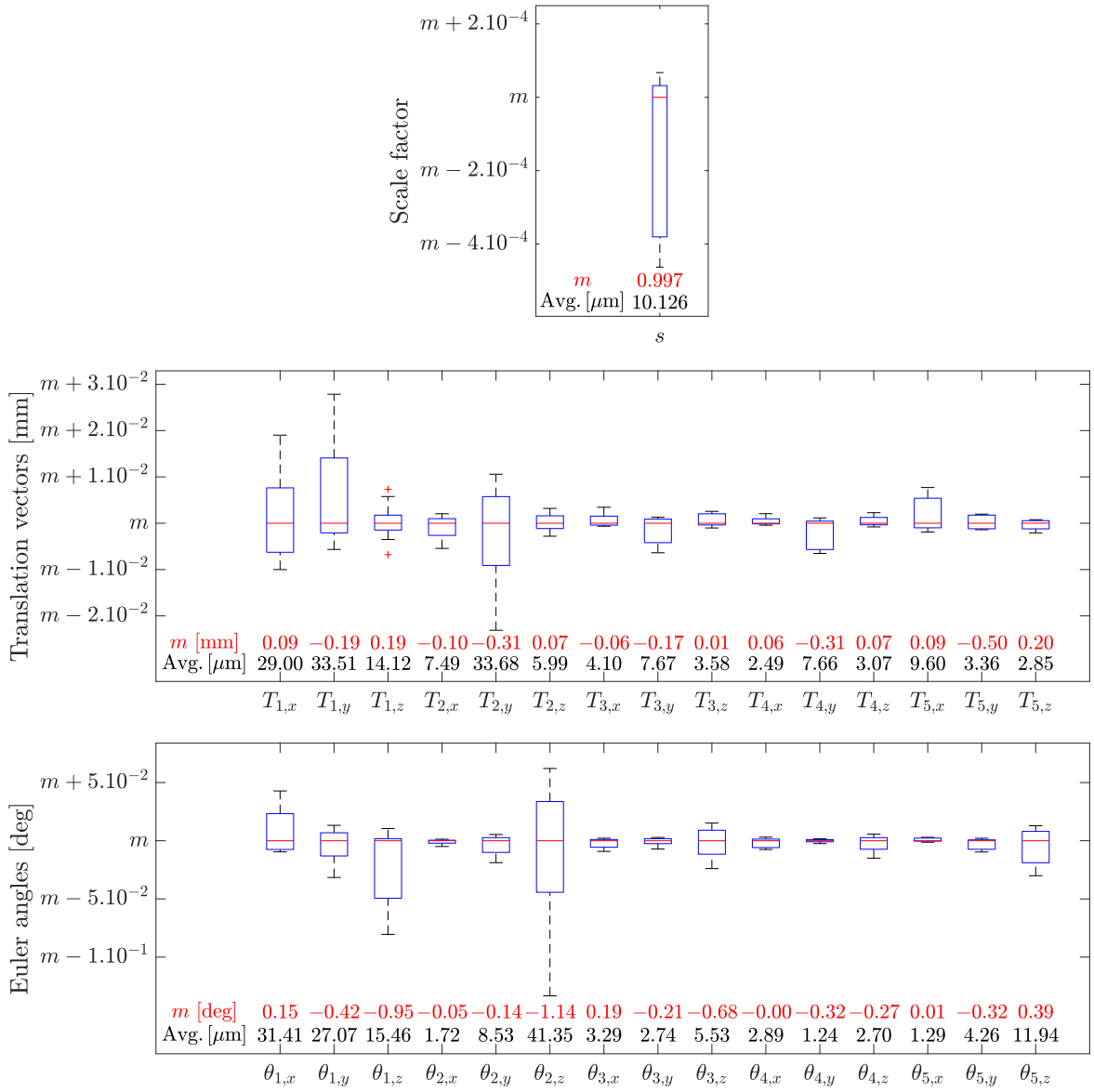

Figure 4.3: Boxplots showing the variability of the identified optimal transformation parameters over 9 repetitions for sample number 1. Values have been centered around their median m to better visualize their spread. Below each box, the median value (red) and the average magnitude (in μm) of the displacements associated with the observed variabilities (black) are presented.

transformation parameters are much smaller than the variability between samples: in the range of 10^{-3} for the scale factor, 35 μm for the translations parameters, and 0.2°

for the Euler angles. To properly interpret theses values, the displacements associated with these variabilities need to be computed and compared to the voxel size which is here 50.55 μm. Thus, for each parameter, two transformations are considered: one using the lowest identified value, the other with the highest (the values of the other parameters correspond to their medians). These transformations are applied to the initial model, and the magnitude of the displacement between the two transformed models is computed at each node. For the rotation and translation parameters, this magnitude is averaged over the associated subpart; and for the scale factor, over the entire core. These values, expressed in μm, are reported below each box of Figure 4.3, in black (second line). A sub-voxel accuracy is observed for all the parameters. The parameter $\theta_{2,z}$, for which the sub-voxel accuracy is barely met, exhibits the largest variability, and thus uncertainty. $\theta_{2,z}$ represents a rotation of the 2$^{\text{nd}}$ subpart, shown in blue in Figure 4.1, around the Z axis. This can be explained by the cylindrical shape of the subpart with a small radius of gyration and an axis that almost coincides with the Z axis. As a consequence, even a large angle variation induces only a minute displacement along the core boundary.

Using equation (4.36), the covariance matrices $\mathbf{C}$ are computed. An example of such a matrix is displayed in Figure 4.4, together with the associated correlation matrix $\mathbf{R}$.

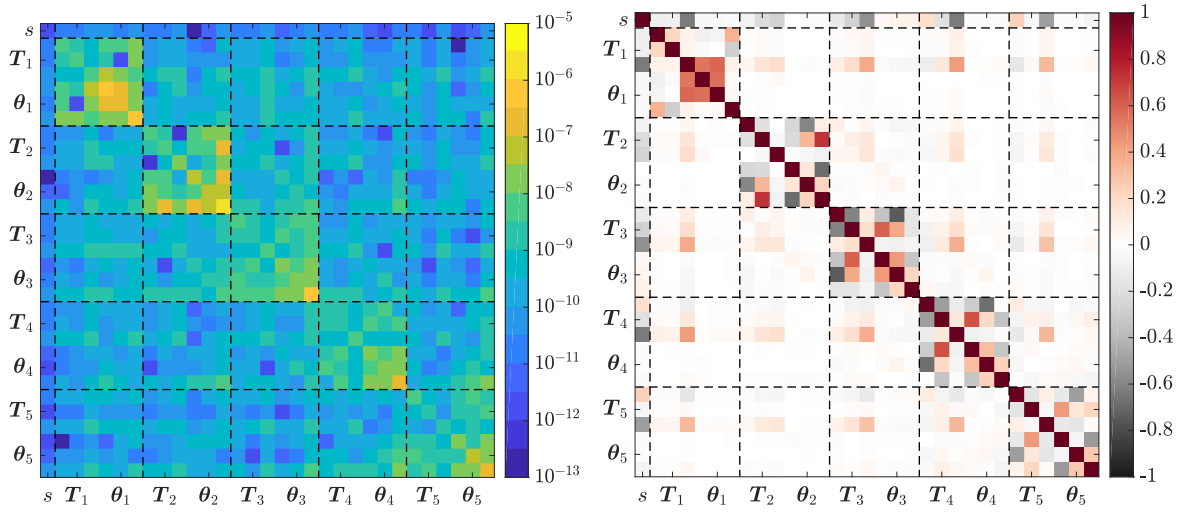

Figure 4.4: Element-wise absolute value of the covariance matrix $\mathbf{C}$ (left, logarithmic scale) and correlation matrix $\mathbf{R}$ (right) computed at convergence. Black dotted lines are plotted to better visualize the different subparts.

By definition, the diagonal terms of the correlation matrix $\mathbf{R}$ are equal to 1. Non-diagonal terms, which range from -1 to 1, represent the degree of correlation between a pair of parameters. As expected, parameters associated with distinct subparts are weakly correlated (less than 0.5). The scale factor s is mostly (negatively) correlated to the translation parameter along the main orientation of the subpart, as a result of its slenderness.

Figure 4.5 displays projection residuals with the initial (top) and optimal (bottom) transformation parameters, focusing on four areas of interest. Residual values are

expressed as a percentage of the dynamic range of the observed projections. The higher level of residuals in the root of the turbine blade, panel (a), is explained by the fact that some phenomena, particularly visible for high thicknesses, were not included in the projection operator Π^n. It should however be noted that this imperfection in the projection operator is small as it represents at most, in the thickest area, a 5.6% deviation from the gray levels of the observed projections. In the top row, the observed residuals are mainly due to the deviation of the core from its ideal design, as shown for instance in panel (c) where a structure with positive residuals on the left and negative on the right is visible. Similar structures are apparent on the other panels. These deviations may be accounted for by the introduced degrees of freedom. Thus, in the bottom row, the above described structure visible on panel (c) is highly reduced, as well as for the other panels. The procedure leads to the estimates of the

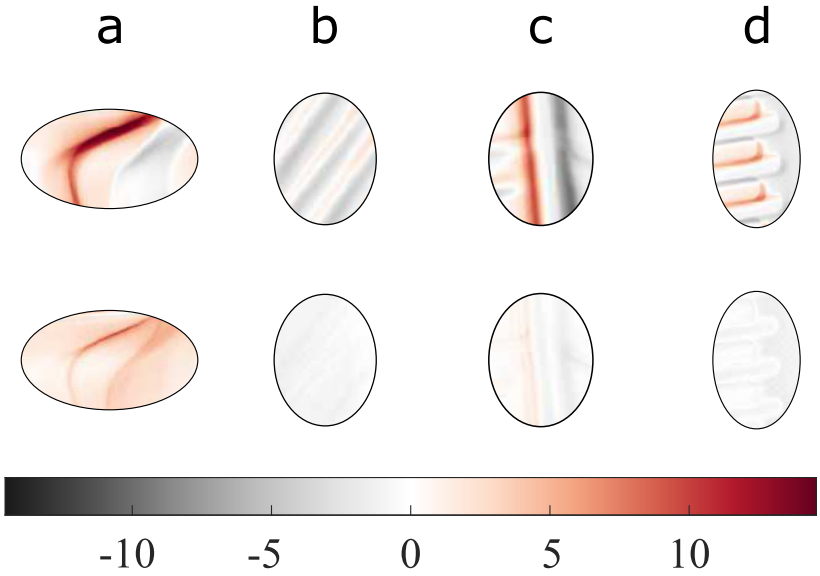

Figure 4.5: Difference (color) between acquired and simulated projections, before (top) and after (bottom) identification of the transformation parameters. The different panels show: (a) a curved region in the root of the turbine blade, (b) an internal structure, known as a rib structure, in the airfoil, (c) a wall of an internal cavity, (d) slots on the trailing edge of the blade. Values are expressed as a percentage of the observed projections dynamic range.

best transformation parameters considering the proposed parametrization.

The transformed CAD models are compared to the ground truth given by a tomographic volume, also called tomogram, reconstructed from a set of 3000 radiographs. Figure 4.6 displays the tomogram (gray) with the initial CAD model (orange) and corrected ones (different shades of blue are used for all 9 estimates). The blue surfaces are barely distinguishable from each other, which confirms the high similarity between the identified sets of transformation parameters. It can be seen that the blue surfaces line up more tightly with the boundaries of the tomogram than those of the initial CAD model. Discrepancies are observed for the cavity in view (a) or the rib in view (c) which appears shifted. As displayed in Figure 4.6, these areas are characterized by a high curvature of the surfaces. These incorrect positionings seem to be large,

however, the surfaces of these cavities are inclined at a low angle with respect to the section planes. It thus corresponds in 3D to an offset between the surfaces of a very few voxels, namely one or two. Despite the number of radiographs used being reduced by a factor of almost 300, the agreement between the corrected model and the tomogram when the curvature is low is outstanding.

However, some remaining deviations are observed. In view (c), the CAD design displays sharp corners, whereas the ones in the manufactured part are smoother. This discrepancy can be explained by the effect of the sintering of the mold or the surface tension between the metal and the core during the metal casting. As these phenomena are not described in the deformable model, such deviations cannot be resolved.

Thus, even with (hopefully localized) model errors, the proposed deformable model explains most of the differences, which renders the correction efficient and operable. In addition, the observed differences between the part and its CAD model in highly curved regions points towards considering other deviations from the original CAD model, namely non-rigid shape deformations. These deviations may be accounted for by resorting to a more flexible deformable model, for instance, an additional correction model acting at a more local scale. An alternative would be to use a more representative core mesh obtained from actual manufactured cores. Such a procedure would allow to distinguish more clearly between systematic shape deviation due to the manufacturing process and intrinsic variability. In the case where the geometry of the subparts are systematically measured in the control chain, *e.g.* by Non-Contact CMM, this approach would allow one to increase the available *a priori* information without increasing the time allocated for the control. A weighting to the surfaces based on their curvature can also be considered to further reduce the weight of these model errors.

Wall thickness have been measured in the airfoil of the 9 corrected models and of the tomogram. As illustrated in Figure 4.6, measurements of the transformed models are similar, so that only the average values of the measurements is representative of further data acquisition and processing. Figure 4.7 (top) shows a Bland-Altman plot [18] to illustrate the disagreement between the two measurement methods (corrected models and tomogram). The bias of 26.6 μm indicates the average difference between the two measurement methods. This discrepancy represents slightly more than *half a voxel*, showing the high accuracy of the proposed approach. The limits of agreement, which indicate the precision of the measuring system, are to be compared to the tolerance values defined in the part specification. In the case of aeronautical parts for which dimensional compliances are very stringent, this large interval of ≈ 196 μm does not meet the technical requirements. It should however be noted that a less constrained parametrization of the shape would be likely to yield a transformed model closer to reality and thus more accurate measurements. In comparison, the same measurements have been performed on the untransformed model, see Figure 4.7 bottom. Using the proposed approach, the bias is increased by a slight amount (15 μm), while the limits of agreement are significantly reduced (185 μm).

The computation of measurement uncertainties based on the covariance matrix $\mathbf{C}$ produced estimates of the order of a few hundred nanometers, which is significantly lower than the uncertainty values obtained by repeating the same control several times. The formula (4.34) used for the computation of $\mathbf{C}$ relies on the assumption that the

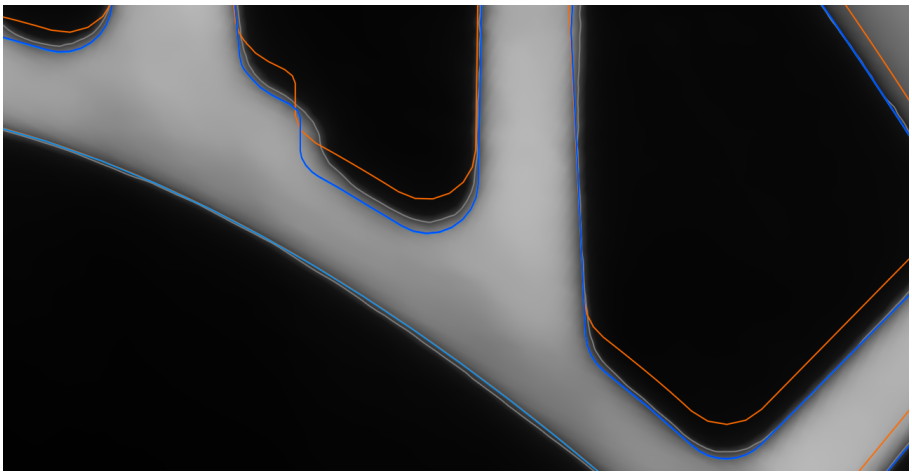

(a)

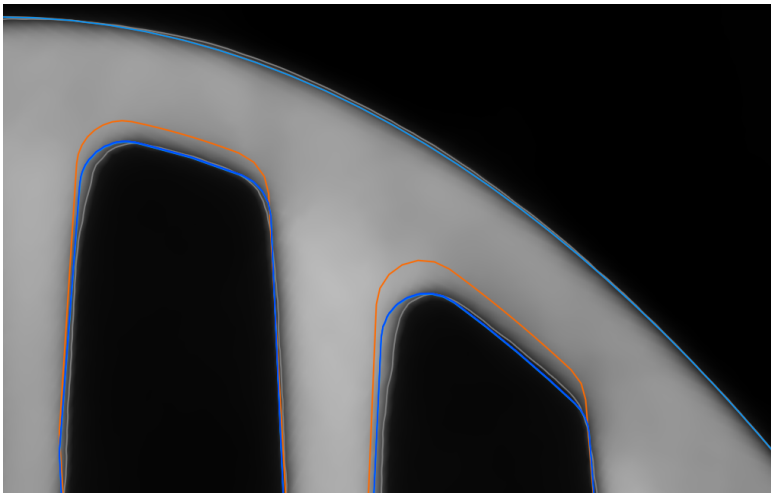

(b)

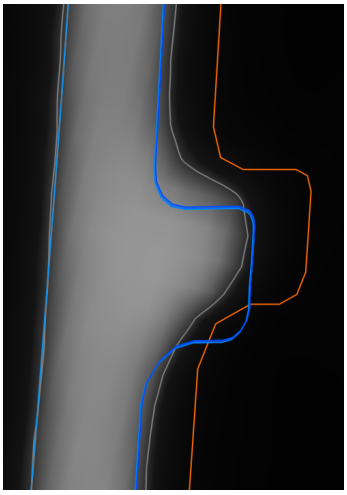

(c)

Figure 4.6: Superimposition of the ideal (orange) and transformed (shades of blue) designs of the core over the tomogram (gray).

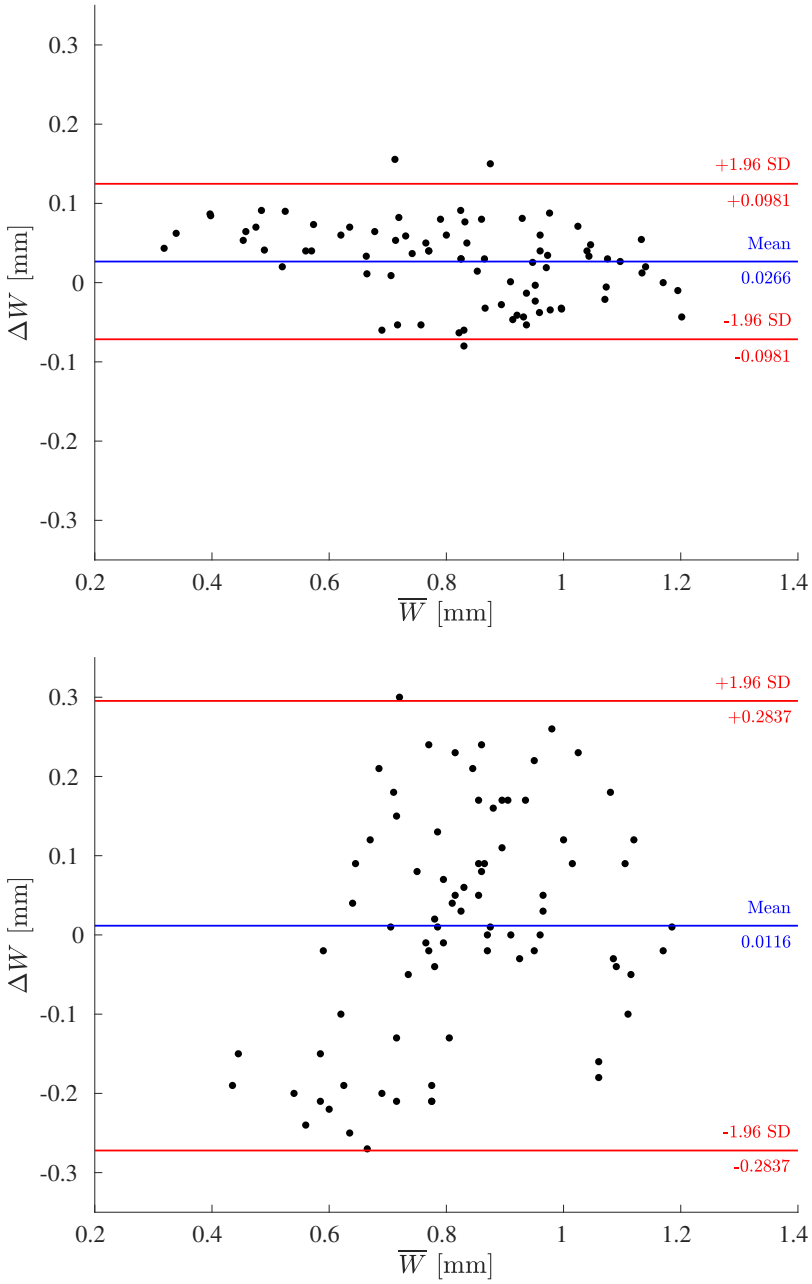

Figure 4.7: Bland-Altman plot of wall thickness measurements by the proposed model and by X-ray CT tomography. The plot displays the difference ΔW as a function of the mean value $\overline{W}$ of measurements using the corrected (top) and initial (bottom) models. The mean of the differences (blue line) indicates the bias between the values obtained from the two measurement methods. The limits of agreement (red lines) delineate the interval where 95% of the differences are expected to lie.

residual ρ^n mostly contains noise η^n. For this assumption to be verified, it is necessary to have a transformed model that exactly matches the imaged part and a perfect projection operator. From the previous results, it appears that these two conditions are not met. Figure 4.6 displays differences in geometry between the estimated model and the ground truth, mainly because the non-rigid deformation of the core is not included in the deformable model. In addition, Figure 4.5 suggests imperfections in the projection operator which, although small, violate the assumption.

The findings of this study do have some limitations. A limitation of the approach is that the proposed deformable model is presumably too simple to account for the exact shape mismatch. Ideally a flexible model would be required, however, an important feature is the parametrization of the considered deformation modes. The ones considered in this work (independent rigid body motions) benefits from a parametrization that is neither too rich (large uncertainty) nor too poor (realism of shape deviations). It is this trade-off that motivated the decision to define the modes as independent rigid body motions. This trade-off leaves a margin of error which leads to residual shape deviations between the transformed model and the tomogram and thus unreliable measurements. To improve the set of transformations one may envision a more flexible deformable model, adding a local correction model, or replacing CAD models of the surfaces with measured ones. Furthermore, projection residuals (above denoted ρ^n) are indicators of the registration quality and thus of the reliability of the computed measurements. They may also be used to identify the most appropriate locations for the measurement points.

It is worth noticing that the images were acquired in a single X-ray cabin (XT H 450), which may constitute a bias in the analysis. Likewise, the procedure was tested on parts of a single type, *i.e.* a single reference of a turbine blade, even if multiple samples were imaged to account for shape variability. It is however expected that similar results would be observed for a different acquisition system or reference of a turbine blade with a comparable manufacturing process as no other assumptions other than the manufacturing process have been made. However, accounting for *e.g.* the panel detector used in the X-ray cabin may enrich the projection operator. From an industrial point of view, endorsing the procedure would require that the same study be performed with multiple parts to ensure that a change in the blade geometry would not lead to inconsistent results. Nevertheless, nothing currently suggests that additional issues are to be encountered.

4.4 Conclusion

In this work, an approach to assess 3D dimensional measurements of complex shape parts from a limited number of 2D X-ray images has been presented. It consists of fitting a parametric model of the imaged part to generate a corrected numerical model. The dimensions to be controlled are measured directly on this corrected model. The selected application case is the control of wall thicknesses of a hollow turbine blade, a part with complex internal geometry. Describing the control principle allowed the definition of guidelines to perform reliable measurements. The optimal transformation parameters of the model are identified by iteratively matching the projections simu-

lated from the transformed model to the observed projections. The parametric model has been developed in line with the manufacturing process. It relies on the partition of the part into multiple subparts: one representing the external surface, five representing the various element of the inner ceramic core describing the internal geometry. The kinematics of each subpart is a rigid-body motion, plus a scale factor to account for thermal constraints experienced by the ceramic core during metal casting. This sparse model mimics what occurs during manufacturing and thus provides a fair description of the expected shape variabilities. In addition, the observed transformations can be further exploited to improve the manufacturing process and reduce the range of shape deviations.

The reliability of the approach was verified *via* a repeatability study where only a slight discrepancy in the identified parameters, and thus in the associated corrected models, was observed. Furthermore, the agreement between measurements computed from the transformed models and reference values computed from a tomogram demonstrated the approach performance. Discrepancies are mostly explained by the non-rigid shape deformations not considered in the simple deformable model proposed here. These discrepancies, although small, do not comply with the very demanding requirements for NDE of turbine blades. Suggestions to mitigate the discrepancy are proposed and include the use of measured surfaces, or the introduction of a more flexible deformable model.

It is worth emphasizing that the proposed methodology has been designed to minimize the acquisition noise error, as expressed in eq. (4.26). This error is currently much lower than other elements of uncertainty and as a consequence, the method leads to an over-quality. One can consider faster, therefore noisier, acquisitions while still remaining below the uncertainties due to other factors.

Acknowledgement

This work was supported by the French "Association Nationale de la Recherche et de la Technologie" (CIFRE n° 2019/0793). The first and second authors would like to thank Mr. Omer Unlu and Mr. Pierre-Luc Patard for their implication in the experimental phase. The authors would like to thank Ms. Tonya Rose from the Digital Sciences and Technologies Department at Safran Tech for her insightful suggestions on the manuscript.

Bibliography

[1] Clemens Buske, Alexander Krumme, Thomas Schmidt, Christian Dresbach, Sascha Zur, and Rüdiger Tiefers. Distributed Multidisciplinary Optimization of a Turbine Blade Regarding Performance, Reliability and Castability. In *Turbo Expo: Power for Land, Sea, and Air*, volume 49712. American Society of Mechanical Engineers Digital Collection, 2016.

[2] Mathias Luers, Max Sagebaum, Sebastian Mann, Jan Backhaus, David Grossmann, and Nicolas R. Gauger. Adjoint-based Volumetric Shape Optimization of Turbine Blades. In *2018 Multidisciplinary Analysis and Optimization Conference*. American Institute of Aeronautics and Astronautics, 2018.

[3] Jiaqi Luo and Yao Zheng. Aerodynamic Shape Optimization of a Turbine Blade Considering Geometric Uncertainty Using an Adjoint Method. In *Turbo Expo: Power for Land, Sea, and Air*, volume 58578. American Society of Mechanical Engineers Digital Collection, 2019.

[4] Chun-Yi Zhang, Ze Wang, Cheng-Wei Fei, Zhe-Shan Yuan, Jing-Shan Wei, and Wen-Zhong Tang. Fuzzy Multi-SVR Learning Model for Reliability-Based Design Optimization of Turbine Blades. *Materials*, 12(15):2341, 2019.

[5] S. Dhivya and A. Karthikeyan. Design and Analysis of Gas Turbine Blade with Cooling. *EAI Endorsed Transactions on Energy Web*, 5(20), 2018.

[6] Mohammed Aljibory, Farhan Lafta, and Hasan Qahtan. Review Of Heat Transfer Enhancement In Air-Cooled TurbineBlades. *International Journal of Scientific & Technology Research*, 9:3123–3130, 2020.

[7] Farah Nazifa Nourin and Ryoichi S. Amano. Review of gas turbine internal cooling improvement technology. *Journal of Energy Resources Technology*, 143(8):080801, 2021.

[8] Jonas Aust and Dirk Pons. Taxonomy of Gas Turbine Blade Defects. *Aerospace*, 6(5):58, 2019. Publisher: Multidisciplinary Digital Publishing Institute.

[9] Robert J. Hocken and Paulo H. Pereira. *Coordinate measuring machines and systems*, volume 6. CRC press Boca Raton, FL, 2012.

[10] Grzegorz Budzik. Geometrical accuracy of aircraft engine turbine blades. *Oficyna Wydawnicza Politechniki Rzeszowskiej, Rzeszów*, 2013.

[11] Radosław Przysowa, Marek Chalimoniuk, Danuta Grzelka-Gajek, Ruslan Shakalo, and Artem Karpenko. CT Inspection of Cooled Turbine Blades. *Journal of KONBiN*, 50(3):307–331, 2020.

[12] Józef Błachnio, Marek Chalimoniuk, Artur Kułaszka, Henryk Borowczyk, and Dariusz Zasada. Exemplification of detecting gas turbine blade structure defects using the x-ray computed tomography method. *Aerospace*, 8(4):119, 2021.

[13] Scott Hastie, Anthony Chan, Kevin Wiens, Doug Nagy, Robert Tollett, and Paul Lowden. Computed Tomography Wall Thickness Inspection to Support Gas Turbine Blade Life Extension. In *Turbo Expo: Power for Land, Sea, and Air*. American Society of Mechanical Engineers Digital Collection, 2021.

[14] Wim Van Aarle, Willem Jan Palenstijn, Jeroen Cant, Eline Janssens, Folkert Bleichrodt, Andrei Dabravolski, Jan De Beenhouwer, Kees Joost Batenburg, and Jan Sijbers. Fast and flexible X-ray tomography using the ASTRA toolbox. *Optics express*, 24(22):25129–25147, 2016. Publisher: Optical Society of America.

[15] Cédric Fragnaud, Clément Remacha, Julián Betancur, and Stéphane Roux. CAD-based X-ray CT calibration and error compensation. *Measurement Science and Technology*, 33(6):065024, 2022.

[16] Fedor Menas'evich Dimentberg. *The Screw Calculus and Its Applications in Mechanics*. Air Force Systems Command. FTD, Foreign Technology Division. Foreign Technology Division, WP-AFB, 1968.

[17] Samuel Sanford Shapiro and Martin Bradbury Wilk. An analysis of variance test for normality (complete samples). *Biometrika*, 52(3/4):591–611, 1965.

[18] John Martin Bland and Douglas Graham Altman. Statistical methods for assessing agreement between two methods of clinical measurement. *The lancet*, 327(8476):307–310, 1986. Publisher: Elsevier.

Chapter 5

Conclusion and perspectives

This thesis work aimed at developing an NDE process to identify and characterize geometrical imperfections in complex-shaped objects by multi-view X-ray imaging. The process has been designed considering the constraints of industrial production lines of HP turbine blades. The developed approach consisted of producing a 3D model of the inspected part based on the observed images using Projection-based Digital Volume Correlation (P-DVC) [1].

The noise properties investigated in Chapter 2 allowed the definition of an optimal cost function, key element of P-DVC, designed to minimize acquisition noise error. A description of a flat-field image was built by unraveling the contributions of the characteristic elements inherent to the acquisition: temporal fluctuation of the X-ray source and its cone-beam geometry, panel assembly of the detector. It was found that the noise polluting a flat-field image is gaussian and white, with a variance that can be readily estimated.

The quantitative comparison of observed and simulated X-ray images calls for:

- the proper definition of the projection geometry. It corresponds to the numerical positioning of the imaged part with respect to the X-ray cabin components (source, detector) through an appropriate parametrization,
- accounting for the physical phenomena underlying image formation. The phenomena that cause the largest deviation from the (monoenergetic) Beer Lambert's attenuation law are beam hardening (resulting from the polyenergetic nature of the source) and Compton scattering (non-pure attenuation phenomenon). Parametric models have been proposed to describe how these phenomena manifest in the observed images.

These three elements (steps 1-3 represented in Figure 1.8) form a parametric projective model for which optimal parameter values are identified through a calibration procedure relying on P-DVC formulated in Chapter 3 [2]. Once this identification is achieved, the projection residuals obtained using the CAD model of the part point toward shape deviations from the nominal geometry, known as geometrical indications. Discrepancies unrelated to these indications are still observed, indicating that the projection operator is prone to improvements. However, it should be noted that the remaining deficiencies are not limiting for the sought purpose.

Characterizing the indications relies on the estimation of the 3D model of the part being imaged on which measurements can be performed. For this, a deformation model derived from the manufacturing process of the blade has been introduced in Chapter 4 [3]. The numerical model of the part is partitioned into multiple subparts whose relative kinematics is given by an independent rigid body motion. A scale factor is

added to account for thermal shrinkage. The reliability of the deformation estimation approach to measuring the wall thickness of a turbine blade is assessed through a repeatability study. Despite model errors, the corrected model is comparable to the ground truth given by the tomogram. This shape agreement implies similar wall thickness measurements, which may be further refined by addressing model errors (*e.g.* non-rigid deformations).

In this sense, the tools developed during this work and detailed in this dissertation meet the target problem of identifying and characterizing geometrical indications. Further aspects related to the initial question have been investigated and are reported below. These are incomplete ideas, *i.e.* additional developments and tests are necessary for them to be fully effective. In addition, limitations of the procedure are discussed, along with suggestions for improvements and future works.

5.1 Partially investigated work

5.1.1 Local geometrical indications

The HP turbine blades feature cooling holes, manufactured by Electrical Discharge Machining (EDM), to help reduce their temperature. Various controls are performed to ensure the geometry of these holes meets the specifications, which include:

- Diameter measurement: verify that the diameter of the manufactured hole is in the tolerance interval;
- Through-hole nature: control that the hole has been manufactured over 100% of its defined length;
- Position and orientation of the hole axis with respect to the part reference frame: the axes of the manufactured holes may vary depending on the part reference frame. Therefore, measuring the deviation between the theoretical axis and the actual one is necessary.

The NDE procedure formulated in this dissertation and applied to the wall thickness measurement may be adapted to the inspection of cooling holes. Steps 1-3 (Figure 1.8) remain unchanged, but an appropriate deformation model has to be defined. This requires proper modeling of a cooling hole. EDM producing straight holes, a realistic approximation of its geometry is a cylindrical shape, as illustrated in Figure 5.1.

In the (fixed) part reference frame, the axis of the hole is represented by a straight line Δ describing the path of the electrodes, a parametric equation of which being

$$\begin{cases} x = a_x + \alpha_x \, z \\ y = a_y + \alpha_y \, z \\ z = z \end{cases} \tag{5.1}$$

Two remarks are to be made: (i) this parametrization is not universal, *i.e.* another one may be adopted to represent the same axis Δ, (ii) a degeneracy arises when the axis is parallel to the XY plane, an issue called "coordinate singularity". In such a case, this parametrization becomes inadequate, but a mere change of representation

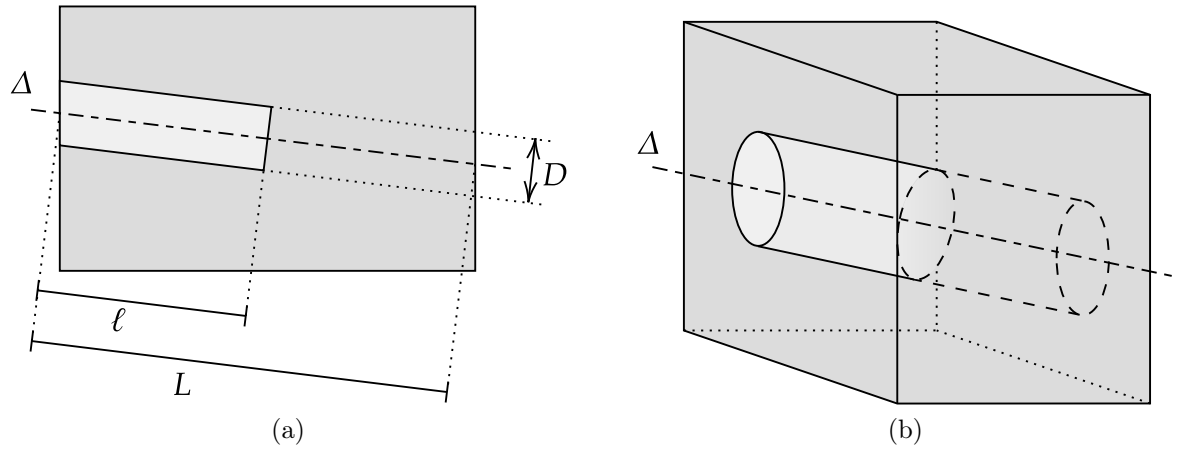

Figure 5.1: Representation of a cooling hole, (a) profile view, (b) section view.

of the axis Δ, for instance

$$\begin{cases} x = a_x + \alpha_x\, y \\ y = y \\ z = a_z + \alpha_z\, y \end{cases} \tag{5.2}$$

eliminates the singularity. This line encodes information regarding the orientation of the hole as well as its position, the latter being specified by a point located at the intersection between Δ and the surface of the part.

The hole is machined over a length $0 < \ell \leq L$, where L denotes the maximum length of the hole given by the wall thickness measured in the direction of Δ. Its diameter is considered constant along Δ, this constraint being automatically satisfied due to the machining process (EDM).

Using this representation, the hole can be described by the following 6 parameters:

- the four parameters of the axis Δ, *e.g.* $(a_x, \alpha_x, a_y, \alpha_y)$;
- the length ℓ;
- the diameter D;

The associated deformation model is obtained by the variation of these parameters. The optimal shape geometry is identified similarly to that detailed in Section 4.2.2.

This approach has been tested on a synthetic case. It yielded very accurate results, better than the required precision (*e.g.* absolute error of 10^{-3} mm in the diameter estimate, and of 6.10^{-3} mm in the parameter a_x). It has yet to be tested on an actual case, *i.e.* real X-ray images of a turbine blade with holes.

It is worth emphasizing that the discussion undertaken in this section illustrates the versatility of the approach. Provided a proper deformation model is established, the approach can be tailored to many applications pertaining to dimensional NDE.

5.1.2 Improved projection views

The identification of the optimal deformation parameters, Section 4.2, has been demonstrated using a set of 12 X-ray images. Projections have been acquired by successively rotating the sample around a fixed axis, with a constant angular spacing of 30° (0°, 30°, 60°, *etc.*). These angles are, however, not necessarily the most appropriate ones to perform the identification. One could even imagine that using a smaller number of views would yield almost identical results. Optimizing the projection views would reduce the time spent on part inspections. It requires (i) a criterion to be minimized or maximized and (ii) an optimization algorithm. Following the formalization introduced and developed in [4], a brief discussion is presented.

Criterion

The parameter identification method detailed in Section 4.2.2 provides uncertainty information regarding the model parameters, from which the uncertainties of dimensional measurements computed on the turbine blade numerical model are derived. Based on these uncertainties, a criterion (cost function) may be proposed whose minimization will lead to the optimized set of projection directions. Two such criteria — which cannot be disclosed for confidentiality — have been investigated.

Optimization algorithm

A greedy approach is proposed to select better-suited projection angles based on these criteria. The angle space is sampled, *e.g.* uniformly, to produce a set of candidate angles $\Theta_c = \left\{\theta_c^1, \ldots, \theta_c^M\right\}$. Starting from the initial configuration $\Theta_a = \left\{\theta_a^1, \ldots, \theta_a^N\right\}$ (12 angles with a constant angular spacing of 30°), it is proposed to iteratively improve it by

- Computing, for each angle θ_a^n in the current configuration and each candidate angle θ_c^m, the criterion where the sensitivity fields associated with θ_a^n are removed and the ones associated with θ_c^m are added;
- Identifying the couple $\left(\theta_a^{n^*}, \theta_c^{m^*}\right)$ that minimizes the criterion;
- Performing the switch, *i.e.* $\theta_c^{m^*}$ is added to the configuration while $\theta_a^{n^*}$ is removed.

In an iterative way, a new and better configuration is built. The decrease in the number of projection views may be achieved by regularly removing $\theta_a^{n^*}$ from the configuration without adding $\theta_c^{m^*}$.

This strategy has been tested to select better-suited angles for inspecting turbine blades. The candidate angles were chosen by sampling at a constant angular spacing of 5°. Both criteria yielded successful results for 12 projections: the volume of the uncertainty ellipsoid was decreased by 29% or by 99% (depending on which of the two criteria is considered), and the largest uncertainty by 21% or by 50%, respectively. Although one would expect the optimal angles to be spread out over the $[0, 2\pi[$ interval, the final configurations show a surprising concentration effect over few angles. Such a result is a promising avenue for future optimization of radiography-based NDE control.

5.2 Perspectives

Future work could provide improvements on the definition of the deformation model, and on the algorithms enabling the estimation of the optimal model parameters for the part being inspected.

5.2.1 Model

As pointed out in Chapters 3 and 4, non-stochastic projection residuals are still visible. These residuals can be attenuated by including other phenomena occurring during the acquisition in the definition of the projection operator, allowing to generate more realistic images. For instance, afterglow may be modeled by a convolution operation of the images in the temporal domain. Another phenomenon to be considered would be the Bragg diffraction that results from the monocrystalline structure of the blade. The crystal orientation may potentially be evaluated. However, it is expected that an accurate model reproducing diffraction would be overly sophisticated for the gain it would provide.

In addition, results of Chapter 4 suggest that non-rigid shape deformations of the surface may be considered to better represent the surface of the blade. Deformation modes derived from mechanical analyses may be envisioned. An example would be to measure the displacement field of the inner ceramic core when subjected to a given load through numerical simulations. Then, a POD or other reduction model methods would allow extracting the dominant deformation modes where the elastic energy is small, defining a mechanical-based deformation model. Other solutions include statistical shape analyses on a set of manufactured blades to obtain a reference shape and the (major modes of) shape variations encoded in the analysis of the deformation to the reference shape.

5.2.2 Procedure speed up

Computation time is currently a limiting factor of the method. The principal bottleneck corresponds to the voxelization step required for computing sensitivity fields. Faster alternatives include implementing the voxelization algorithm in a more efficient programming language (*e.g.* C++) as it is currently implemented in Matlab, or even circumventing this difficulty by using directly the 3D model instead of its voxelized representation. Such a projector has been developed for the ASTRA Toolbox and is presented in [5]. Similarly, other algorithmic aspects of the procedure may be optimized, such as the computation of BH correction function for the simulated images.

5.3 Outlook of NDE

The works reported in this dissertation provide an up-and-coming solution for performing NDE based on a few X-ray images. The method has been applied for detecting dimensional indications, namely wall thickness imperfections. Nevertheless, it is worth emphasizing that its outputs may be exploited to help detect structural indications that falls within the scope of material health inspections. Indeed, final projection residuals might reveal imperfections such as cracks or porosities that may be difficult to detect in raw X-ray images. This would provide alternatives to other

control modalities that are less attractive from an economic, applicability, or richness of measurement point of view. As such, it opens up new possibilities for NDE in an industrial framework.

Moreover, because the noise was found not to be a limiting factor, the acquisitions may be noisier that the method would still be efficient. This implies shorter acquisition times, which can be further shortened if only a few views are considered relevant.

Studies are currently being initiated to verify the applicability of the method in production lines.

Bibliography

[1] Hugo Leclerc, Stéphane Roux, and François Hild. Projection savings in CT-based digital volume correlation. *Experimental Mechanics*, 55(1):275–287, 2015.

[2] Cédric Fragnaud, Clément Remacha, Julián Betancur, and Stéphane Roux. CAD-based X-ray CT calibration and error compensation. *Measurement Science and Technology*, 33(6):065024, 2022.

[3] Cédric Fragnaud, Clément Remacha, Julián Betancur, and Stéphane Roux. Model-based dimensional NDE from few X-ray radiographs: Application to the evaluation of wall thickness in metallic turbine blades. Submitted to *Precision Engineering*.

[4] Kévin Cosseron, David Mellé, Jean-Frédéric Diebold, François Hild, and Stéphane Roux. Optimized gauging for tire-rim loading identification. *European Journal of Mechanics-A/Solids*, 87:104192, 2021.

[5] Árpád Marinovszki, Jan De Beenhouwer, and Jan Sijbers. An efficient CAD projector for X-ray projection based 3D inspection with the ASTRA Toolbox. In *Proceedings of the 8th Conference on Industrial Computed Tomography (iCT 2018), Wels, Austria*, pages 1–6, 2018.

Appendices

Résumé étendu en français

Dans un moteur d'avion, les aubes de turbine haute pression (HP) sont exposées à la température extrême des gaz d'échappement, connue sous le nom de température d'entrée de la turbine HP, pouvant atteindre 1580°C. Elles subissent en outre de fortes contraintes mécaniques, notamment en raison de la force centrifuge résultant de leur rotation autour de l'arbre HP. Les aubes résistent à ces conditions thermiques et mécaniques intenses grâce à de multiples innovations, qui n'ont de sens que si des contrôles stricts sont effectués lors de leur production. Parmi les méthodes de Contrôles Non Destructifs (CND), la radiographie par rayons X se distingue par sa capacité à imager la structure interne (complexe) de l'aube. Une image radiographique est obtenue en exposant la pièce à inspecter à une source de rayons X. Les rayons émis par la source sont atténués à différents niveaux en fonction du trajet qu'ils suivent en traversant l'objet. Les intensités des rayons en sortie de pièce sont mesurées par un détecteur afin d'obtenir une image 2D de l'échantillon montrant sa structure interne. En vue de répondre aux impératifs de la production, le contrôle par radiographie se doit d'être rapide, ce qui se traduit en l'acquisition et l'analyse par un opérateur d'un nombre restreint d'images radiographiques de l'aube, typiquement une dizaine.

Dans ce cadre, le travail de thèse présenté dans ce manuscrit vise à développer une méthode de CND fondée sur un nombre réduit d'images radiographiques, pour l'identification et la caractérisation d'indications géométriques. De nombreux contrôles sont effectués sur les aubes de turbine. Nous nous sommes ici limités, pour des raisons pratiques, aux contrôles d'épaisseur de parois. Ce contrôle est primordial puisque les imperfections d'épaisseur de parois peuvent nuire à l'intégrité des aubes lorsqu'elles opèrent à des températures élevées, menaçant ainsi l'intégrité du moteur. Ainsi, nous proposons de développer une méthode de CND pour le contrôle d'épaisseur de parois. Le processus à développer vise à contourner les difficultés suivantes :

- *le nombre limité de vues* : cela implique l'utilisation d'une quantité réduite d'informations sur la pièce inspectée.

- *les phénomènes à l'origine de la formation des images radiographiques* : la formation des images radiographiques indique qu'une attention particulière doit être portée à l'interprétation des niveaux de gris observés. Pour chaque énergie des photons, l'atténuation est dictée par la loi de Beer-Lambert. Mais le coefficient d'absorption varie avec leur énergie. Ce phénomène est connu sous le nom de durcissement du faisceau et entraîne une relation non-linéaire entre la valeur de l'atténuation mesurée et l'épaisseur de matière traversée par le rayon. De plus, en traversant la matière, un photon peut dévier de sa trajectoire (rectiligne) initiale suite à son interaction inélastique avec les électrons. Ce phénomène, connu sous le nom de diffusion Compton, conduit à la détection d'un signal parasite qui entraîne une réduction de contraste dans les images. Ces deux phénomènes

concourent à invalider une vision purement "géométrique" de la formation des radiographies, qui prévaut le plus souvent, y compris pour la reconstruction tomographique. Ils sont souvent négligés en tomographie, voire "estompés" après reconstruction, mais ils sont critiques lorsque le contrôle est réalisé à partir d'un nombre réduit d'images, à savoir une dizaine.

- *la dépendance de l'opérateur* : ceci appelle à un processus automatisé dans lequel les données d'entrée correspondent aux images radiographiques observées (et des informations complémentaires, comme mentionné ci-dessus), et les données de sortie sont des marqueurs révélant les indications géométriques sur la pièce (identification), et des mesures dimensionnelles précises (caractérisation).

- *le biais de l'évaluation des mesures dimensionnelles 3D à partir d'images 2D* : cette problématique suggère que les mesures ne devraient pas être évaluées directement à partir des images, mais plutôt à partir d'un modèle en 3D de la pièce inspectée.

En tenant compte de ces contraintes, nous avons conçu un processus de CND consistant à créer un modèle 3D déformable de l'aube recalé à partir des images observées. Les cotes à contrôler sont mesurées sur le modèle recalé sur les projections. Ce processus repose sur la Corrélation de Volumes Numériques fondée sur les Projections (*Projection-based Digital Volume Correlation*, ou P-DVC). La P-DVC vise à minimiser une fonction de coût faisant intervenir les résidus de projection, définis comme étant les différences entre les images observées et celles simulées numériquement. À partir des images radiographiques acquises représentant la pièce inspectée et de son modèle CAO, le processus est défini par cinq étapes principales :

0. **Analyse du bruit** : une étape préliminaire de la procédure consiste à évaluer le bruit polluant une image radiographique. Elle permet d'introduire une fonction de la P-DVC optimale vis-à-vis du bruit d'acquisition, et fournit une valeur de référence (écart-type du bruit) pour l'interprétation des résidus de projection. Les propriétés du bruit affectant une image de blanc ont d'abord été déterminées (normalité, variance, corrélations spatiales), à partir desquelles celles du bruit affectant une image radiographique ont été inférées et vérifiées expérimentalement. Cette étape est détaillée au chapitre 2.

1. **Affinement de la géométrie de projection** : la simulation d'images radiographiques requiert la définition de la géométrie de projection qui englobe la géométrie du système d'acquisition (position relative de la source et du détecteur, orientation du détecteur, *etc.*). Dans ces travaux, nous proposons d'affiner la géométrie de projection par P-DVC. Cette étape est détaillée au chapitre 3.

2. **Estimation du durcissement du faisceau** : ce phénomène se traduit par une relation non-linéaire entre l'atténuation et l'épaisseur de matière traversée par le faisceau. L'estimation de cette relation permet la correction du durcissement de faisceau, qui se réduit à un réencodage non-linéaire des niveaux de gris à l'aide d'une fonction de correction (paramétrique). Dans ces travaux, nous proposons d'identifier la fonction de correction, modélisée comme une fonction linéaire par

morceaux, de manière itérative par P-DVC. Outre sa simplicité, une telle fonction a l'avantage d'être un bon interpolant de la fonction à identifier, avec la propriété que plus il y a de paramètres, meilleure est l'interpolation, sans perte de stabilité. Cette étape est détaillée au chapitre 3.

3. **Estimation de la diffusion Compton** : le phénomène de diffusion entraîne la mesure d'un signal parasite. Dans ces travaux, le signal du rayonnement diffusé est modélisé comme le résultat de la convolution entre le signal primaire et un noyau paramétrique à estimer, dont les paramètres sont identifiés itérativement par P-DVC. La contribution de la diffusion Compton suggère que le noyau est symétrique et en forme de cloche. Une superposition de fonctions gaussiennes peut être choisie pour la décrire, de sorte que le noyau est modélisé comme une somme pondérée de fonctions gaussiennes de largeurs différentes. Cette étape est décrite au chapitre 3.

4. **Déformation du modèle** : pour mesurer les écarts de forme entre pièce idéale et pièce imagée, la géométrie réelle de la pièce imagée doit être déduite des images radiographiques. Cette inférence de la forme repose sur la définition d'un modèle de déformation. Le modèle de déformation doit être suffisamment riche pour représenter la variabilité de forme attendue, tout en comportant un nombre minimal de paramètres pour assurer un meilleur conditionnement, et donc une plus faible incertitude. Dans ces travaux, un modèle de déformation parcimonieux mais représentatif est proposé. Il s'appuie sur le processus de fabrication des aubes de turbine et a été conçu en collaboration avec des experts en CND des aubes de turbine, familiers des imperfections dimensionnelles rencontrées sur les lignes de production. Il consiste en la partition de la pièce en plusieurs sous-parties : une représentant la surface externe, cinq représentant les différents éléments du noyau céramique décrivant la géométrie interne. Leur cinématique relative est donnée par un mouvement de corps-rigide, accompagné d'un facteur d'échelle pour tenir compte du retrait thermique. Cette étape est détaillée au chapitre 4.

Il convient de noter qu'à l'issue de l'étape 3, les résidus de projection obtenus en utilisant le modèle nominal de l'aube (*i.e.* son modèle CAO) contiennent les écarts géométriques entre la pièce inspectée et son modèle idéal. Ces écarts peuvent être mis en évidence en comparant les résidus à la valeur de référence définissant le niveau de bruit, introduite à l'étape 0.

La fiabilité de l'approche pour mesurer l'épaisseur de paroi d'une aube de turbine est évaluée par une étude de répétabilité. Malgré les erreurs du modèle, le modèle corrigé est comparable à la vérité terrain donnée par le tomogramme. Cette similitude de forme implique des mesures d'épaisseur de paroi similaires, qui peuvent être affinées en corrigeant les erreurs de modèle.

Des pistes de réflexion pour améliorer la précision des mesures sont envisagées, dans l'optique de trouver une alternative économiquement plus intéressante que la tomographie et plus riche et précise que les contrôles ultrasons actuellement opérés sur les aubes.

université PARIS-SACLAY

ÉCOLE DOCTORALE
Sciences mécaniques et énergétiques, matériaux et géosciences (SMEMAG)

Titre: Estimation de paramètres de forme d'un modèle 3D à partir d'images radiographiques multi-vues
Mots clés: Imagerie Rayons X, Métrologie, Contrôle Non Destructif, Modélisation 3D

Résumé: Les aubes de turbine haute pression des moteurs d'avion sont soumises à des conditions thermiques et mécaniques extrêmes. Elles y résistent grâce à de multiples innovations, qui n'ont de sens que si des contrôles stricts sont effectués lors de leur production. Parmi les méthodes de Contrôles Non Destructifs (CND), la radiographie par rayons X se distingue par sa capacité à imager la structure interne (complexe) de l'aube. En vue de répondre aux impératifs de la production, ce contrôle se doit d'être rapide, ce qui se traduit en l'acquisition et l'analyse d'un nombre restreint d'images radiographiques de l'aube, typiquement une dizaine. Dans ce cadre, le travail de thèse présenté dans ce manuscrit vise à développer une méthode de CND fondée sur un nombre réduit d'images radiographiques, pour l'identification et la caractérisation d'indications géométriques.

La démarche choisie pour répondre à cette problématique consiste à créer un modèle 3D déformable de l'aube recalé à partir des images observées en utilisant une approche *Projection-based Digital Volume Correlation* (P-DVC). Les cotes à contrôler sont mesurées sur le modèle recalé sur les projections. La P-DVC repose sur la minimisation d'une fonction de coût faisant intervenir les résidus de projection, définis comme étant les différences entre les images observées et celles simulées numériquement. Dans un premier temps, une étude sur le bruit affectant une image radiographique a été conduite. Les propriétés du bruit affectant une image de blanc ont d'abord été déterminées (normalité, variance, corrélations spatiales), à partir desquelles celles du bruit affectant une image radiographique ont été inférées et vérifiées expérimentalement. Cela permet d'obtenir une mesure de référence pour interpréter les résidus de projection (niveau de bruit), et d'introduire une fonction de coût optimale vis-à-vis du bruit d'acquisition. En outre, les phénomènes physiques intervenant lors de la formation des images radiographiques se doivent d'être identifiés et correctement étalonnés pour simuler des images radiographiques réalistes, $i.e.$ comparables à celles observées. Le durcissement du faisceau et la diffusion Compton sont les deux mécanismes physiques principaux qui entravent l'analyse quantitative des images. Des modèles paramétriques pour reproduire ces phénomènes sur les images simulées ont été proposés. Les paramètres associés sont identifiés de manière itérative par P-DVC. Les résidus de projection obtenus en utilisant le modèle nominal de l'aube ($i.e.$ son modèle CAO) sont exploités pour identifier des indications géométriques. Leur quantification s'appuie sur la déformation de ce modèle, pour ajuster le modèle recalé susmentionné. Le modèle de déformation doit être suffisamment riche pour représenter la variabilité de forme attendue, tout en comportant un nombre minimal de paramètres pour assurer un meilleur conditionnement, et donc une plus faible incertitude. Un modèle inspiré du procédé de fabrication de l'aube a été construit. Il consiste en la partition de la pièce en plusieurs sous-parties : une représentant la surface externe, cinq représentant les différents éléments du noyau céramique décrivant la géométrie interne. Leur cinématique relative est donnée par un mouvement de corps rigide, accompagné d'un facteur d'échelle pour tenir compte du retrait thermique. Les mesures d'épaisseur de paroi de l'aube calculées sur le modèle recalé sont proches de celles calculées sur un volume tomographique. Des pistes de réflexion pour améliorer la précision des mesures sont envisagées, dans l'optique de trouver une alternative économiquement plus intéressante que la tomographie et plus riche que les contrôles ultrasons actuellement opérés sur les aubes. En outre, le caractère générique de la méthode permet son application au CND d'autres pièces métalliques.

université PARIS-SACLAY

ÉCOLE DOCTORALE
Sciences mécaniques et énergétiques, matériaux et géosciences (SMEMAG)

Title: Shape parameter estimation of a 3D model from multi-view radiographic images
Keywords: X-ray imaging, Measurements, Non Destructive Evaluation, 3D modeling

Abstract: High pressure turbine blades in aircraft engines are exposed to extreme thermal and mechanical conditions. They withstand them through multiple innovations, which demand strict controls to be carried out during their production. Among the Non Destructive Evaluation (NDE) methods, X-ray radiography offers the ability to image the internal (complex) structure of the blade. To meet the production requirements, this control must be fast, which translates into the acquisition and analysis of a limited number of radiographic images of the blade, typically around ten. In this context, the thesis work aims at developing an NDE method based on a limited number of radiographic images, for the identification and characterization of geometrical indications.

The selected strategy to address this challenge consists in generating a deformable 3D model of the blade registered onto the observed images using a Projection-based Digital Volume Correlation (P-DVC) approach. The dimensions to be checked are calculated on the registered model. The P-DVC relies on the minimization of a cost function involving the projection residuals, defined as the differences between observed and numerically simulated images. First, a study of the noise present in radiographic images has been conducted. The properties of the noise polluting a flat-field image were first determined (normality, variance, spatial correlations), from which those of the noise of a radiographic image were inferred and verified experimentally. This provides a reference measurement to interpret the projection residuals (noise level), and to introduce a cost function optimal for the acquisition noise. Additionally, the physical phenomena involved in the formation of radiographic images must be identified and correctly calibrated to simulate realistic radiographic images, comparable to those observed. Beam Hardening and Compton scattering are the two main physical mechanisms that impede quantitative image analysis. Parametric models to reproduce these phenomena on simulated images have been proposed. The associated parameters are iteratively identified through P-DVC. The projection residuals obtained using the nominal model of the blade ($i.e.$ its CAD model) are processed to identify geometric indications. Their characterization is achieved through the deformation of this model, so as to generate the above-mentioned corrected model. This deformation implies the design of a deformation model, which needs to be rich enough to represent the expected shape variability while containing a reasonable ($i.e.$ small) number of parameters to ensure a good conditioning, and hence a low uncertainty. A model derived from the manufacturing process of the blade has been designed. It consists in the partition of the part into multiple subparts: one representing the external surface, five representing the different elements of the ceramic core describing the intern geometry. Their relative kinematics is given by a rigid-body motion, plus a scale factor to account for thermal shrinkage. The wall thickness measurements of the blade calculated on the registered model match well those calculated on a tomographic volume. Further reflections for improving the precision of the measurements are considered, with a view to finding an alternative economically more interesting than tomography and richer than the ultrasound controls currently carried out on the blades. Additionally, the generic nature of the method allows its application to the NDE of other metallic parts.